Pure

Bangor University

DOCTOR OF PHILOSOPHY

Intersubband optical processes in semiconductor quantum wells.

Cheung, Colleen Yue Ling

Award date:
1998

Awarding institution:
Bangor University

Link to publication

General rights
Copyright and moral rights for the publications made accessible in the public portal are retained by the authors and/or other copyright owners and it is a condition of accessing publications that users recognise and abide by the legal requirements associated with these rights.

- Users may download and print one copy of any publication from the public portal for the purpose of private study or research.
- You may not further distribute the material or use it for any profit-making activity or commercial gain
- You may freely distribute the URL identifying the publication in the public portal ?

Take down policy
If you believe that this document breaches copyright please contact us providing details, and we will remove access to the work immediately and investigate your claim.

Download date: 29. Jun. 2024

Intersubband Optical Processes in Semiconductor Quantum Wells

Colleen Yue Ling Cheung

Thesis submitted to the University of Wales

in candidature for the degree of Doctor of Philosophy

November 1998

School of Electronic Engineering and Computer Systems,
University of Wales, Bangor.

NI DDEFNYDDIO YN Y
LLYFRGELL YN UNIG

TO BE CONSULTED IN THE
LIBRARY ONLY

LLYFRGELL U.W.B LIBRARY

Synopsis

In this thesis, several aspects of the optical properties of intersubband semiconductor lasers are studied theoretically, including the waveguiding properties of quantum cascade lasers (QCLs), the anticipated modulation bandwidth, gain and threshold current of intersubband lasers, and the engineering of nonlinear susceptibilities in intersubband quantum well structures. Using two computational solvers, for the Helmholtz and Schrödinger Equations respectively, optical waveguide structures and multi quantum well (MQW) structures are designed for subsequent research. The waveguide design of a QCL reported by the Bell Labs reseachers is analysed and improved upon. A four level rate equation model was used to obtain the population inversion condition and modulation response for a triple quantum well structure (TQW) designed for intersubband lasing. An analytical expression for the modulation response is first obtained, followed by a numerical computation to verify the results. It is demonstrated that there is a unique dependence of the modulation bandwidth upon the output power of the laser, and that the maximum modulation frequency does not increase monotonically with optical output power as is the case with conventional semiconductor lasers. An expression describing the optical gain of intersubband lasers is also derived. Using this, investigations into the predicted achievable gain in mid-infrared (MIR) and near-infrared (NIR) intersubband lasers are conducted. It is found that the NIR gain is at least an order of magnitude higher than that of the MIR case. Self-consistent calculations of the optical gain are also undertaken, where the rate equations and the optical gain equations are solved alternately. An intersubband structure is designed for both triple harmonic generation (THG) and four-wave mixing (FWM). The third order nonlinear susceptibilities of these respective processes in the structure were calculated and found to be comparable to those of structures designed for just one process.

To my parents, and to Oliver.

We shall not cease from exploration.

And the end of all our exploring

Will be to arrive where we started -

And know the place for the first time.

- T. S. Elliot, *The Four Quartets.*

Acknowledgements

I would like to thank, first of all, my supervisor Prof. K. Alan Shore, who is probably one of the best supervisors anyone could hope for. I am truly indebted to him for his assistance and guidance, not to mention his books, of which I have borrowed many, and still am borrowing. I am also grateful to the rest of my supervisory committee, Dr. Paul Rees and Dr. Paul Spencer. P. Rees for his help at various times when I was stuck at some point of research or other, and for his general optimism. P. Spencer for being the most organised person I have ever known, and for letting me (sometimes) have copies of the papers I invariably mislay.

I would also like to thank Jianming, Yanhua, Siva and Iestyn for their help with the technical bits, and for letting me observe their experiments, Dr. Gareth Roberts for putting me on his server list, and Albert Rees for his cheerful presence. And Andrea, Dewi, Guy and Rob for generally being entertaining throughout those weeks when I had to stay in front of my computer and write this thesis. And finally, Oliver, and my parents for their unfailing support and belief that I would actually get to finish this!

The financial support of the School of Electronic Engineering and Computer systems, University of Wales, Bangor and the Committee of Vice Chancellors and Principals are gratefully acknowledged.

Contents

List of Figures

Chapter 1

Overview of Intersubband Lasers

1.1 Introduction

Lasers are fast becoming an integral part of our lives, so much so that it seems almost astounding that when the first laser was successfully demonstrated in 1960, it was known as a "solution looking for a problem," and that, within research circles at least, the acronym *laser* stood for "Less Application of Stimulated Expensive Research." This, of course, gives credence to the practice of funding blue-sky research, and is no doubt much cited by researchers looking for funds.

In the early 1960s, when research on He-Ne, ruby and other lasers was started, many laboratories and institutions also began research on semiconductor lasers. At that time, J. B. Gunn discovered what is now known as the "Gunn effect" in which particular solid-state devices such as gallium arsenide

and calcium sulphide were found to be capable of driving microwave oscillations. As a consequence, studies on III-V semiconductors were started [1]. At that time, it was understood that semiconductor lasers must be considered not only as simple diodes but also as optical waveguides. In 1962, along with their report of the first successful operation of semiconductor lasers, expressions and equations leading to a direct modulation limit were also discovered by Hall *et al* [1], [2].

Infrared semiconductor lasers, especially those emitting light in the near-infrared spectral region, have found numerous applications in recent years. Semiconductor lasers working in the mid- to far- infrared region, from 2 μm to 2 mm, on the other hand, are rare due to the longer wavelengths and, hence, narrower bangaps involved. Lasers generating light in this spectral region are useful for many purposes, including pollution detection, medicine and free-space communications. However, due to the lack of suitable narrow band-gap materials, a departure from the traditional semiconductor lasing concept of electron conduction-valence bands, or interband, transition is required.

1.2 Intersubband lasers

The development of advanced processes for the growth of high quality semiconductor crystals which has now progressed to the stage where it is now possible to deposit a few monolayers at a time using techniques such as metal-organic vapour phase epitaxy (MOVPE), and molecular beam epitaxy (MBE) which allows the deposition of single monolayers of atoms ($\approx$ 3 Ä) at a time, has made possible the fabrication of ultra-thin semiconductor het-

erostructures.

This ability to fabricate such complex structures has motivated an extensive study of the physics and applications of the devices. In particular, the optical properties of semiconductor coupled quantum well (QW) structures and superlattices in the infrared wavelength have gathered much interest since the first observation of the large oscillator strength of an intersubband transition within a QW by West *et al* [3].

Intersubband lasers offer opportunites for obtaining compact laser sources with emission wavelengths in nearly the whole range of the infrared range from the near- to the far-infrared (say 1.3 μm - 100 μm). These devices utilise electronic transitions in the conduction band (or valence band hole transitions) to achieve population inversion and lasing, hence the term 'unipolar'. Such lasers have attracted considerable attention following the development by Faist, Capasso *et al* of mid-infrared (MIR) quantum cascade lasers [4]. That work gave the first practical demonstration of a long-standing proposal for the utilisation of intersubband transitions to obtain lasing action in semiconductor superlattices [5]. Quite considerable progress has subsequently been made in improving the operating characteristics of those devices [6], [7], and it thus becomes relevant to assess the expectations of operating characteristics of intersubband laser devices including their anticipated gain and threshold current values.

In this thesis, an investigation of the following optical properties of in-

tersubband devices is detailed, namely the waveguiding properties of the so-called quantum cascade lasers (QCLs), the anticipated modulation bandwidth, gain and threshold current of intersubband lasers, and the engineering of nonlinear susceptibilities in intersubband quantum well structures. The above topics will be briefly introduced in the following sections and the organisation of the thesis is outlined. In the following chapters, the basic concepts relevant to the subject of interest in the chapter will be introduced first before proceeding with the description of the work and investigations.

1.3 Wave Equations for Optical Waveguides and Electron Wavefunctions

The similarities between the wave equations for optical waveguides and that of multi quantum well (MQW) structures have long been noted, and these are utilised in Chapter 2, where the computational methods for solving firstly, the Helmholtz Equation for optical fields in waveguides to find the supported modes, and secondly, the conduction-band time-independent Schrödinger Equation for the electron in MQWs to find the energy eigenstates and the corresponding wavefunctions, are discussed.

These methods are utilised to design and conduct studies of the waveguide and intersubband MQW structures which will be investigated in the rest of this thesis.

1.4 Optical Waveguiding Properties of Quantum Cascade Lasers

The predominantly TM-polarised light produced by intersubband transitions means that there is a possibility that some light might be lost via mode coupling with surface plasmons, which are modes which propagate in the interface between two media which have dielectric constants of opposite sign, e.g., a metal and a semiconductor. In Chapter 3, the waveguide design of a working QCL reported in [6] is investigated, and improvements to the structure are suggested [8].

1.5 Rate Equations and Modulation Bandwidth of Intersubband Lasers

A study of the light-current characteristics and threshold current density of a triple quantum well (TQW) intersubband structure is detailed in Chapter 4. Analytical expressions for the population inversion condition and threshold current were obtained. There, the four-level rate equations [9], [10] which were utilised in the calculations and those described in the following chapters are introduced. The electron transport through the TQW structure is also discussed. The modulation response of intersubband structures is analytically found by performing a small signal analysis on these rate equations [11], and preliminary investigations of the direct current modulation response are conducted.

The two TQW structures designed for mid-infrared (MIR) and near-infrared (NIR) lasing are presented in Chapter 5. The requirements considered in the design are prescribed [12]. Studies of the anticipated modulation bandwidth of these structures are performed using a numerical computational method based on the dynamics of the rate equations [13].

1.6 Intersubband Optical Gain

In Chapter 6, the fundamental theory necessary to provide an adequate description of optical gain in intersubband devices is examined, and the expression for intersubband optical gain is derived [14]. The expression is found to be almost similar to that reported in [15]. The lineshape function utilised in that work is also incorporated into the optical gain expression presented here.

Using the expression for gain as well as the four-level rate equations, in Chapter 7 a self-consistent study of the intersubband optical gain is addressed [16].

1.7 Intersubband Nonlinearities

The development of the laser also heralded the birth of the field of nonlinear optics - a field previously limited to studies of the behaviour ordinary light beams under the effect of strong externally applied magnetic and electric fields. The intense and focused light produced by lasers possess electric and magnetic fields that were so strong that the characteristics of the medium in which it is travelling were affected. This may be put under the general

category of extrinsic nonlinearity. The complementary category of intrinsic nonlinearity involves phenomena such as second and third harmonic generation, and sum and difference frequency generation, which in general can be described as the conversion of input light of a certain frequency to output light of a different frequency via interactions with polarisable material.

One of the properties of intersubband structures is that their energy levels can be tailored by suitable design of the wells and barriers using the appropriate semiconductor alloys. In Chapter 8, a MQW structure with energy levels appropriate for both triple harmonic generation and four wave mixing, with large third order susceptibilities is designed and investigated [17].

References

[1] K. Iga, *Fundamentals of Laser Optics*, Chapter 5, Plenum Press, New York, 1994.

[2] R. N. Hall, G. H. Fenner, J. D. Kingsley, T. J. Soltys, and R. D. Carlson, *Phys. Rev. Lett.* 9, p.366, 1962.

[3] L. C. West and S. J. Eglash, "First observation of an extremely large-dipole infrared transition within the conduction band of a GaAs quantum well," *Appl. Phys. Lett.* 46, pp. 1156-1158, 1985.

[4] J. Faist, F. Capasso, D. L. Sivco, C. Sirtori, A. L. Hutchinson and A. Y. Cho, "Quantum cascade laser," *Science*, 264, pp. 553-556, 1994.

[5] R. F. Kazarinov and R. A. Suris, "Possibility of the amplification of electromagnetic waves in a semiconductor with a superlattice," *Sov. Phys. Semiconductor*, 5, pp. 797-800, 1971.

[6] J. Faist, F. Capasso, D. L. Sivco, C. Sirtori, A. L. Hutchinson and A. Y. Cho, "Continuous wave operation of a vertical transition quantum cascade laser above T = 80K," *Appl. Phys. Lett.*, 67, pp. 3057-3059, 1995.

[7] C. Sirtori, J. Faist, F. Capasso, S. L. Sivco, A. L. Hutchinson and A. Y. Cho, "Mid-infrared (8.5 μm) semiconductor lasers operating at room temperature," *IEEE Photonics Technol. Lett.*, 9, pp. 294-296, 1997.

[8] P. S. Spencer, C. Y. L. Cheung and K. A. Shore, "Sensitivity analysis of the optical-waveguide properties of quantum cascade lasers," *IEE Proc.-Optoelectron.* 144, pp. 323-326, 1997.

[9] W. M. Yee, K. A. Shore and E. Schöll, "Carrier transport and intersubband population inversion in coupled quantum wells," *Appl. Phys. Lett.*, **63**, pp. 1089-1091, 1993.

[10] W. M. Yee and K. A. Shore, "Threshold current density calculations for far-infrared semiconductor lasers," *Semicond. Sci. Technol.*, **9**, pp. 1190-1197, 1994.

[11] C. Y. L. Cheung, P. S. Spencer and K. A. Shore, "Modulation bandwidth optimisation for unipolar intersubband semiconductor lasers," *IEE Proc. Optoelectron.* **144**, pp. 44-47, 1997.

[12] C. Y. L. Cheung and K. A. Shore, "Anti-crossing and coupling effects in the design of intersubband semiconductor lasers," submitted for publication.

[13] C. Y. L. Cheung and K. A. Shore, "Self-consistent analysis of the dc modulation response of unipolar semiconductor lasers ," *J. Mod. Optics* **45**, pp. 1219-1229, 1998.

[14] C. Y. L. Cheung, P. Rees and K. A. Shore, "Gain calculations for unipolar semiconductor lasers," submitted for publication.

[15] V. B. Gorfinkel, S. Luryi and B. Gelmont, "Theory of gain spectra for quantum cascade lasers and temperature dependence of their characteristics at low and moderate carrier concentrations," *IEEE J. Quant. Electon.* **32**, pp. 1995-2003, 1996.

[16] C. Y. L. Cheung, P. Rees and K. A. Shore, "Self-consistent optical gain and threshold current calculations for 1.55μm intersubband semiconductor lasers, submitted for publication.

[17] C. Y. L. Cheung, K. A. Shore and P. Rees, Manuscript in preparation.

Chapter 2

Wave Equations for Optical Waveguides and Electron Wavefunctions

2.1 Introduction

The growing sophistication of semiconductor growth processes means that there is now scope for fabricating increasingly complex multilayer optoelectronic structures. In turn, this leads to a need for more accurate and flexible calculation techniques in order to optimize the performance of the desired devices. The Helmholtz Equation for optical fields will be used to find the waveguide modes in order to optimise laser design. The Schrödinger Equation will be applied to calculate the energy levels and envelope wavefunction, and the corresponding lifetimes of any metastable states, which are needed to find the matrix elements for intersubband transitions, as well as design

the quantum well (QW) structures for intersubband lasing. In this chapter, the application of the Argument Principle Method (APM) to the extraction of the solutions to, firstly, the Helmholtz Equation for the optical fields of a multilayer waveguide [1], and secondly, the time-independent Schrödinger Equation of a multi-quantum well (MQW) structure [2] is discussed. Similarities will be noted between the forms of the two equations.

2.1.1 The TE and TM Polarisations in a Waveguide

In general, the modes supported in a waveguide can be categorised into two types. These are (i) the transverse electric (TE) modes, so called because the electric field (E_y) is restricted to the transverse plane, i.e. normal to the plane of propagation; and (ii) the transverse magnetic (TM) modes, because in this case, the magnetic (H_y) field is restricted to the transverse plane.

Here, E_y and H_y are the y components of the electric and magnetic fields respectively, where the electric field is defined as $\mathcal{E} = (E_x, E_y, E_z)$, and the magnetic field is defined as $\mathcal{H} = (H_x, H_y, H_z)$. TE modes involve the field components E_y, H_x and H_z, while TM modes involve the field components H_y, E_x and E_z.

2.1.2 The Electron Wavefunction in a QW

The electron wavefunction ϕ describes the state of the electron. A rigorous calculation of it may be performed by solving the Schrödinger Wave equation with the appropriate crystal potential. However, since such an exact calculation tends to be complicated and difficult to work with, approximations

PAGE/PAGES EXCLUDED UNDER INSTRUCTION FROM UNIVERSITY

(2.8), and can be written as

$$\begin{aligned} E_{yi}(x) &= A_i \exp[-j\tilde{\kappa}_i d_i + B_i \exp[+j\tilde{\kappa}_i d_i] \\ \omega\mu_0 H_{zi}(x) &= A_i\tilde{\kappa}_i \exp[-j\tilde{\kappa}_i d_i + B_i\tilde{\kappa}_i \exp[+j\tilde{\kappa}_i d_i] \end{aligned} \tag{2.7}$$

where d_i defines the thickness of the ith layer, as shown in Figure 2.4.

Using the solutions of the above equations, the tangential fields at the bottom of the ith layer ($x = x_i$) can be expressed as a function of the fields within that layer as

$$\begin{aligned} \begin{bmatrix} E_{yi}(x_i) \\ \omega\mu_0 H_{zi}(x_i) \end{bmatrix} &= \begin{bmatrix} \cos[\tilde{\kappa}_i d_i] & \frac{j}{\tilde{\kappa}_i}\sin[\tilde{\kappa}_i d_i] \\ j\tilde{\kappa}_i \sin[\tilde{\kappa}_i d_i] & \cos[\tilde{\kappa}_i d_i] \end{bmatrix} \begin{bmatrix} E_{yi}(x_i) \\ \omega\mu_0 H_{zi}(x_i) \end{bmatrix} \\ &= \mathcal{M}_i \begin{bmatrix} E_{yi}(x_i) \\ \omega\mu_0 H_{zi}(x_i) \end{bmatrix} \end{aligned} \tag{2.8}$$

where $\mathcal{M}_i$ is the transfer matrix for the ith layer, with thickness d_i.

Hence, due to the continuity of the tangential fields at any layer interface in the multilayer waveguide structure, the fields tangential to the boundaries at the top of the substrate layer E_{yS}, H_{zS}, and at the bottom of the cladding layer E_{yC}, H_{zC}, are related via the matrix product

$$\begin{aligned} \begin{bmatrix} E_{yC}(x_C) \\ \omega\mu_0 H_{zC}(x_C) \end{bmatrix} &= \mathcal{M}_1\mathcal{M}_2\mathcal{M}_3\cdots\mathcal{M}_r \begin{bmatrix} E_{yS}(x_S) \\ \omega\mu_0 H_{zS}(x_S) \end{bmatrix} \\ &= \begin{bmatrix} m_{11} & m_{12} \\ m_{21} & m_{22} \end{bmatrix} \begin{bmatrix} E_{yS}(x_S) \\ \omega\mu_0 H_{zS}(x_S) \end{bmatrix} \end{aligned} \tag{2.9}$$

In general, the tangential fields at the boundaries can be written as

$$\begin{aligned} E_{yC}(x) &= B_C \exp[\dot{-}\tilde{\gamma}_C(x - x_{r+1})] \text{ for } x > x_{r+1} \\ \omega\mu_0 H_{zC}(x) &= -j\tilde{\gamma}_C B_C \exp[-\tilde{\gamma}_C(x - x_{r+1})] \text{ for } x > x_{r+1} \\ E_{yS}(x) &= A_S \exp(\tilde{\gamma}_S x) \text{ for } x < 0 \\ \omega\mu_0 H_{zS}(x) &= j\tilde{\gamma}_S A_S \exp(\tilde{\gamma}_S x) \text{ for } x < 0 \end{aligned} \tag{2.10}$$

where $\tilde{\gamma}_S = \pm\sqrt{\tilde{\gamma}_2 - k_0^2\tilde{n}_S^2}$, and $\tilde{\gamma}_C = \pm\sqrt{\tilde{\gamma}_2 - k_0^2\tilde{n}_C^2}$, where $\tilde{n}_S$, $\tilde{n}_C$ are the substrate and cover complex refractive indices respectively. Equations (2.9) and (2.10) yield the dispersion equation

$$\mathcal{F}(\tilde{\gamma}) = j(\tilde{\gamma}_S m_{11} + \tilde{\gamma}_C m_{22}) - m_{21} + \tilde{\gamma}_S\tilde{\gamma}_C m_{12} = 0 \tag{2.11}$$

which has as solutions the complex propagation constants $\tilde{\gamma}$.

The same procedure is followed for the TM case, with the resulting layer transfer matrices $\mathcal{M}_i$ having the same form, but with $\tilde{\kappa}_i$ replaced by $-\tilde{\kappa}_i/\tilde{n}_i^2$ in the coefficients of the sine terms, and in Equation (2.13) $\tilde{\gamma}_S$ and $\tilde{\gamma}_C$ must be replaced by $-\tilde{\gamma}_S/\tilde{n}_S^2$ and $-\tilde{\gamma}_C/\tilde{n}_C^2$ respectively.

In general, the square roots signs of $\tilde{\gamma}_S$ and $\tilde{\gamma}_C$ can be positive or negative. However, at the waveguide boundaries it is important to select the sign appropriately to correspond to whether the fields are increasing or decaying. So for bound states the solutions are chosen such that $\mathcal{R}e[\tilde{\gamma}_S] > 0$, and $\mathcal{R}e[\tilde{\gamma}_C] > 0$.

For forward leaky waves which leak energy into the substrate, $k_0 n_C < \beta < k_0 n_S$, the tranverse propagation constant in the substrate is $\tilde{\gamma}_S =$

$\pm\sqrt{\tilde{\gamma}^2 - k_0\tilde{n}_S^2} = \gamma_S' + j\gamma_S''$ and the sign selection must be such that $\gamma_S' < 0$ and $\gamma_S'' > 0$. There is no reason to modify $\tilde{\gamma}_C$ since $\mathcal{R}e[\tilde{\gamma}_C]$ must be positive.

For the case of forward propagating waves leaking energy into the cladding, exactly the same conditions hold, but with sign inversion, since $x > 0$ and with subscript change from S to C since $k_0 n_S < \beta < k_0 n_C$.

For backward propagating leaky waves with $\beta < 0$, the method is the same as for the forward leaky waves, with the only difference is that the region to be searched must be in the negative β range. Hence, by imposing the correct sign on the γ_S'', γ_C'' numbers, the desired leaky waves can be selected. The full description of all possible leaky waves that can be supported by a multilayer waveguide structure and their $\tilde{\gamma}_S$, $\tilde{\gamma}_C$, $\tilde{\gamma}$ conditions can be found in [10].

2.3 The Schrödinger Wave Equation

The Schrödinger equation can be used to obtain the energy levels and wavefunction in a MQW heterostructure. Obtaining solutions to the Schrödinger Equation will enable the extraction of the eigen-energy values of an unbiased/biased quantum heterostructure. The envelope wavefunction for conduction electrons in a single band, $\Psi(r,t)$, is described by the effective-mass Schrödinger equation [2], [3]

$$\frac{-\hbar^2}{2m^*(r)}\nabla^2\Psi(r,t) + V(r)\Psi(r,t) = i\hbar\frac{\partial}{\partial t}\Psi(r,t) = E\Psi(r,t) \qquad (2.12)$$

where r is the space position vector, $V(r)$ is the potential energy at r, $m^*(r)$ is the spatially varying electron mass, $(-\hbar/2m^*(r))\nabla^2$ is the kinetic energy

operator ($= p^2/2m^*(r)$), and E is the eigen-energy of the system. The state function can be expressed as the product of space-dependent and time-dependent factors, $\Psi(r,t) = \psi(r)w(t)$, where the time-dependent part

$$w(t) = e^{-j(E/\hbar)t} \tag{2.13}$$

The time-independent part of the Schrödinger equation, which contains the spatial-varying envelope wavefunction, $\psi(r)$, is

$$\frac{-\hbar^2}{2m^*(r)}\nabla^2\psi(r) + V(r)\psi(r) = E\psi(r) \tag{2.14}$$

The general solution for a uniform potential can be written as the sum of two counterpropagating plane waves,

$$\psi(r) = Ae^{j\tilde{\kappa}z} + Be^{-j\tilde{\kappa}z} \tag{2.15}$$

where the relation

$$\tilde{\kappa}^2 = \frac{2m^*}{\hbar^2}(E - V) \tag{2.16}$$

is found from Equation (2.14).

2.3.1 Similiarities between QW Heterostructures and Multilayer Optical Waveguides

There is no difference in the form of the time-independent Schrödinger's equation

$$-\frac{\hbar^2}{2m}\nabla^2\psi(r) + [V(r) - E]\psi(r) = 0 \tag{2.17}$$

and the form of the wave equation for the transverse electric (TE) field

$$\nabla^2\mathcal{E}(r) + [k_0^2 n^2(r) - \beta]\mathcal{E}(r) = 0 \tag{2.18}$$

Therefore the solutions for the two equations will be similiar if the boundary conditions are analogous; the boundary conditions are analogous for the TE modes which are polarised in the y-direction, but a little different for the TM modes which are polarised in the x-direction [3].

2.3.2 Energy States

The energy eigenstates, E, of a MQW structure can be of several types. These are illustrated in Figure 2.5, and are described [2], in analogy with the waveguide modes, as follows: (i) **Bound states**, in which the electrons are bounded within semi-infinitely thick left and right barriers; (ii) **Type 1 quasibound states**, in which the electrons have classically free propagation in the left and right boundary regions (these states are also referred to as *virtual* or *extended* states); (iii) **Type 2 quasibound states**, in which the electrons have classically free propagation in the right boundary region, and bounded propagation in the left boundary region; and finally (iv) For completeness it is noted that **Type 3 quasibound states**, in which the electrons have classically free propagation in the left boundary region and bounded propagation in the right boundary region, but this will not be relevant for this work as it is assumed here that an applied bias will tilt the MQW structure from left to right, as in Figure 2.5.

For quasibound energy levels, the solution of the envelope wavefunction has boundary conditions that require an electron wavefunction to leak out, and hence, using the complex energy method (CEM) [5], [6], [7], the energy

PAGE/PAGES EXCLUDED UNDER INSTRUCTION FROM UNIVERSITY

eigen-values become complex having the form $\tilde{E} = E_r + jE_i$, where $E_i \geq 0$, with the lifetime of the energy level, τ, being related to the imaginary part of the energy eigen-values as $\tau = \hbar/2E_i$ [2].

All the allowed heterostructure eigenstates can be classified according to their eigen-energy real part, $\mathcal{R}e[\tilde{E}] = E_r$, with respect to the the heterostructure barrier levels V_0 and V_{N+1}. If, as in Figures 2.5 and 2.6, $V_0 + V_{bias} > V_{N+1}$, then for (i) bound states $E_r \leq V_{N+1}$, as in regime (a) of Figure 2.6; (ii) for type 2 quasibound states $V_{N+1} \leq E_r \leq V_0 + V_{bias}$, as in regime (b); and (iii) for the type 1 quasibound states $V_0 + V_{bias} \leq E_r$, as in regime (c). The bound states are confined within the heterostructure region, the type 2 quasibound states leak out from the lowest potential energy heterostructure boundary, V_{N+1}, while the type 1 quasibound states leak out from both boundaries. The imaginary part of the eigen-energy, $\mathcal{I}m[\tilde{E}] = E_i$, is nonzero only for the case of quasibound states, i.e. for states that can leak out of the well, and it is zero for bound states.

2.3.3 Transfer Matrix Formulation

Figure 2.5 shows an arbitrary potential energy profile $V(z)$ under a bias, V_{bias}, where $V(z)$ is segmented into $i = 1, \cdots, N$ layers with piecewise constant potential energy V_i. The discretised time-independent conduction-band effective-mass Schrödinger equation for the ith region with uniform potential energy V_i, and constant effective mass m_i^*, is derived in Appendix C, and is

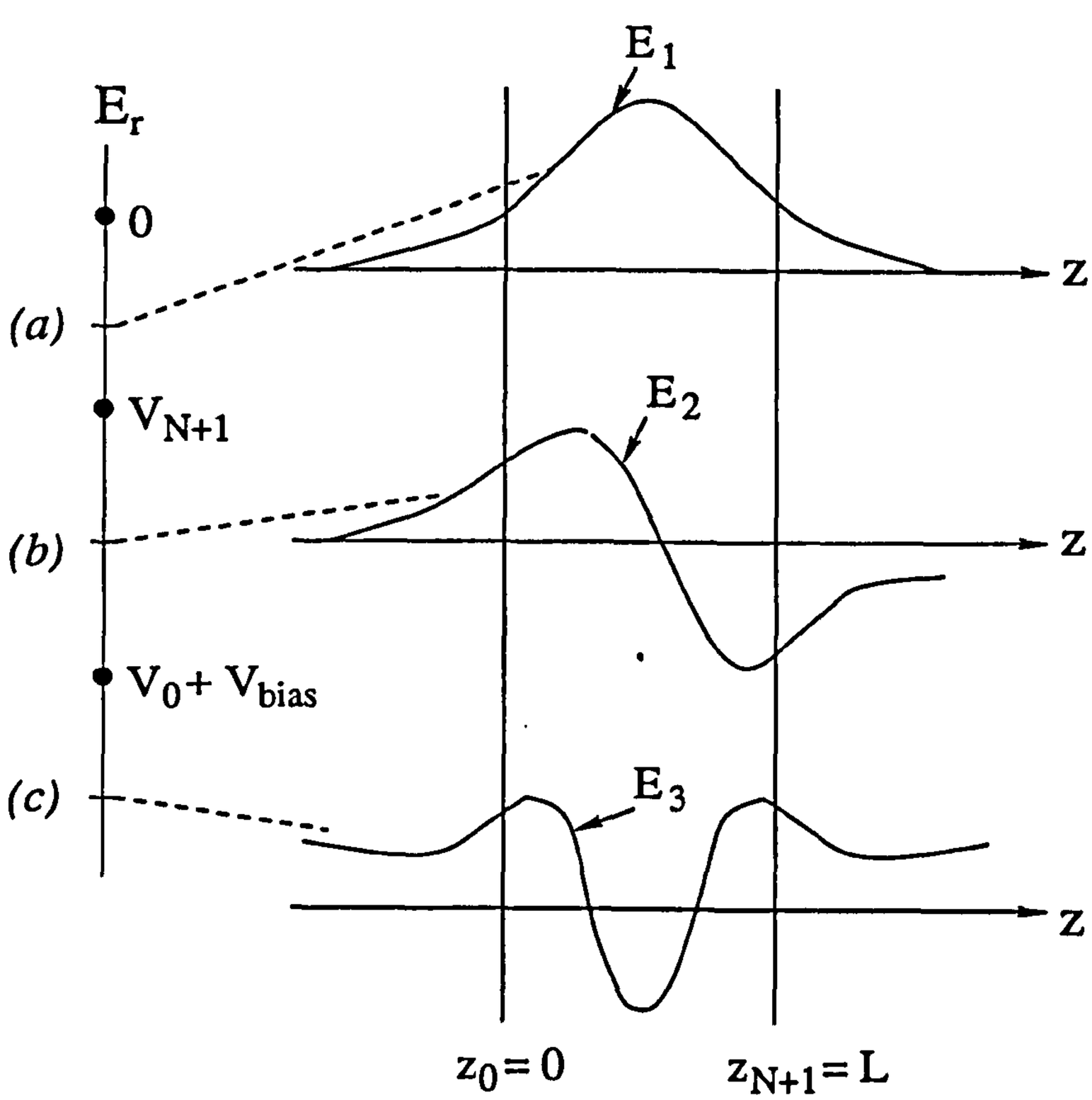

Figure 2.6: The envelope wavefunctions according to the different values of the real part of the energy eigen states, E_r.

given by [2]

$$\frac{d^2}{dz^2}\psi_i(z) + \tilde{\kappa}_i^2\psi_i(z) = 0 \qquad \text{for } z_{i-1} \leq z \leq z_i \tag{2.19}$$

where

$$\tilde{\kappa}_i = \pm\sqrt{\frac{2m_i^*}{\hbar^2}(\tilde{E} - V_i)} \tag{2.20}$$

where $\psi_i(z)$ denotes the envelope wavefunction in the ith layer, and $\tilde{\kappa}_i$ defines the complex wavevector in the same layer along the z-direction.

The boundary conditions for $\psi(z)$ at the interfaces between layers $i-1$ and i where $i = 1, 2 \cdots N+1$, are written as [8]

$$\begin{aligned} \psi_{i-1}(z_{i-1}) &= \psi_i(z_{i-1}) \\ \frac{1}{m_{i-1}^*}\frac{d}{dz}\psi_{i-1}(z_{i-1}) &= \frac{1}{m_i^*}\frac{d}{dz}\psi_i(z_{i-1}) \end{aligned} \tag{2.21}$$

due to the classical equation of particle current continuity. It was shown by Bastard [9] that for a QW, the particle current is only conserved if the factor $1/m^*$ is included in Equation (2.21). As was further pointed out in the same paper, the boundary condition in Equation (2.21) is the only one which ensures stationary eigenstates even is there is a jump in the effective mass at the boundaries. The total wavefunction for the system ψ is then given by summing the wavefunctions ψ_i in all the individual layers together.

Rewriting Equation (2.17) into the discretised form, we have

$$\begin{aligned} \psi_i(z) &= A_i e^{j\tilde{\kappa}_i(z-z_{i-1})} + B_i e^{j\tilde{\kappa}_i(z-z_{i-1})} \\ &\qquad \text{for } z_{i-1} \leq z \leq z_i \end{aligned} \tag{2.22}$$

Using Equations (2.21) and (2.22) for the ith layer with thickness d_i, the envelope wavefunction and its derivative scaled by the effective mass m_i^* at the ith layer boundaries z_{i-1} and z_i can be written as

$$\begin{bmatrix} \psi_i(z_{i-1}) \\ \frac{1}{m_i^*}\frac{d}{dz}\psi_i(z_{i-1}) \end{bmatrix} = \begin{bmatrix} \cos(\tilde{\kappa}_i d_i) & -\frac{m_i^*}{\tilde{\kappa}_i}\sin(\tilde{\kappa}_i d_i) \\ \frac{\tilde{\kappa}_i}{m_i^*}\sin(\tilde{\kappa}_i d_i) & \cos(\tilde{\kappa}_i d_i) \end{bmatrix} \cdot \begin{bmatrix} \psi_i(z_i) \\ \frac{1}{m_i^*}\frac{d}{dz}\psi_i(z_i) \end{bmatrix}$$
$$= \mathcal{M}_i \begin{bmatrix} \psi_i(z_i) \\ \frac{1}{m_i^*}\frac{d}{dz}\psi_i(z_i) \end{bmatrix} \tag{2.23}$$

Combining Equations (2.21) and (2.23), the wavefunction and its derivative scaled by the effective mass at the left ($i = 0$) and the right ($i = N+1$) heterostructure boundaries can be related as

$$\begin{bmatrix} \psi_0(z_0) \\ \frac{1}{m_0^*}\frac{d}{dz}\psi_i(z_0) \end{bmatrix} = \mathcal{M}_1\mathcal{M}_2\mathcal{M}_3\cdots\mathcal{M}_N \begin{bmatrix} \psi_{N+1}(z_{N+1}) \\ \frac{1}{m_{N+1}^*}\frac{d}{dz}\psi_{N+1}(z_{N+1}) \end{bmatrix}$$
$$= \begin{bmatrix} m_{11} & m_{12} \\ m_{21} & m_{22} \end{bmatrix} \begin{bmatrix} \psi_{N+1}(z_{N+1}) \\ \frac{1}{m_{N+1}^*}\frac{d}{dz}\psi_{N+1}(z_{N+1}) \end{bmatrix} \tag{2.24}$$

The travelling waves outside the heterostructure boundary regions can be written as

$$\begin{aligned} \psi_0(z) &= A_0 \exp[\tilde{\gamma}_0 z] \text{ for } z < 0 \\ \psi_{N+1}(z) &= B_{N+1} \exp[-\tilde{\gamma}_{N+1}(z - z_{N+1}) \text{ for } z > z_{N+1} \end{aligned} \tag{2.25}$$

where $\tilde{\gamma}_0 = j\tilde{\kappa}_0$, $\tilde{\gamma}_{N+1} = j\tilde{\kappa}_{N+1}$. The condition that $\psi(z)$ must be bounded, i.e. zero at $z = \pm\infty$, leads to

$$\begin{bmatrix} 1 & -m_{11} + m_{12}\frac{\tilde{\gamma}_{N+1}}{m_{N+1}^*} \\ \frac{\tilde{\gamma}_0}{m_0^*} & -m_{21} + m_{22}\frac{\tilde{\gamma}_{N+1}}{m_{N+1}^*} \end{bmatrix} \begin{bmatrix} A_0 \\ B_{N+1} \end{bmatrix} = 0 \tag{2.26}$$

For nontrivial solutions the determinant of Equation (2.26) must be zero, and so the dispersion equation is obtained:

$$\mathcal{F}(\tilde{E}) = m_{11}\frac{\tilde{\gamma}_0}{m_0^*} + m_{22}\frac{\tilde{\gamma}_{N+1}}{m_{N+1}^*} - m_{21} - m_{12}\frac{\tilde{\gamma}_0}{m_0^*}\frac{\tilde{\gamma}_{N+1}}{m_{N+1}^*} = 0 \qquad (2.27)$$

the zeroes of which define the heterostructure energy eigenstates. In general, the square root signs of $\mathcal{R}e[\tilde{\kappa}_i]$ from Equation (2.20) can be positive or negative. At the heterostructure boundaries, however, it is important to select the sign appropriately to correspond to whether the wavefunction is decaying or increasing. So for (i) bound states $\mathcal{R}e[\tilde{\kappa}_0] > 0$ and $\mathcal{R}e[\tilde{\kappa}_{N+1}] > 0$, (ii) type 1 quasibound states $\mathcal{R}e[\tilde{\kappa}_0] < 0$ and $\mathcal{R}e[\tilde{\kappa}_{N+1}] < 0$, and (iii) type 2 quasibound states $\mathcal{R}e[\tilde{\kappa}_0] > 0$ and $\mathcal{R}e[\tilde{\kappa}_{N+1}] < 0$.

2.4 The Argument Principle Method

The argument principle method (APM) is based on the generalised argument principle theorem which has the form [11]

$$\frac{1}{j2\pi}\oint_C \frac{f'(z)}{f(z)}dz = N - Q \qquad (2.28)$$

where f is a function which is analytic within and on C and has no zeros on C; the contour C does not pass through the origin, N and Q are the number of zeros and the number of poles of f respectively, and $f'(z)$ denotes the derivative of f with respect to z.

For the case that the function f has no poles, i.e. $Q = 0$, the equation below maybe realised [2], [11]

$$\sigma + P = \frac{1}{j2\pi}\oint_C z^P \frac{f'(z)}{f(z)}dz = \sum_{i=1}^{n} \zeta_i^P \qquad (2.29)$$

where ζ_i^P are the $i = 1, 2, \cdots, n$ zeros of f which lies in C raised to the Pth power, and σ_P is the summation of these zeros for the Pth power.

The derivative $f'(z)$ may be found using the Cauchy integral formula $f(z) = \frac{1}{j2\pi} \oint_C \frac{f(s)}{s-z} ds$ (see Appendix A), where z is any point within C and s is any point on C. If a function is analytic at a point, its derivatives of all orders exist at that point and are also analytic there [11]. It can be shown (see Appendix A) that the derivative of f at the point$z = z_0$ has the integral representation [2] [11]

$$f'(z_0) = \frac{1}{j2\pi} \oint_D \frac{f(z)}{(z - z_0)^2} dz \tag{2.30}$$

So consider a region C, and carry out the contour integral numerically for several values of P, approximations to $\sigma_0, \sigma_1, \sigma_2, \cdots$ maybe determined. When $P = 0$, Equation (2.30) takes the form of Equation (2.28). In this instance, σ_0 is an integer and gives the number of zeros of f within C. Using these approximations, a polynomial $S(z)$ of degree σ_0 may be found, the zeros of which coincide with the zeros of f in C. It has been found, however, that using Muller's Method [14], the zeros of the original function f are converged to very rapidly, so that the formation of the approximation polynomial is not necessary. Hence the program runs more efficiently when it is removed, and many of the complications related to the implementation of the routine for the approximation polynomial are not incurred. For example, in practice, the zeros of the approximation polynomial do not coincide with the zeros of the initial function $f(z)$, and further refinements usually need to be done.

2.4.1 Numerical Implementation of APM

The application of APM to the dispersion equations of Equation (2.12) and Equation (2.27), i.e. with $f(z) = \mathcal{F}(\tilde{E})$ and $f(z) = \mathcal{F}(\tilde{\gamma})$, is relatively straightforward. First, the singularity points need to be identified, after which the area between the singularities is enclosed by rectangular contours. These contours do not enclose any of the singularities. The vertical contour segments can approach the singularities arbitrarily close, while the horizontal segments should be located at a value of an order of magnitude larger than the real value range, on the imaginary axis [1],[2]. The path integral of Equation (2.29) evaluated for $P = 0$ gives the number of zeros of $f(z)$ enclosed by the contour C, i.e. the number of modes supported by the waveguide in the case of $f(z) = \mathcal{F}(\tilde{E})$, and the number of energy levels in the MQW structure if $f(z) = \mathcal{F}(\tilde{\gamma})$. The values of the propagation constants or energy levels may then be solved for.

The optical waveguide dispersion equation:

A typical multilayer-waveguide refractive index distribution in the complex plane is shown in Figure 2.7. The X's in Figure 2.7 correspond to the singularities $k_0\tilde{n}_C$ and $k_0\tilde{n}_S$. According to the previously mentioned segmentation strategy, the region of interest in the complex plane muct be enclosed by two contours C_1 and C_2, since the singular points must be excluded from any path. The contour C_2 encloses the refractive index with the maximum real part $k_0 n_{max}$.

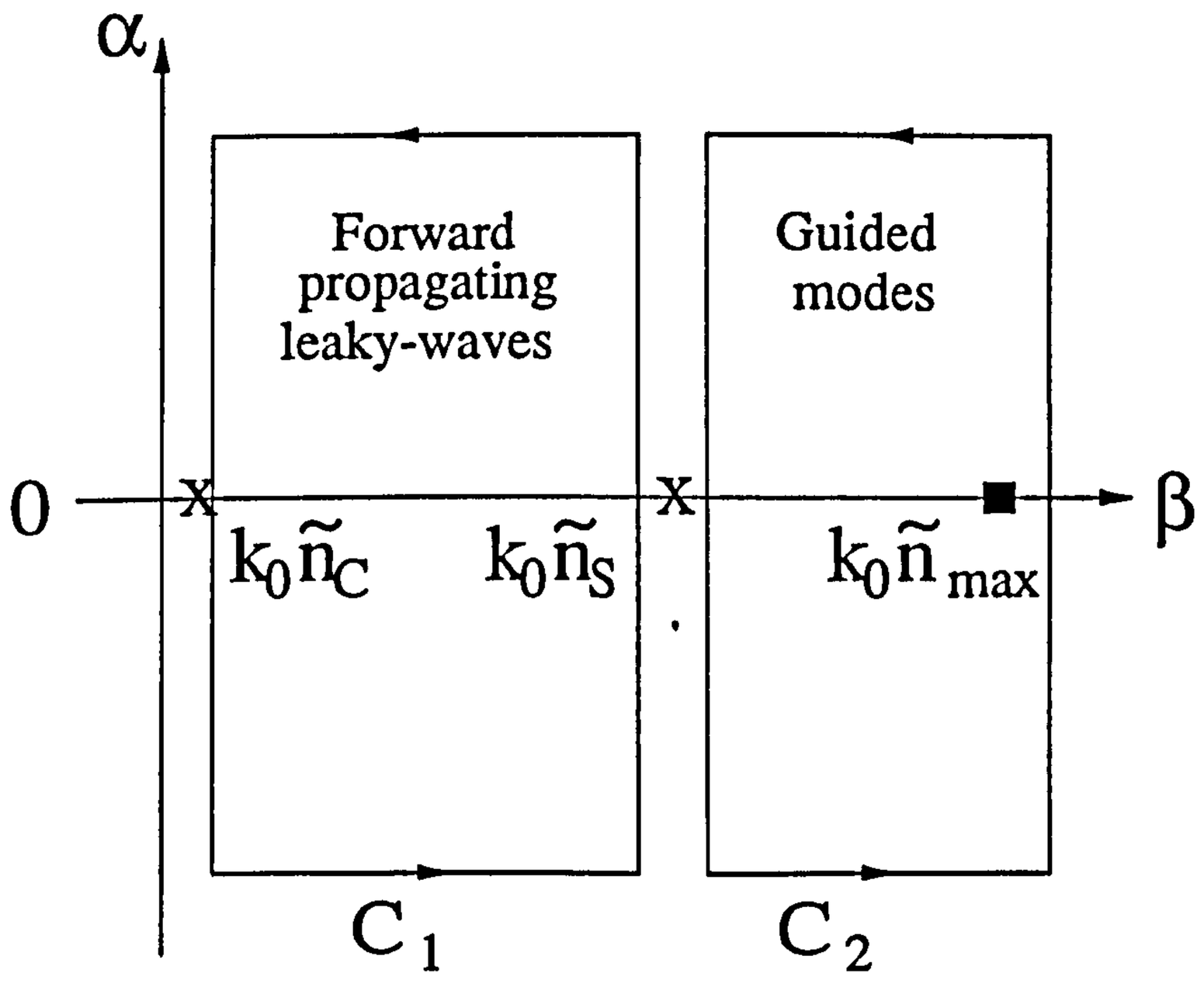

Figure 2.7: Complex plane representation of APM operation on the dispersion equation for a multilayer waveguide. $k_0\tilde{n}_{max}$ is the complex refractive index with the maximum real part and is enclosed by contour C_2.

The Schrödinger dispersion equation:

The two singularities which are marked by X's in Figure 2.8, are the two potential energy levels V_0+V_{bias} and V_{N+1}, which correspond to the heterostructure boundary regions. The energy range for which the heterostructure energy levels are of interest, is enclosed in rectangular contours which exclude the two singularities. C_1, C_2 and C_3 are the integration contours which enclose regions to be searched for complex energy eigenvalues in bound, type 2 quasibound, and type 1 quasibound respectively.

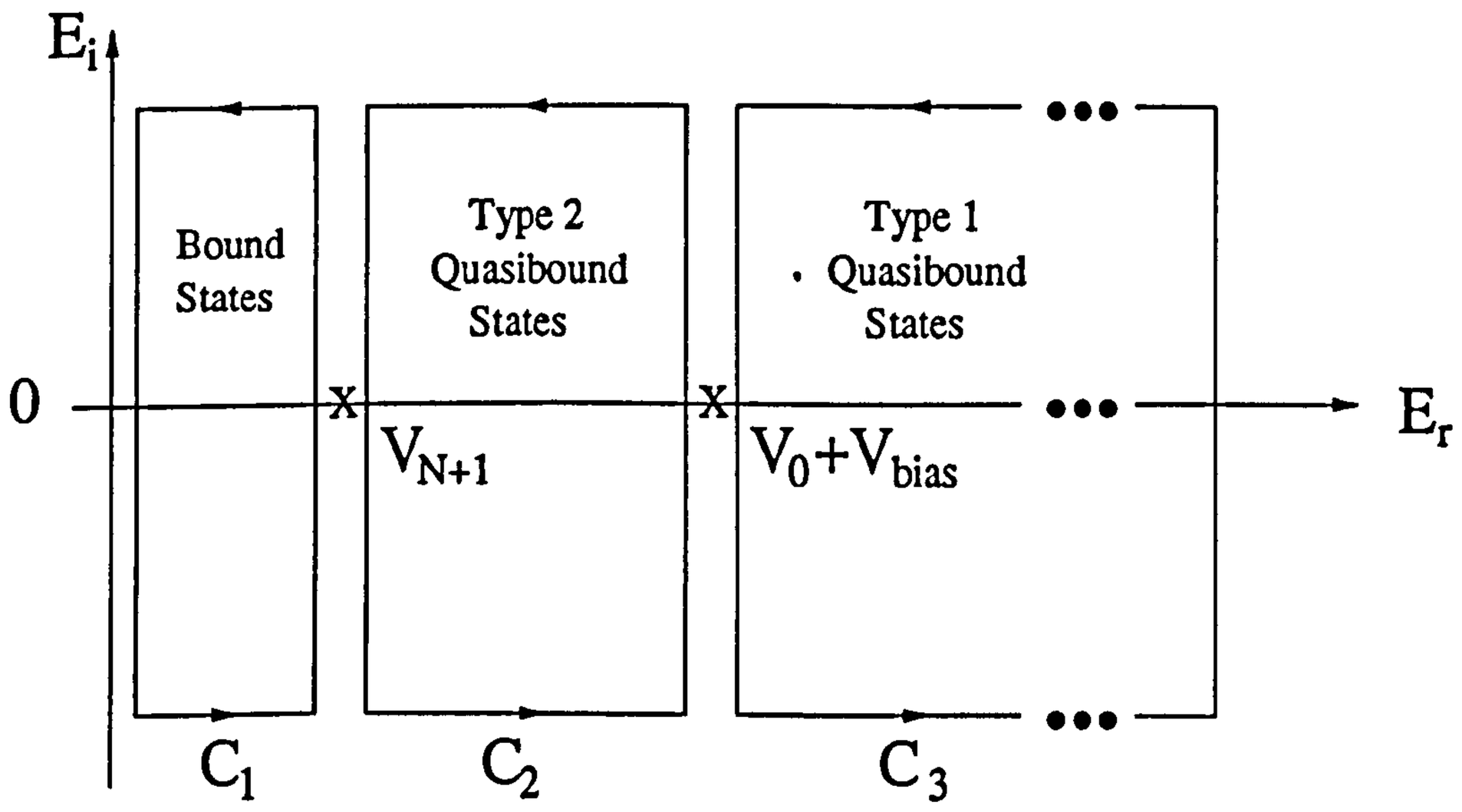

Figure 2.8: Complex plane representation of APM operation on the dispersion equation for a MQW structure.

2.5 Conclusion

In conclusion, the wave equations for both the optical fields in waveguides, and electron wavefunctions in QW heterostructures have been discussed. The transfer matrix formulations for both were presented and a single method, the APM, used for solving both analogous equations.

References

[1] E. Anemogiannis and E. N. Glytis, "Multilayer Waveguides: Efficient Numerical Analysis of General Structures," *J. Lightwave Technol.* **10**, pp. 1344-1351, 1992.

[2] E. Anemogiannis, E. N. Glytis and T. K. Gaylord, "Bound and Quasi-bound State Calculations for Biased/Unbiased Semiconductor Quantum Heterostructures," *IEEE J. Quant. Electron.* **29**, pp. 2731-2740, 1993.

[3] L. A. Coldren and S. W. Corzine, *Diode Lasers and Photonic Integrated Circuits*, Chapter 4 and Appendix 1, John Wiley & Sons, New York, 1995.

[4] P.Yeh and A. Yariv, *Optical Waves in Crystals*, Chapter 11, John Wiley & Sons, New York, 1984.

[5] L. D. Landau and E. M. Lifshitz, *Quantum Mechanics: Non-Relativistic Theory*, p. 555, Pergamon, New York, 1977.

[6] T. B. Bahder, C. A. Morrison and J. D. Bruno, "Resonant level lifetime in GaAs/AlGaAs double-barrier structures," *Appl. Phys. Lett.* **51**, pp. 1089-1090, 1987.

[7] J. -W. Choe, H. -J. Hwang, A. G. U. Perera, S. G. Matsik and M. H. Francombe, "Resonant tunneling times in superlattice structures," *J. Appl. Phys.* **79**, pp. 7510-7513, 1996.

[8] B. Jonsson and S. T. Eng, "Solving the Schrödinger Equation in arbitrary quantum-well profiles using the transfer matrix method," *IEEE J. Quant. Electron.* **26**, pp. 2025-2035, 1990.

[9] G. Bastard, "Superlattice band structure in the envelope-function approximation," *Phys. Rev. B* **24**, pp. 5693-5697, 1981.

[10] T. Tamir and F. Y. Kou, "Varieties of leaky waves and their excitation along multilayer structures," *IEEE J. Quant. Electron.* **22**, pp. 544-551, 1986.

[11] R. V. Churchill, J. W. Brown and R. F. Verhey, *Complex Variables and Applications*, 3rd ed., McGraw-Hill, 1974.

[12] L. M. Delves and J. N. Lyness, "A numerical method for locating the zeros of an analytic function," *Math. Comp.* **21**, pp. 543-560, 1967.

[13] L. M. Delves and J. N. Lyness, "On numerical contour integration round a closed contour," *math. Comp.* **21**, pp. 561-577, 1967.

[14] W. H. Press, B. P. Flannery, S. A. Teukolsky and W. T. Vetterling, *Numerical Recipes in C*, Cambridge Univ. Press, 1988.

[15] H. -P. Nolting, G. Szetefka, M. Grawert and J. Ctyroky, "Wave propagation in a waveguide with a balance of gain and loss," OSA Integrated Photonics Research (IPR96), 1996.

Chapter 3

Optical Waveguiding Properties of Quantum Cascade Lasers

3.1 Introduction

In this chapter, the optical-waveguide properties of the Quantum Cascade Laser (QCL) [1] are analysed and discussed. Intersubband transitions involve predominantly TM-polarised light, where the electric field is perpendicular to the epitaxial layers, although some weak TE-polarised transitions are possible under certain circumstances [2]. The interface between the metal contact and semiconductor in the waveguide structure reported in [3] may also support the so-called surface plasmon modes, or electromagnetic surface modes, which are highly lossy, and hence, for most cases, any coupling between the plasmon mode and the lasing (guided) mode should be avoided. It has, conversely, been argued [4] that the use of plasmon modes is an effective method for obtaining waveguiding. In that work, a metal contact layer (palladium) with a larger imaginary refractive index component than, e.g., gold or silver

which are the metals usually used for contacts, is utilised to increase the reflection coefficient at the guiding interfaces, so that the penetration of the mode into the metal, and hence the losses at the interface, is reduced.

The modes supported by the metal-semiconductor interface of the QCL waveguide can be modelled using the method of solving the Helmholtz equation for optical fields, which was introduced in Chapter 2.

3.1.1 Electromagnetic Surface Waves (Surface Plasmons)

A surface wave is a mode of propagation which is confined to the immediate vicinity of the interface between two semi-infinite media [5]. For example, the occurence of ripples in water can be thought of as a surface wave guided by the interface between air and water. The electromagnetic surface wave, however, occurs at the interface between a dielectric and a metal, and was first suggested by Kossel [6], when he postulated the existence of "surface states" near the interface between a periodic dielectric layered medium and a dielectric homogenous one. Both TE and TM modes can be supported, and many modes may exist at a given frequency ω.

Electromagnetic surface waves can also exist at the interface between two media, provided the dielectric constants of the media are opposite in sign (e.g. air and silver). In this case, only a single TM mode exists at a given frequency [5]. The amplitude of the wave decreases exponentially in the two directions normal to the interface as illustrated in Figure 3.1. The modes are also called surface plasmon waves because of the electron-plasma contribu-

PAGE/PAGES EXCLUDED UNDER INSTRUCTION FROM UNIVERSITY

is defined as the fraction of the optical energy that is confined in the active region of the waveguide. The modal gain may then be found from the expression $g_{modal} = \Gamma g$. However, using the complex energy method described previously, the modal gain may be *directly* calculated from the imaginary part of the complex propagation coefficient, i.e. the attenuation coefficient, α. This method is therefore more accurate than the traditional one.

3.2 The QCL Waveguide

In a conventional semiconductor laser, the epitaxial layers grown on either side of the active region are usually chosen to form a waveguide normal to these layers. This techinique has also been used in the QCL [3], [8]. The epitaxial layers grown adjacent to the active layer of a semiconductor layer ensure that most of the light propagates in the active layer. The active region forms the central core layer of the multilayer waveguide, as shown in Figure 3.2.

For the TM-polarised light emitted by a QCL, only three field components (E_x, H_y, E_z) need to be considered in the waveguide analysis. The TM modes supported by an optical waveguide can be found using the transfer matrix method, and Argument Principle Method (APM) described in Chapter 2, using the appropriate parameters for TM configuration.

The structures shown in in Figures 3.3 and 3.4 have been analysed [9] and both are found to be multi-moded. Figure 3.3 shows the original waveguide structure used in [3], while Figure 3.4 shows an alternative design proposed

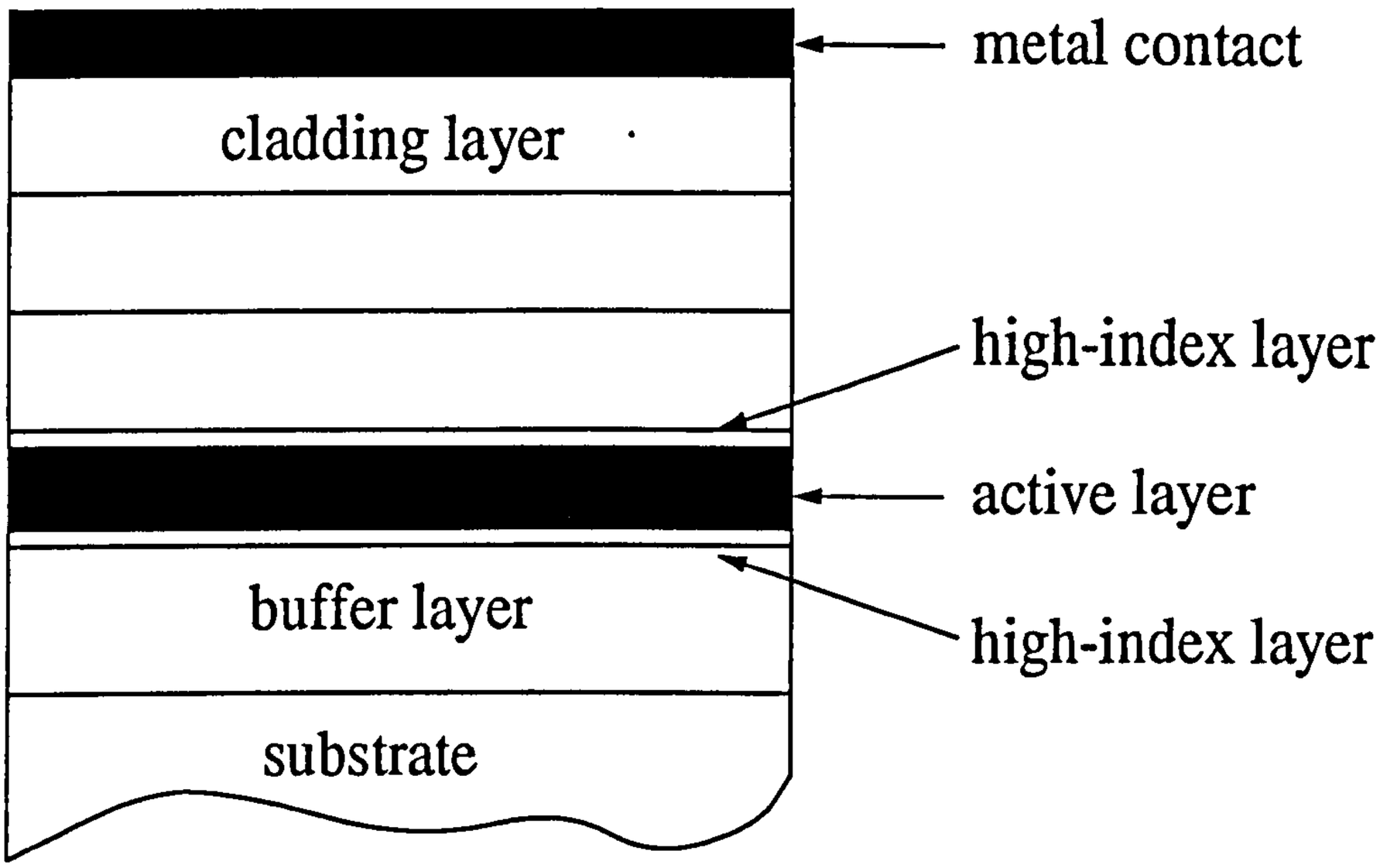

Figure 3.2: Schematic diagram of the layer structure of a typical quantum cascade laser.

in [7] after a sensitivity analysis of the waveguide, which is described in Section 3.6.

The details of the widths and relative permittivities of the two-layer structures being analysed are given in Table 3.1, part of these values were taken from [9]. All calculations assume a gold interface contact and that the imaginary part of the relative permittivity of the active region is equivalent to a local gain of 50 cm^{-1}. All other epitaxial layers have been taken to be passive. A lasing wavelength of 4.65 μm has been assumed.

The primary purpose of the two thin layers of high refractive index on both sides of the active layer of Figure 3.3, is to increase the confinement of

PAGE/PAGES EXCLUDED UNDER INSTRUCTION FROM UNIVERSITY

the optical power in the active region, and hence reduce the coupling to the lossy surface mode. The structure from [3] was found to support two modes, and the value of the complex propagation coefficients are given in Table 3.1. The modal intensities of the two modes are shown in Figure 3.5. In the following analysis it will be shown that the high-index layer nearest the metal primarily controls the interaction between the bound modes and the surface plasmon; and that, similiarly, the other high-index layer near the substrate influences the interaction with the active region. The combined widths of the high-index layers will also be shown to be the primary indication of the degree of confinement of higher-order modes.

3.3 Proposed Waveguide Design

If the high-refractive-index layer nearest the metal contact is removed, the resulting simpler structure (Figure 3.4) has slightly improved propagation characteristics compared with those of the original design, as shown in Table 3.1. The remaining high-index layer pulls the peak of the fundamental mode towards the substrate, and thereby improves the confinement of the fundamental mode in the active region, while simultaneously reducing the confinement of the first-order mode in the active layer. So, the gain experienced by the fundamental mode is larger than that of the original case, and, the gain of the first-order mode is reduced, in comparison with the original design.

The removal of the high-index layer nearest the metal contact has two

Table 3.1: Thickness and real part of the relative permittivity of the epitaxial layers that make up the two waveguide structures being investigated.

Original design [3]								
Epitaxial layer	1	2	3	4	5	6	7	8	9
Thickness (μm)	-	1.24	0.50	0.74	0.24	1.24	0.24	1.80	-
Refractive index	2.50	2.92	3.17	3.20	3.47	3.39	3.47	3.04	3.04
	Fundamental mode					First-order mode			
	n_{eff}		cm^{-1}			n_{eff}		cm^{-1}	
	3.2998		9.3706			3.0951		1.9805	

Proposed design								
Epitaxial layer	1	2	3	4	5	6	7	8
Thickness (μm)	-	1.24	0.50	0.74	1.24	0.24	1.80	-
Refractive index	2.50	2.92	3.17	3.20	3.39	3.47	3.04	3.04
	Fundamental mode				First-order mode			
	n_{eff}		cm^{-1}		n_{eff}		cm^{-1}	
	3.2875		9.5415		3.0792		1.1235	

The effective index and modal gain of the two modes supported by each waveguide are given. The complex reflectivity of gold was taken to be $(1.086 - j33.57)$.

favourable effects on the propagation coefficients of the two modes supported (Table 3.1). The modal profiles are shown in Figure 3.6. It is expected that the proposed waveguide structure will have the following beneficial effects on overall device performance: (i) it will reduce the threshold current, and (ii) it will suppress the excitation of higher-order modes and thereby improve the near and far-field optical profiles.

3.4 Sensitivity Analysis

The sensitivity of the above structures in Figures 3.3 and 3.4 to small perturbations has also been investigated. The effect that small changes in the width and relative permittivity of various layers have on the propagation coefficient are shown in Table 3.2, where the changes in the imaginary part of the propagation coefficient induced by each perturbation have been expressed in terms of the modal gain, and as a percentage change in the modal gain.

Some general observations can be made about the data in Table 3.2. The two structures show the same degree of sensitivity to the perturbations. Also, in general, the modal gain experienced by the fundamental mode of the new structure (Figure 3.4) is larger than that of the original structure (Figure 3.3). The new structure is better at suppressing the first-order modes. In all cases, the first-order modes show the greatest sensitivity to the perturbations. These first-order modes are close to cut-off, and hence small perturbations in optical parameters have a greater effect.

Table 3.2: Modal gains calculated for both structures after altering (i) the active layer width by ±5% and ±1%, (ii) the real part of the relative permittivity of the active layer by ±1%, and (iii) the width of the high-index (H-I) layer(s) next to the active layer by ±1%.

	Modal gain							
	Fundamental mode				First-order mode			
	Original		Proposed		Original		Proposed	
	cm^{-1}	%	cm^{-1}	%	cm^{-1}	%	cm^{-1}	%
Unperturbed	9.3706	0.00	9.5415	0.00	1.9805	0.00	1.1235	0.00
Active width +5%	9.6289	2.75	9.8257	2.97	2.3988	21.1	0.2687	-76.0
Active width +1%	9.4235	0.56	9.5695	0.29	2.0651	4.27	-0.3845	-134.2
Active width −1%	9.3168	-0.57	9.4852	-0.58	1.9853	-4.30	1.0248	-8.75
Active width −5%	9.0946	-2.95	9.2542	-3.00	1.5499	-21.7	0.6298	-44.0
Active index +1%	9.6831	3.33	9.8147	2.87	2.2185	12.1	1.4726	31.1
Active index −1%	9.0246	-3.69	9.2447	-3.11	1.7549	-11.4	0.7759	-31.0
H-I layer +1%	9.5050	1.43	9.5341	-0.07	1.2144	-38.6	1.1414	1.64
H-I layer −1%	9.6185	2.65	9.5478	0.07	1.110	-44.0	1.1045	-1.64

The actual gain of each mode and its percentage difference from the unperturbed case are given.

Variations in the width of the active layer show one surprising result. The modal gain experienced by the first-order mode of the new structure goes through a minimum as the active layer is increased, while the modal gain of the fundamental mode increases with active-layer width. This behaviour is not observed in the original design, where both modal gains simply increase with active-layer width.

An increase in the value of the refractive index of the active layer increases the modal gain of all the modes, and there is no appreciable difference in the performance of the two structures to this type of perturbation. As would be expected, increasing the refractive index of the active layer raises the optical confinement in this layer. But in doing so, care must naturally be taken to avoid the onset of higher-order modes.

The results in Table 3.2 also indicate that there is an optimum value for the width of the high-index layer used in the new design. Increasing the thickness of the high-index layer causes a reduction in the modal gain of the fundamental mode, as more of the mode is guided in the high-index layer. The data in Tables 3.2 and 3.3 indicate that there are also optimum widths for the two high-index layers used in the original structure.

In Table 3.3 the changes in the modal gain of both modes of the original structure, caused by independent variations in the width of the high-index layers, are presented. Increasing the width of the high-index layer nearest the substrate causes a decrease in the modal gain of both modes. Chang-

Table 3.3: Effect of independently changing the widths of the high-index (H-I) layers on both sides of the active layer of the structure of [3].

	Modal Gain			
	Fundamental mode		First-order mode	
	cm^{-1}	%	cm^{-1}	%
Unperturbed	9.3706	0.00	1.9805	0.00
H-I layer nearest the metal +5%	9.3409	-0.31	2.0443	3.22
H-I layer nearest the metal +1%	9.3647	-0.06	1.9933	0.65
H-I layer nearest the metal −1%	9.3763	0.06	1.9676	-0.65
H-I layer nearest the metal −5%	9.3989	0.30	1.9157	-3.27
H-I layer nearest the substrate +5%	9.3726	0.02	2.0151	1.74
H-I layer nearest the substrate +1%	9.3710	~0.0	1.9875	0.35
H-I layer nearest the substrate −1%	9.3699	~0.0	1.9733	-0.36
H-I layer nearest the substrate −5%	9.3669	-0.04	1.9444	-1.82

Both the actual gain of each mode and its percentage difference from the unperturbed case are given.

ing the width of this layer primarily alters the degree of interaction which both modes have with the active region. In contrast, varying the width of the other high-index layer nearest the metal has a more complicated effect. Increasing the width of this layer reduces the modal gain of the fundamental but increases the modal gain of the first-order mode. The converse is true if the width is reduced. The high-index layer nearest the metal contact primarily increases the interaction of the fundamental modes with the metal surface contact by pulling the mode closer to the contact. Any increase in the width of either of the high-index layers causes the first-order mode to be more tightly bound, and thus increases its modal gain. These results show that ony the high-index layer nearest the substrate is required to improve the guiding of the fundamental mode. The other high-index layer primarily assists in guiding the first-order mode. These effects explain the improved performance of the new structure.

Increasing the refractive index of either or both of the high-index layers in either structure causes minimal changes because these layer are relatively thin. Assuming that all the epitaxial layers (except the active layer) are lossy causes reductions in the modal gains consistent with the assumed attenuation. As would be expected, reducing the optical wavelength causes all the modes to be more tightly bound, i.e. more of the optical power is confined to the core regions, and the power also decays more rapidly outside the core waveguide layers, resulting in increased modal gains.

3.5 Conclusion

The basic multilayer optical-waveguide structure used in the majority of quantum cascade laser devices has been investigated, and has been shown to be multimoded. A complex-waveguide analysis was undertaken using the transfer-matrix method and the APM described in Chapter 2. The effect of small perturbations in the optical parameters on the complex propagation coefficient has been studied.

This analysis has shown that a more efficient waveguide structure can be obtained by the simple expedient of removing the high-index layer nearest the metal contact from the original design of [3], in the sense that not only has it resulted in a better guided and more confined fundamental mode with a higher modal gain, but also a weaker first-order mode, in comparison to the original design. In subsequent chapters, studies will be conducted of the active region section where the lasing processes take place.

References

[1] J. Faist, F. Capasso, D. L. Sivco, C. Sirtori, A. L. Hutchinson and A. Y. Cho, "Quantum cascade laser," *Science*, **264**, pp. 553-556, 1994.

[2] R. Q. Yang, J. M. Xu and M. Sweeny, "Selection rules of intersubband transitions in conduction-band quantum wells," *Phys. Rev. B* **50**, pp. 7474-7482, 1994.

[3] J. Faist, F. Capasso, D. L. Sivco, C. Sirtori, A. L. Hutchinson and A. Y. Cho, "Continuous wave operation of a vertical transition quantum cascade laser above $T = 80$K," *Appl. Phys. Lett.* **67** pp. 3057-3059, 1995.

[4] C. Sirtori, C. Gmachl, F. Capasso, J. Faist, D. L. Sivco, A. L. Hutchinson and A. Y. Cho, "Long-wavelength ($\lambda \approx 8-11.5\mu$m) semisonductor lasers with waveguides based on surface plasmons," *Optics Letts.* **23**, pp. 1366-1368, 1998.

[5] P. Yeh and A. Yariv, *Optical Waves in Crystals*, Chapters 6 and 11, John Wiley & Sons, 1984.

[6] D. Kossel, "Analogies between thin-film optics and electron-band theory of solids," *J. Optics Soc. Am.* **56**, 1434, 1966.

[7] P. S. Spencer, C. Y. L. Cheung and K. A. Shore, "Sensitivity analysis of the optical-waveguide properties of quantum cascade lasers," *IEE Proc.-Optoelectron.* **144**, pp. 323-326, 1997.

[8] C. Sirtori, J. Faist, F. Capasso, D. L. Sivco, A. L. Hutchinson and A. Y. Cho, "Quantum cascade laser with plasmon-enhanced waveguide operating at 8.4μm wavelength," *Appl. Phys. Lett.* **66**, pp. 3242-3244, 1995.

[9] P. S. Spencer and K. A. Shore, "Surface plasmon effects and waveguide properties of quantum cascade lasers," *IEE Proc.-Optoelectron.* **144**, pp. 48-52, 1997.

Chapter 4

Rate Equation Analysis and Threshold Conditions

4.1 Introduction

The performance of a semiconductor laser is defined by several parameters, which include its threshold current density, J_{th} and its light-current ($P-J$) characteristics. A study of these characteristics for a triple quantum well (TQW) intersubband structure, as illustrated in Figure 4.1, has been presented in [1], and will be discussed in this chapter, in order to determine the feasibility of achieving lasing action in such structures which utilise resonant tunneling to populate the upper level and depopulate the lower level of the lasing transition.

Utilisation of the four-level rate equations to predict the modulation response is investigated here. Analytical results for a symmetric structure presented in [2] [3] [4], and published in [5] will be discussed.

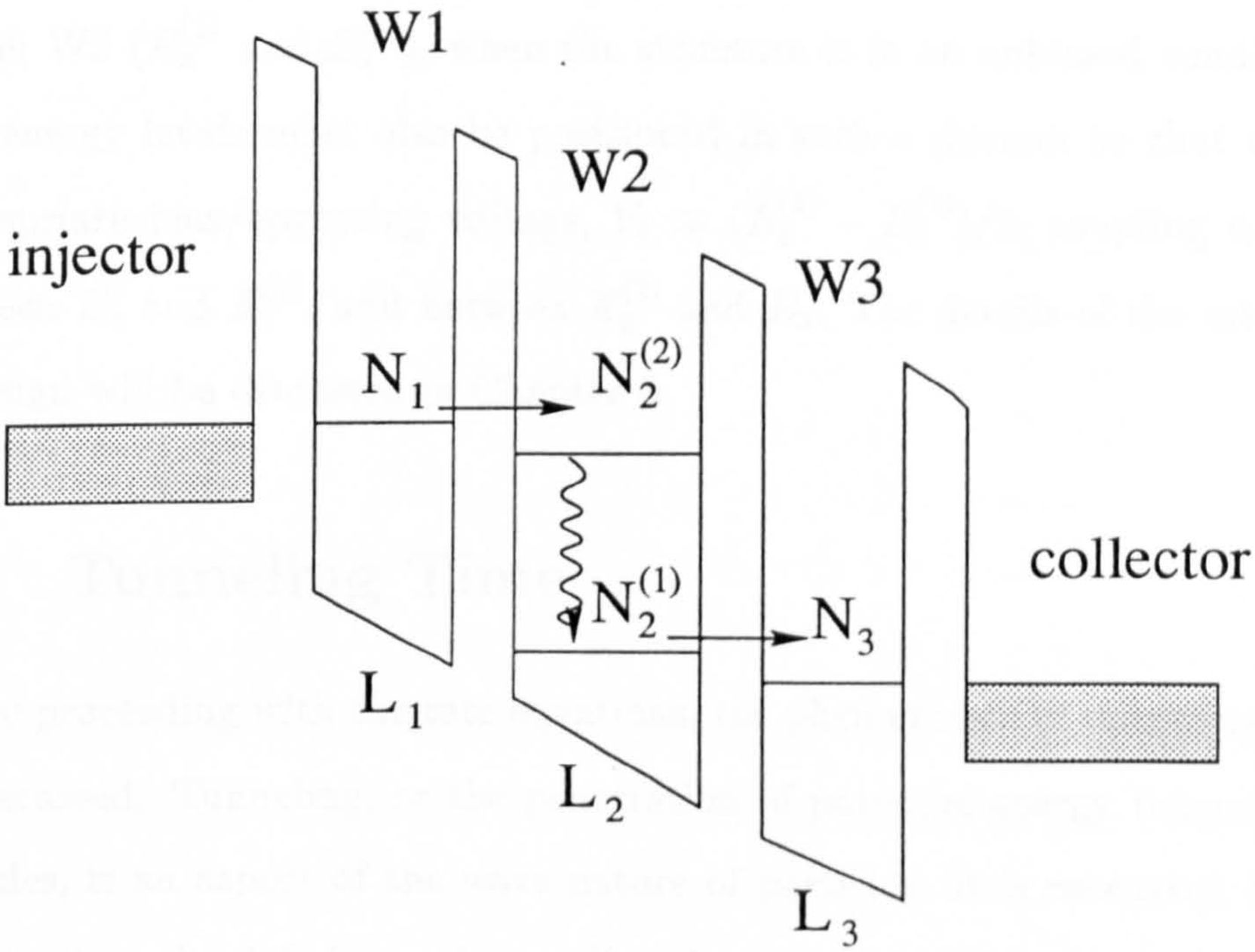

Figure 4.1: Schematic diagram of a nominal TQW structure with four energy levels.

The TQW intersubband structure shown in Figure 4.1 is essentially a four-level system. The lasing transition occurs in W2. Electrons are injected into the upper energy level of W2 through W1 and are removed from the lower energy level of W2 through W3, via resonant tunneling. The confined electrons undergo intersubband transitions such as stimulated radiative emission, absorption and intersubband relaxation. It is assumed that there are no carrier source or sink in the wells so that the injection current densities, J, entering and leaving the structure are the same.

In order to achieve this, the TQW structure is designed such that its four

lowest energy levels are localised one each in W1 (E_1) and W3 (E_3), and two in W2 ($E_2^{(1)}$ and $E_2^{(2)}$), when the structure is in an unbiased condition. The energy levels must also be positioned in such a manner so that at an appropriate bias/operating voltage, $V_b \approx (E_2^{(2)} - E_2^{(1)})/2$, coupling occurs between E_1 and $E_2^{(1)}$, and between $E_2^{(2)}$ and E_3. The details of the method of design will be discussed in Chapter 5.

4.2 Tunneling Time

Before proceeding with the rate equations, the phenomenon of tunneling will be discussed. Tunneling, or the penetration of potential energy barriers by particles, is an aspect of the wave nature of particles. It is necessary, however, to state the definition of *tunneling time* as used in this chapter, and in the remainder of this thesis, to avoid confusion, as there are several definitions available in the literature. The state lifetime mentioned previously in Chapter 2 is one such phenomenon which has been given the name of this all-encompassing term. The definition used here, however, is similiar to that used by Choe *et al* [6], and Künz *et al* [7] which is that of *resonant* tunneling, and is defined as the time it takes an electron to travel from one side of the barrier in one well to the other side of the barrier in the other well when the wells are coupled together.

Coherent resonant tunneling not only occurs when the energy levels of the relevant states (E_1 and $E_2^{(1)}$, as well as $E_2^{(2)}$ and E_3, in this case) coincide. It is rather a resonant phenomenon leading to maximum tunneling currents in the case of exact alignment, but also taking place for small de-

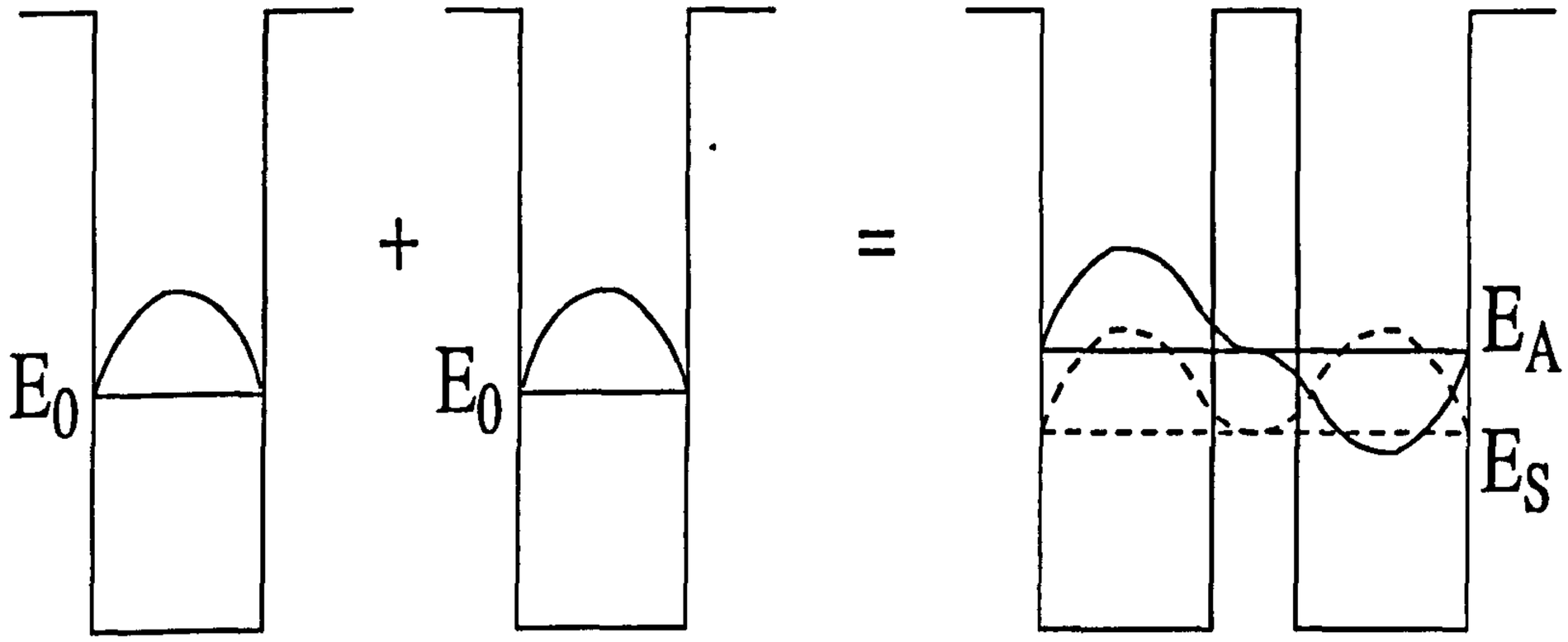

Figure 4.2: Two identical single QWs, each with a a single energy level are shown. Combining, or coupling, the two wells and leaving a thin barrier between the wells yields a double QW structure, with two energy levels, and wavefunctions which take the forms as shown, and results in an energy level splitting $\Delta E = E_A - E_S$ between the two energy levels, where $E_A > E_0 > E_S$.

viations [8]. Figure 4.2 illustrates what happens when two wells are coupled together. For simplicity, two identical wells are used in the example, but two wells with energy levels which coincide, either through the application of a bias voltage or by design, can also be coupled. Exact alignment, and hence maximum tunneling current, occurs when the energy level splitting, ΔE, is at a minimum value, ΔE_{min}. For the identical wells shown in Figure 4.2, ΔE is automatically at that minimum value, but in the case where alignment has to be achieved through the application of a bias voltage, for example, then there may be some slight deviation. The stronger the coupling strength, the greater this minimum value, ΔE_{min}. A time-evolution simulation using the *time-dependent* Schrödinger equation would show the two wavefunctions oscillating between the wells. The characteristic time for this tunneling may

then be found from the following expression [7]:

$$\tau_{tun} = \frac{\pi\hbar}{\Delta E} \tag{4.1}$$

4.3 Rate Equations

The dynamics of the electron densities in the respective energy levels are described by the four-level rate equations which are given below [9], [10]:

$$\frac{\mathrm{d}N_1}{\mathrm{d}t} = \frac{J}{eL_1} + \frac{L_2}{L_1}\frac{N_2^{(2)}}{\tau_{12}} - \frac{N_1}{\tau_{12}} \tag{4.2}$$

$$\frac{\mathrm{d}N_2^{(2)}}{\mathrm{d}t} = \frac{L_1}{L_2}\frac{N_1}{\tau_{12}} - \frac{N_2^{(2)}}{\tau_{12}} - aP\left(N_2^{(2)} - N_2^{(1)}\right) - \frac{N_2^{(2)}}{\tau_S} \tag{4.3}$$

$$\frac{\mathrm{d}N_2^{(1)}}{\mathrm{d}t} = aP\left(N_2^{(2)} - N_2^{(1)}\right) + \frac{N_2^{(2)}}{\tau_S} + \frac{L_3}{L_2}\frac{N_3}{\tau_{23}} - \frac{N_2^{(1)}}{\tau_{23}} \tag{4.4}$$

$$\frac{\mathrm{d}N_3}{\mathrm{d}t} = \frac{L_2}{L_3}\frac{N_2^{(1)}}{\tau_{23}} - \frac{N_3}{\tau_{23}} - \frac{J}{eL_3} \tag{4.5}$$

$$\frac{\mathrm{d}P}{\mathrm{d}t} = aP\left(N_2^{(2)} - N_2^{(1)}\right) - \frac{P}{\tau_P} \tag{4.6}$$

where $N_i^{(j)}$ denotes the electron density in Well i ($i = 1, 2, 3$) and energy level j - as there is only one energy level in W1 and W3, the superscript j is omitted. e is the electronic charge, a is the local gain parameter, P is the photon density, and τ_S is the intersubband relaxation time. L_1, L_2 and L_3 are the widths of the three wells respectively, $aP(N_2^{(2)} - N_2^{(1)})$ is the stimulated emission term and $N_2^{(2)}/\tau_S$ is the spontaneous emission term, while the optical losses are denoted by P/τ_P, where τ_P is the photon lifetime.

The tunneling times τ_{12} and τ_{23}, between W1 and W2, and between W2 and W3 respectively, are given by

$$\tau_{12} = \frac{\pi\hbar}{\Delta E_{12}} \qquad \tau_{23} = \frac{\pi\hbar}{\Delta E_{23}} \tag{4.7}$$

where $\hbar$ is Planck's constant divided by 2π, and ΔE_{12}, ΔE_{23} are the energy level splittings due to the coupling of W1 and W2, and W2 and W3 respectively. The stronger the coupling strength between the wells, the larger the possible energy separation, hence resulting in faster tunneling time through the barrier, as may be deduced from Equation (4.7) above.

Since the current injection is equal to the rate of total charge passing through the resonant tunneling quantum well structure, the following expression may be obtained:

$$J = \frac{e}{\tau_T}\left[N_1 L_1 + (N_2^{(1)} + N_2^{(2)})L_2 + N_3 L_3\right] \tag{4.8}$$

where τ_T is the effective transit time of the carriers through the whole structure, which includes not only the tunneling times through the barriers and the intersubband transition times, but also the time delays caused by intraenergy level scattering and electron diffusion, and J is the injection current density.

4.4 Population Inversion Condition

In order to find the population inversion condition, $(N_2^{(2)} - N_2^{(1)}) > 0$, and the threshold current, J_{th}, the rate equations must be solved using steady-state conditions and at threshold. At steady state, the rates of change of

the carrier densities, dN_i/dt are equivalently zero, and at threshold there is no lasing so the photon density, $P = 0$. The carrier rate equations therefore take the form:

$$\frac{J}{eL_1} + \frac{L_2}{L_1}\frac{N_2^{(2)}}{\tau_{12}} - \frac{N_1}{\tau_{12}} = 0 \tag{4.9}$$

$$\frac{L_1}{L_2}\frac{N_1}{\tau_{12}} - \frac{N_2^{(2)}}{\tau_{12}} - \frac{N_2^{(2)}}{\tau_S} = 0 \tag{4.10}$$

$$\frac{N_2^{(2)}}{\tau_S} + \frac{L_3}{L_2}\frac{N_3}{\tau_{23}} - \frac{N_2^{(1)}}{\tau_{23}} = 0 \tag{4.11}$$

$$\frac{L_2}{L_3}\frac{N_2^{(1)}}{\tau_{23}} - \frac{N_3}{\tau_{23}} - \frac{J}{eL_3} = 0 \tag{4.12}$$

while the photon rate equation becomes

$$\begin{aligned} P\left[a(N_2^{(2)} - N_2^{(1)}) - \frac{1}{\tau_P}\right] &= 0 \\ \Delta N &= \frac{1}{a\tau_P} \end{aligned} \tag{4.13}$$

where $\Delta N = (N_2^{(2)} - N_2^{(1)})$.

After some mathematical manipulations, the details of which are in Appendix B, an expression for ΔN is obtained:

$$\Delta N = \frac{J}{eL_2}[4\tau_S + \tau_{12} - \tau_{23} - \tau_T] \tag{4.14}$$

where J is the current density at, and below, lasing threshold. An expression for the threshold current density may be found in a straightforward manner, by substituting the expression for ΔN from Equation (4.13) into the above

equation:

$$\frac{1}{\tau_P} = \frac{J_{th}}{eL_2}[4\tau_S + \tau_{12} - \tau_{23} - \tau_T]$$

$$J_{th} = \frac{2eL_2}{a\tau_P}\frac{1}{4\tau_S + \tau_{12} - \tau_{23} - \tau_T} \tag{4.15}$$

while the population inversion condition, where $\Delta N > 0$ is given by

$$\frac{J}{eL_2}[4\tau_S + \tau_{12} - \tau_{23} - \tau_T] > 0$$

$$4\tau_S + \tau_{12} - \tau_{23} - \tau_T > 0 \tag{4.16}$$

This condition provides design rules for selecting appropriate TQW structures and operating conditions to achieve population inversion. It is noted that the above conditions may be unnecessarily restrictive since, on the basis of work by Faist and Capasso [11], there are some cases in which so-called inversionless lasing may occur. Treatment of that case is not, however, within the scope of this thesis.

4.5 Light-Current Characteristics

In order to find the $P - J$ characteristics, conditions at steady state above threshold should be considered, so the carrier rate equations become:

$$\frac{J}{eL_1} + \frac{L_2}{L_1}\frac{N_2^{(2)}}{\tau_{12}} - \frac{N_1}{\tau_{12}} = 0 \tag{4.17}$$

$$\frac{L_1}{L_2}\frac{N_1}{\tau_{12}} - \frac{N_2^{(2)}}{\tau_{12}} - aP\left(N_2^{(2)} - N_2^{(1)}\right) - \frac{N_2^{(2)}}{\tau_S} = 0 \tag{4.18}$$

$$aP\left(N_2^{(2)} - N_2^{(1)}\right) + \frac{N_2^{(2)}}{\tau_S} + \frac{L_3}{L_2}\frac{N_3}{\tau_{23}} - \frac{N_2^{(1)}}{\tau_{23}} = 0 \tag{4.19}$$

$$\frac{L_2}{L_3}\frac{N_2^{(1)}}{\tau_{23}} - \frac{N_3}{\tau_{23}} - \frac{J}{eL_3} = 0 \tag{4.20}$$

The photon rate equation is still of the form in Equation (4.13). From these, an expression for the current density is found

$$J = \frac{2eL_2(1+2aP\tau_S)}{a\tau_P(4\tau_S+\tau_{12}-\tau_{23}-\tau_T)} \tag{4.21}$$

so that when considered together with Equation (4.15), the photon density in terms of the current density and the threshold current density, see Appendix B, takes the form:

$$P = \frac{1}{2a\tau_S}\left(\frac{J}{J_{th}} - 1\right) \tag{4.22}$$

Using Equation (4.22), the idealised linear light output power versus injection current density characteristics is shown in Figure 4.3, for the parameters given in Table 4.1. The values for the photon lifetime, τ_P, and the local gain parameter, a, were taken from [9] and [10], whereas the tunneling times τ_{12} and τ_{23} were calculated from Equation (4.7) using the method which will be described in Chapter 5. The value for τ_S is within the estimates of 1-3 ps given in the literature [10], [12].

These results serve as the basis for a small signal analysis of the modulation response of the laser, which will be described in the next section.

Table 4.1: Parameters for the calculation of the $P - J$ dependence.

Local gain parameter, a	1.0×10^{-5} cm^{-3}
Tunneling time from W1 to W2, τ_{12}	0.52 ps
Tunneling time from W2 to W3, τ_{23}	0.50 ps
Inter-energy level relaxation time, τ_S	2.0 ps
Photon lifetime, τ_P	1.0 ps
Transit time, τ_T	3.2 ps
Width of W2, L_2	8.3 nm

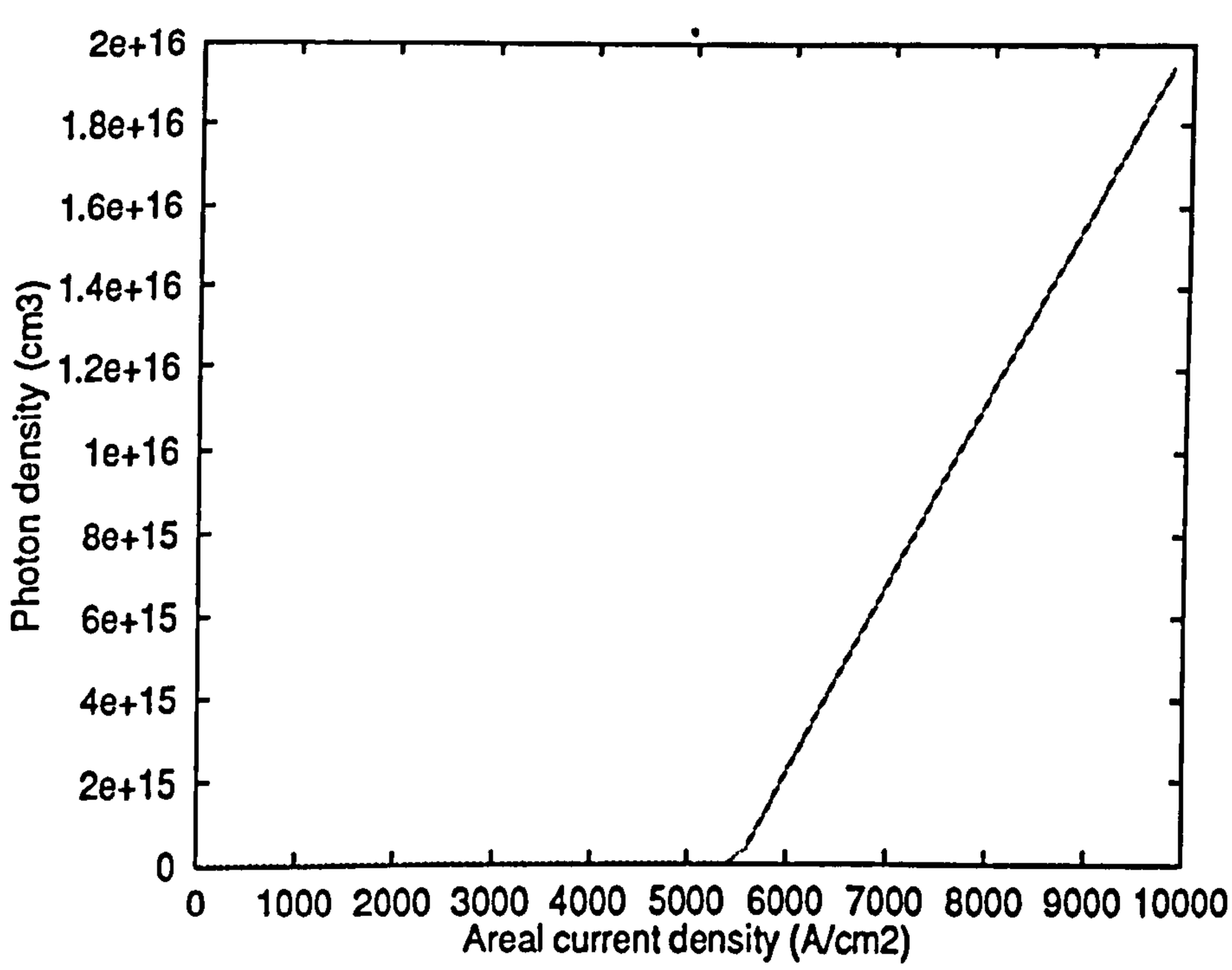

Figure 4.3: The variation of the photon density with the current density. The threshold current density, $J_{th} = 5520$ A/cm^2.

4.6 Small Signal Analysis and Modulation Response

A small signal analysis is performed on the rate equations, where a modulation current, $J_m(t) = J_m \cos(\omega_m t)$ is superimposed upon the pre-bias current J_b, giving rise to variations in the steady state values of the carrier and photon densities of the form $N = \bar{N}_i + n_i$ and $P = \bar{P} + p$, so the rate equations are then rewritten as

$$\frac{\mathrm{d}(\bar{N}_1 + n_1)}{\mathrm{d}t} = \frac{J_b + J_m(t)}{eL_1} + \frac{L_2}{L_1}\frac{(\bar{N}_2^{(2)} + n_2^{(2)})}{\tau_{12}} - \frac{(\bar{N}_1 + n_1)}{\tau_{12}} \tag{4.23}$$

$$\begin{aligned}\frac{\mathrm{d}(\bar{N}_2^{(2)} + n_2^{(2)})}{\mathrm{d}t} &= -aP\Big((\bar{N}_2^{(2)} + n_2^{(2)}) - (\bar{N}_2^{(1)} + n_2^{(1)})\Big) + \frac{L_1}{L_2}\frac{(\bar{N}_1 + n_1)}{\tau_{12}} \\ &\quad - \frac{(\bar{N}_2^{(2)} + n_2^{(2)})}{\tau_{12}} - \frac{(\bar{N}_2^{(2)} + n_2^{(2)})}{\tau_S}\end{aligned} \tag{4.24}$$

$$\begin{aligned}\frac{\mathrm{d}(\bar{N}_2^{(1)} + n_2^{(1)})}{\mathrm{d}t} &= aP\Big((\bar{N}_2^{(2)} + n_2^{(2)}) - (\bar{N}_2^{(1)} + n_2^{(1)})\Big) + \frac{L_3}{L_2}\frac{(\bar{N}_3 + n_3)}{\tau_{23}} \\ &\quad - \frac{(\bar{N}_2^{(1)} + n_2^{(1)})}{\tau_{23}} + \frac{(\bar{N}_2^{(2)} + n_2^{(2)})}{\tau_S}\end{aligned} \tag{4.25}$$

$$\frac{\mathrm{d}(\bar{N}_3 + n_3)}{\mathrm{d}t} = \frac{L_2}{L_3}\frac{(\bar{N}_2^{(1)} + n_2^{(1)})}{\tau_{23}} - \frac{(\bar{N}_3 + n_3)}{\tau_{23}} - \frac{J_b + J_m(t)}{eL_3} \tag{4.26}$$

$$\frac{\mathrm{d}P}{\mathrm{d}t} = aP\Big((\bar{N}_2^{(2)} + n_2^{(2)}) - (\bar{N}_2^{(1)} + n_2^{(1)})\Big) - \frac{P}{\tau_P} \tag{4.27}$$

$$J_b + J_m(t) = \frac{e}{\tau_T}\Big[(\bar{N}_1 + n_1)L_1 + ((\bar{N}_2^{(1)} + n_2^{(1)}) + (\bar{N}_2^{(2)} + n_2^{(2)}))L_2 + (\bar{N}_3 + n_3)L_3\Big] \tag{4.28}$$

where $\bar{N}_i$ and $\bar{P}$ denote the steady state values of the carrier and photon densities respectively, while n_i and p denote the small perturbations in the steady state values of the carrier and photon densities. The above equations may be simplified, as the rate of change of the steady state carrier and photon densities are identically zero at steady state, and the 2nd order perturbations are negligible. And so,

$$\frac{\mathrm{d}n_1}{\mathrm{d}t} = \frac{J_m(t)}{eL_1} + \frac{L_2}{L_1}\frac{n_2^{(2)}}{\tau_{12}} - \frac{n_1}{\tau_{12}} \tag{4.29}$$

$$\begin{aligned}\frac{\mathrm{d}n_2^{(2)}}{\mathrm{d}t} &= \frac{L_1}{L_2}\frac{n_1}{\tau_{12}} - \frac{n_2^{(2)}}{\tau_{12}} - ap\bar{N}_d - a\bar{P}n_d - \frac{n_2^{(2)}}{\tau_S} \\ &= \frac{L_1}{L_2}\frac{n_1}{\tau_{12}} - \frac{n_2^{(2)}}{\tau_{12}} - \frac{p}{\tau_P} - a\bar{P}n_d - \frac{n_2^{(2)}}{\tau_S}\end{aligned} \tag{4.30}$$

$$\begin{aligned}\frac{\mathrm{d}n_2^{(1)}}{\mathrm{d}t} &= ap\bar{N}_d + a\bar{P}n_d + \frac{n_2^{(2)}}{\tau_S} + \frac{L_3}{L_2}\frac{n_3}{\tau_{23}} - \frac{n_2^{(1)}}{\tau_{23}} \\ &= \frac{p}{\tau_P} + a\bar{P}n_d + \frac{n_2^{(2)}}{\tau_S} + \frac{L_3}{L_2}\frac{n_3}{\tau_{23}} - \frac{n_2^{(1)}}{\tau_{23}}\end{aligned} \tag{4.31}$$

$$\frac{\mathrm{d}n_3}{\mathrm{d}t} = \frac{L_2}{L_3}\frac{n_2^{(1)}}{\tau_{23}} - \frac{n_3}{\tau_{23}} - \frac{J_m(t)}{eL_3} \tag{4.32}$$

$$\begin{aligned}\frac{\mathrm{d}p}{\mathrm{d}t} &= ap\bar{N}_d + a\bar{P}n_d - \frac{p}{\tau_P} \\ &= a\bar{P}n_d\end{aligned} \tag{4.33}$$

where $\bar{N}_d = \bar{N}_2^{(2)} - \bar{N}_2^{(1)} = 1/(a\tau_P)$ and $n_d = n_2^{(2)} - n_2^{(1)}$. Also, knowing from Equation (4.8) that $J_b = e/\tau_T(\bar{N}_1 L_1 + \bar{N}_s L_2 + \bar{N}_3 L_3)$, it can therefore be deduced from Equation (4.28) that

$$J_m(t) = e/\tau_T(n_1 L_1 + n_s L_2 + n_3 L_3) \tag{4.34}$$

where $\bar{N}_s = \bar{N}_2^{(2)} + \bar{N}_2^{(1)}$ and $n_s = n_2^{(2)} + n_2^{(1)}$.

The small analysis (Appendix B) results in a modulation response η which can be presented, using a resonance frequency ω_0 and a damping parameter γ, in the familiar form:

$$\eta = \frac{\frac{a\tau_T}{2eL_2}\left(\frac{1}{\tau_W} - \frac{1}{\tau_S}\right)J_m}{(\omega_0^2 - \omega_m^2) + j\omega_m\gamma} \tag{4.35}$$

From this expression the usual form for the maximum modulation frequency (MMF) can be deduced:

$$\omega = \sqrt{\omega_0^2 - \frac{\gamma^2}{2}} \tag{4.36}$$

However, due to the carrier transport dynamics of the structure under consideration, there are a number of novel features of the above expression. In the first place, the explicit forms of the resonance frequency and damping factor differ from those of conventional semiconductor lasers. In the present case, it is found that:

$$\omega_0^2 = \frac{2a\bar{P}}{\tau_P} \qquad \text{and} \qquad \gamma = 2a\bar{P} + \frac{1}{\tau_W} + \frac{1}{\tau_S} \tag{4.37}$$

where $\tau_W = \tau_{12} = \tau_{23}$. This special case was noted previously by Yee and Shore [10].

Calculations of the modulation response using the parameters shown in Table 4.2 shown in Figure 4.4 show that, due to the picosecond carrier lifetimes which are typical of such structures [13], terahertz modulation can be anticipated. It is further observed that the carrier lifetimes in such structures are typically of the same order as the photon lifetime. Here, in contrast with

Table 4.2: Parameters

Symbol	Meaning	Value
a	gain coefficient	$10^{-5}s^{-1}$
L_1	thickness of quantum well 1 (W1)	40 $\mathring{A}$
L_2	thickness of quantum well 2 (W2)	80 $\mathring{A}$
L_3	thickness of quantum well 3 (W3)	40 $\mathring{A}$
τ_W	tunneling times between W1/W2 and W2/W3	10 ps
τ_T	carrier transit time through the structure	125 ps
τ_S	intersubband relaxation time	30 ps
τ_P	photon lifetime	1 ps

interband semiconductor lasers, there s a finer balance between the contributions of the resonance frequency and damping factor in the determination of the maximum modulation frequency. The consequences of this observation are considered next.

4.6.1 Optical Output Power Optimisation

The first implication of the novel features of the transport dynamics of the intersubband laser is that the MMF does not increase monotonically as a function of the optical output power of the laser. The dependence is illustrated in Figure 4.5 for the case of laser emission at 10 μm. The existence of an optimised MMF can be readily demonstrated using Equation (4.36). In this way, the optimum output power for the device to achieve maximum

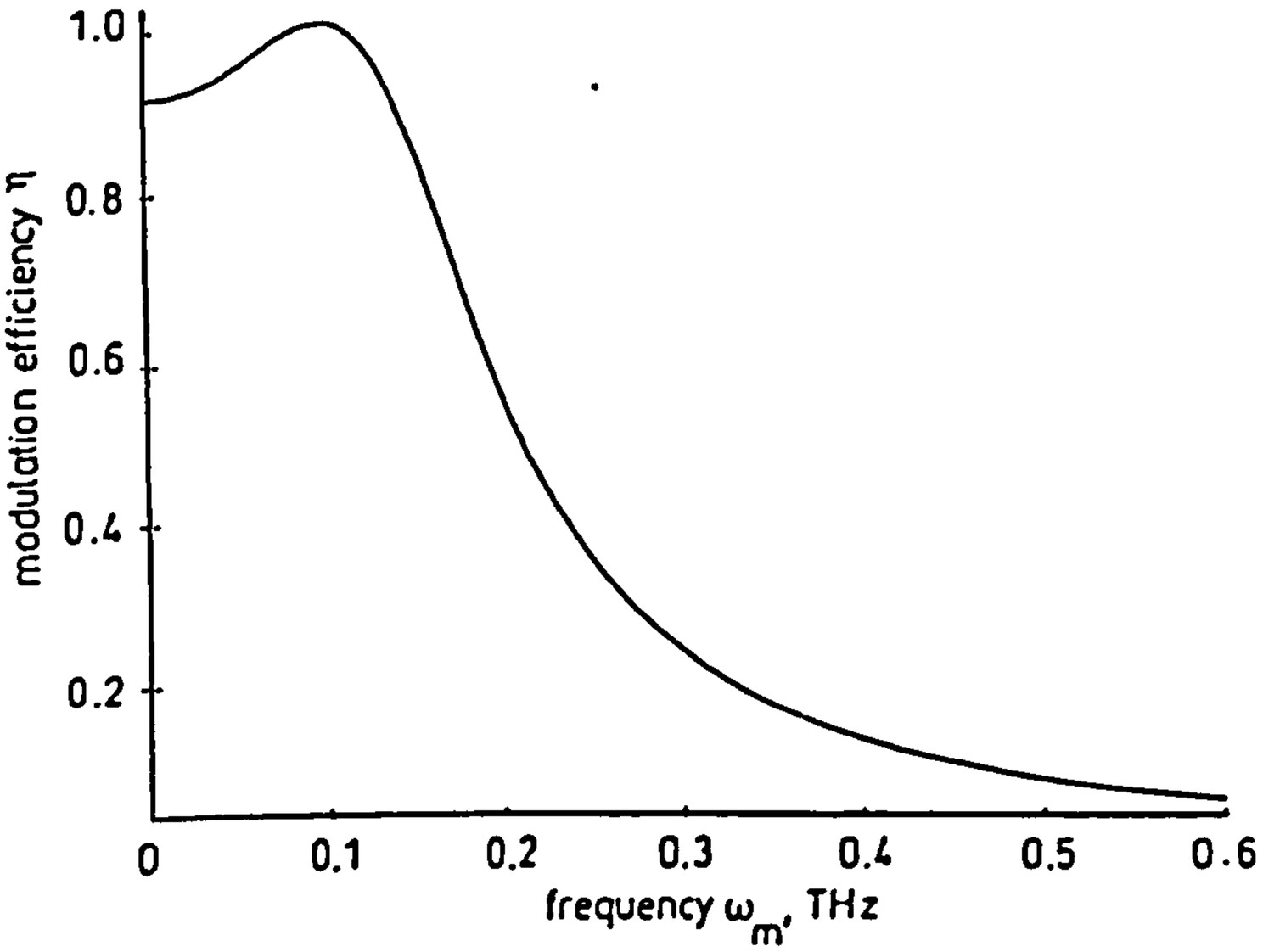

Figure 4.4: Direct current modulation response of intersubband laser.

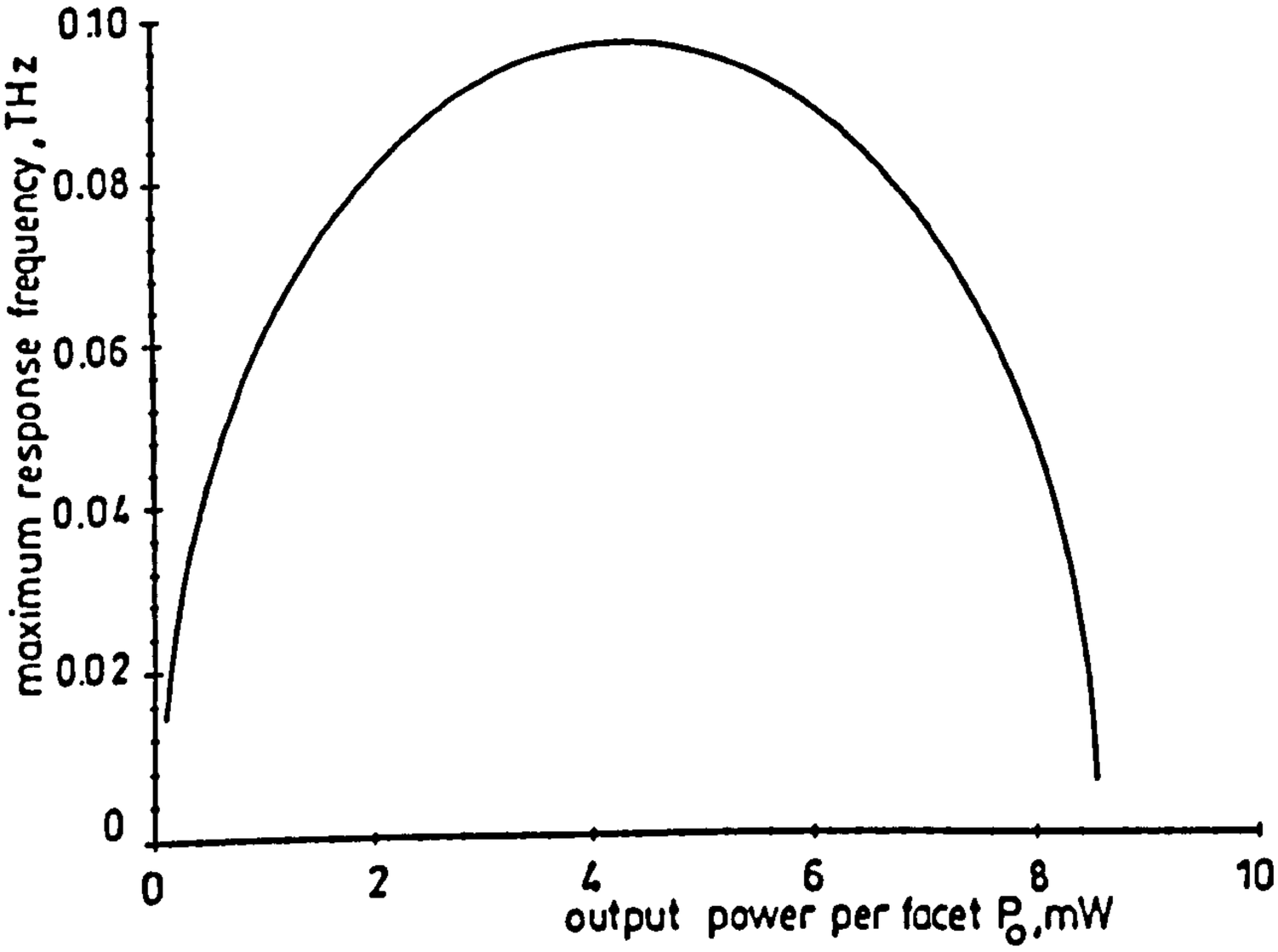

Figure 4.5: Maximum modulation frequency versus optical output power for a laser with emission wavelength of 10 μm.

modulation frequency can be found to be:

$$\bar{P}_{opt} = \left(\frac{1}{\tau_P} - \frac{1}{\tau_W} - \frac{1}{\tau_S}\right)\frac{1}{2a} \tag{4.38}$$

and the coresponding MMF is written explicitly as:

$$\omega_{max} = \sqrt{\frac{1}{\tau_P}\left(\frac{1}{2\tau_P} - \frac{1}{\tau_W} - \frac{1}{\tau_S}\right)} \tag{4.39}$$

4.6.2 Carrier Lifetime Optimisation

The maximum modulation frequency is also liable to optimisation with respect to carrier transport time constants. In turn these provide further guidelines for the design of coupled QW structures to be utilised in intersubband lasers. For this optimisation, care must be taken to ensure that lifetimes are consistent with the conditions for population inversion indicated in Equation (4.16). Considering the various time constants in turn, the following expressions for optimised MMF are obtained:

$$\omega_{max}^2 = \frac{2a\bar{P}}{\tau_P} - \frac{(2a\bar{P} + \frac{1}{\tau_W})^2}{2} \qquad \text{when } \tau_S \to \infty \tag{4.40}$$

$$\omega_{max}^2 = \frac{2a\bar{P}}{\tau_P} - \frac{(2a\bar{P} + \frac{1}{\tau_S})^2}{2} \qquad \text{when } \tau_W \to \infty \tag{4.41}$$

In Figures 4.6 and 4.7, the corresponding response curves are given. The characteristic terahertz modulation frequencies which are expected, due to the picosecond carrier lifetimes in the device, are found. The figures may, at first sight, look misleading as the maximum modulation frequency increases as the lifetimes increase. However, it should be noted that the output power is also affected by the change in the lifetimes, and hence, would also change accordingly, thus resulting in the behaviour of the maximum modulation frequency as illustrated in the figures.

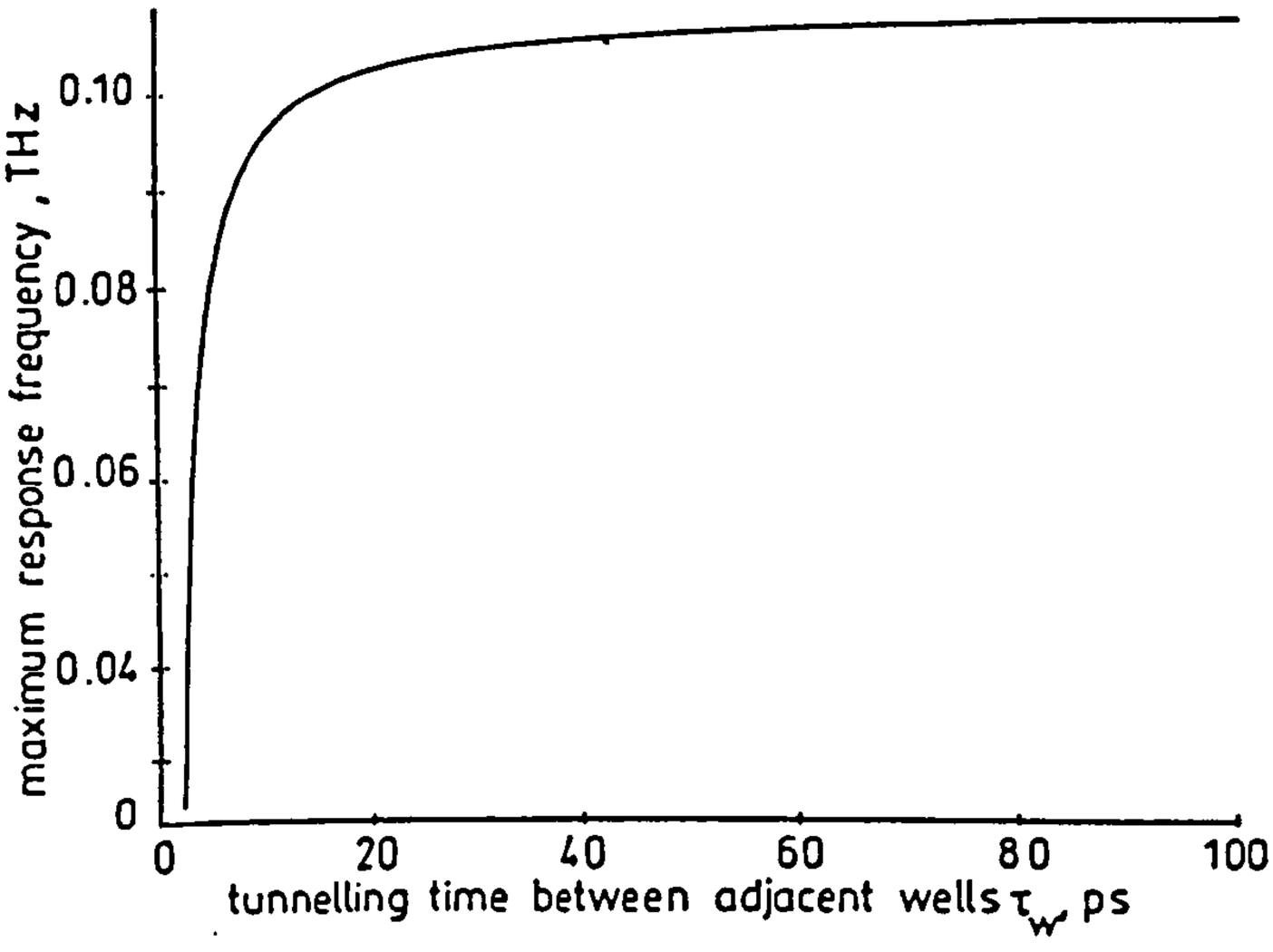

Figure 4.6: Maximum modulation frequency as a function of interwell tunneling time.

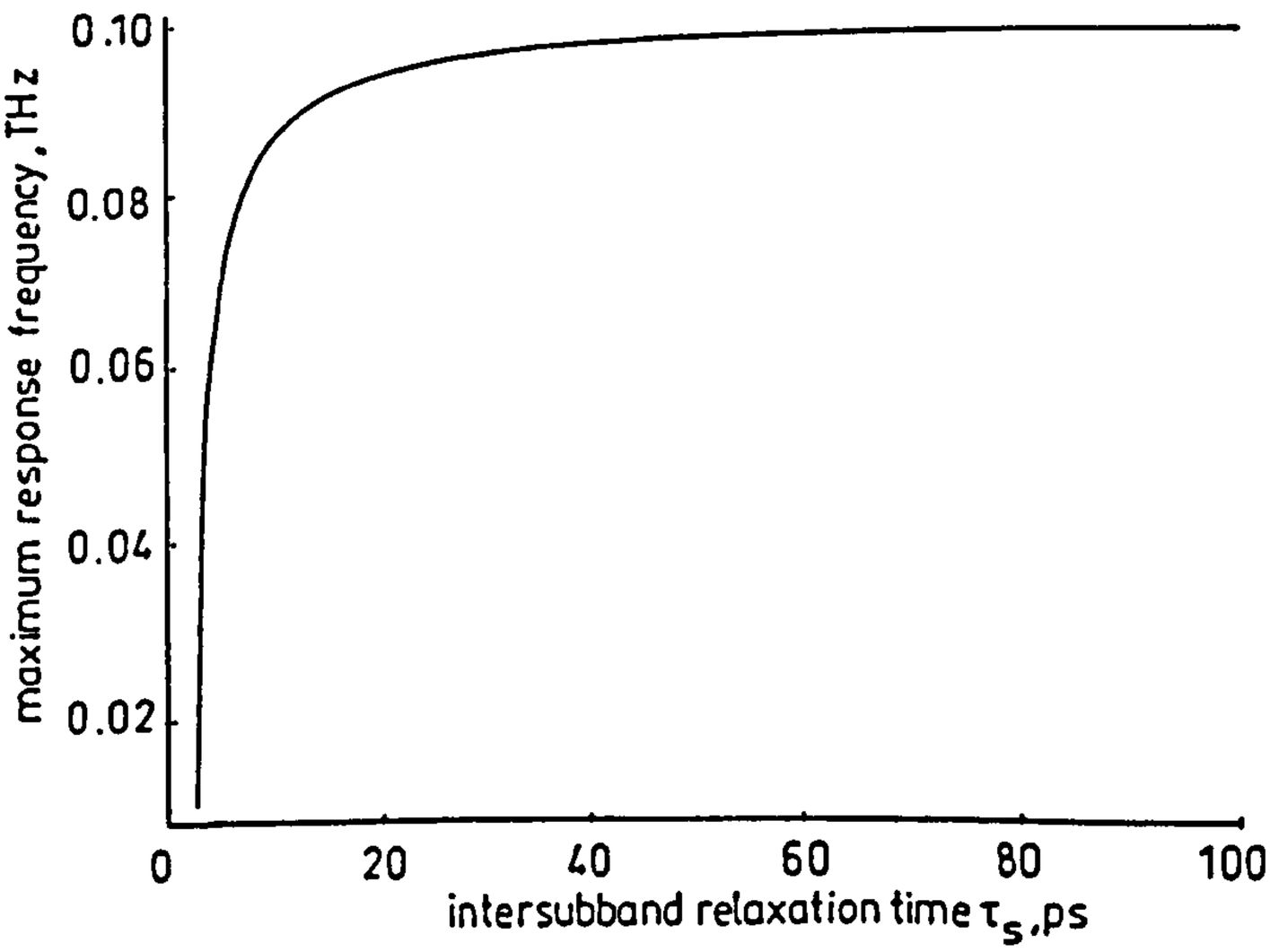

Figure 4.7: Maximum modulation frequency as a function of intersubband relaxation time.

4.7 Conclusion

It has been shown that the modulation bandwidth of intersubband structures is dependent upon carrier lifetimes, and exhibits a unique dependence upon the optical output power of the laser. Here, in contrast with interband semiconductor lasers, there is a fine balance between the contributions of the resonance frequency and damping factor in the determination of the maximum modulation frequency due to the picosecond carrier lifetimes which are characteristic of such structures. In consequence, it is found that the MMF does not increase monotonically as a function of the optical output power of the laser.

Analytical results have been obtained here for a special case of equal lifetimes. It is expected that the same qualitative dependence of the maximum modulation frequency will be found in the more general situation of unequal electron lifetimes. However, analytical results cannot then be easily obtained and numerical methods must be employed instead. This will be discussed in the next chapter.

References

[1] K. A. Shore, P. S. Spencer and C. Y. L. Cheung, "Threshold conditions and modulation properties of intersubband lasers," *Quantum Electronics Symposium IOP CMMP'95*, Liverpool, December 1995.

[2] C. Y. L. Cheung, P. S. Spencer and K. A. Shore, "Modulation bandwidth predictions for unipolar intersubband semiconductor lasers," 10th Conference on Semiconductor and Integrated Optoelectronics (SIOE'96), Cardiff, April 1996.

[3] C. Y. L. Cheung, P. S. Spencer and K. A. Shore, "Modulation bandwidth predictions for intersubband quantum well semiconductor lasers," Optical Society of America, Integrated Photonics Research Conference, Boston, Mass. USA, post-deadline paper PD-1, April 1996.

[4] C. Y. L. Cheung, P. S. Spencer and K. A. Shore, "Optimisation of maximum modulation bandwidth of intersubband semiconductor lasers," Mid-Infrared Optoelectronics: Materials and Devices," Lancaster University, September 1996.

[5] C. Y. L. Cheung, P. S. Spencer and K. A. Shore, "Modulation bandwidth optimisation for unipolar intersubband semiconductor lasers," *IEE Proc. Optoelectron.* **144**, pp. 44-47, 1997.

[6] J. -W. Choe, H. -J. Hwang, A. G. U. Perera, S. G. Matsik and M. H. Francombe, "Resonant tunneling times in superlattice structures," *J. Appl. Phys.* **79**, pp. 7510-7513, 1996.

[7] R. E. Künz and E. Schöll, "Bistability and negative photoconductivity in

optically induced real-space transfer," *Phys. Rev. B* **47**, pp. 4337-4347, 1993.

[8] S. Luryi, "Coherent versus incoherent resonant tunneling and implications for fast devices," *Superlattices and Microstructures* **5**, pp. 375-, 1989.

[9] W. M. Yee, K. A. Shore and E. Schöll, "Carrier transport and intersubband population inversion in coupled quantum wells," *Appl. Phys. Lett.*, **63**, pp. 1089-1091, 1993.

[10] W. M. Yee and K. A. Shore, "Threshold current density calculations for far-infrared semiconductor lasers," *Semicond. Sci. Technol.*, **9**, pp. 1190-1197, 1994.

[11] J. Faist and F. Capasso, "Quantum cascade laser without intersubband population inversion," *Phys. Rev. Lett.*, **76**, pp 411, 1996.

[12] B. E. Cole, C. J. G. M. Langerak, B. N. Murdin, C. D. Bezant, J. M. Chamberlain, C. R. Pidgeon, M. Henini and V. Nakov, "Saturation absorption studies of intersubband relaxation rates in a p-GaAs/AlGaAs QW using a free electron laser," *Physica E* **2**, pp. 181-185, 1998.

[13] J. Faist, F. Capasso, D. L. Sivco, C. Sirtori, A. L. Hutchinson and A. Y. Cho, "Continous wave operation of a vertical transition quantum cascade above $T = 80$K," *Appl. Phys. Lett.* **67**, pp. 3057-3059, 1995.

Chapter 5

Self-Consistent Dynamics of Intersubband Lasers

5.1 Introduction

In the previous chapter, an analytical study of the modulation response of the TQW intersubband laser was undertaken. There were, however, several approximations and assumptions that were made in order to obtain that simple expression for the modulation response given in Equation (4.35). In addition, the lifetimes that were utilised there were taken as parameters of the calculations. In order to verify those results that were obtained from the analytical study, namely the existence of an optimum output power to achieve the maximum modulation frequency, the results of a numerical investigation will be detailed in this chapter. Moreover, in the present analysis, the relevant lifetimes will be deduced from calculations of electonic wavefunctions in the structures.

There are two triple quantum well (TQW) structures which will be considered, one which is suitable for.mid-infrared (MIR) lasing, at a nominal wavelength of 10 μm [1], and the other for near-infrared (NIR) lasing, at a wavelength of 1.55 μm [2]. These structures are illustrated in Figures 5.1 and 5.2.

5.2 Anticrossing

Anticrossing affects the state lifetimes and structure energy levels, and hence, the transition energy. It occurs when a bias voltage of appropriate magnitude is applied to a multi-quantum well (MQW) structure, and two coupled energy levels change position; the lower becomes the upper and *vice versa* as in Figure 5.3.

The structures in Figures 5.1 and 5.2 are designed to have, when unbiased, a transition energy near to that corresponding to the required operating wavelength, so that when account is taken of the effects of the bias voltage and anticrossing, the resulting transition energies would correspond to the required wavelengths. Although anticrossing, between $E_2^{(2)}$ and E_1, and between $E_2^{(1)}$ and E_3, results in decreased transition energies, it is nevertheless necessary in order for successful device operation to be achieved, as it results in the inversion of state lifetimes, a faster carrier escape rate from the structure and increased overlap between the wavefunctions of the subbands [6].

As mentioned in the previous chapter, there is a minimum anticrossing

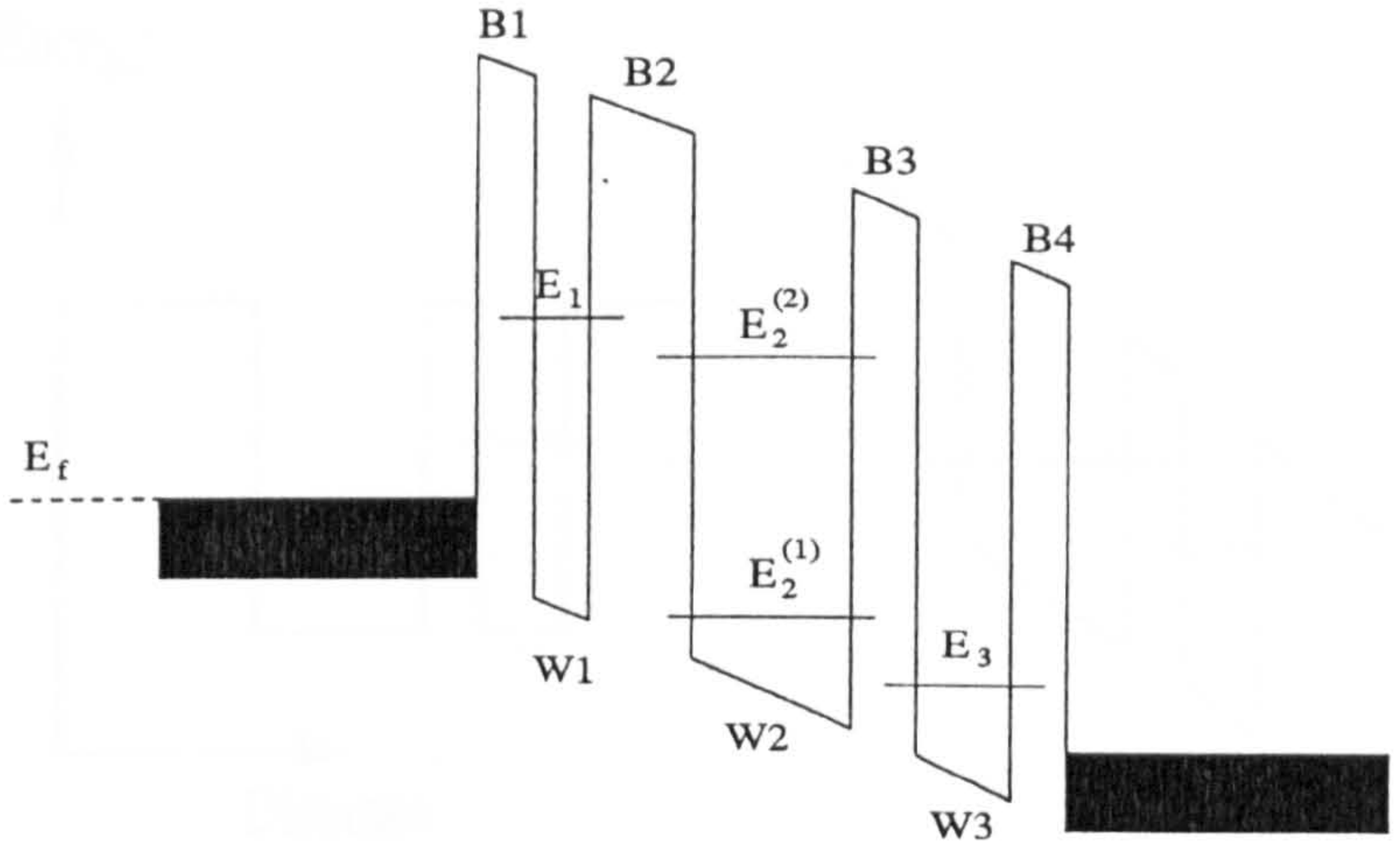

Figure 5.1: Schematic conduction band diagram of the MIR TQW structure biased to an appropriate operating voltage. Structure composition is GaAs/$Al_{0.45}Ga_{0.55}As$. Well widths are 2.8 nm, 8.2 nm, 6.2 nm. Barrier widths are 4.0 nm, 5.0 nm, 3.0 nm, 2.4 nm.

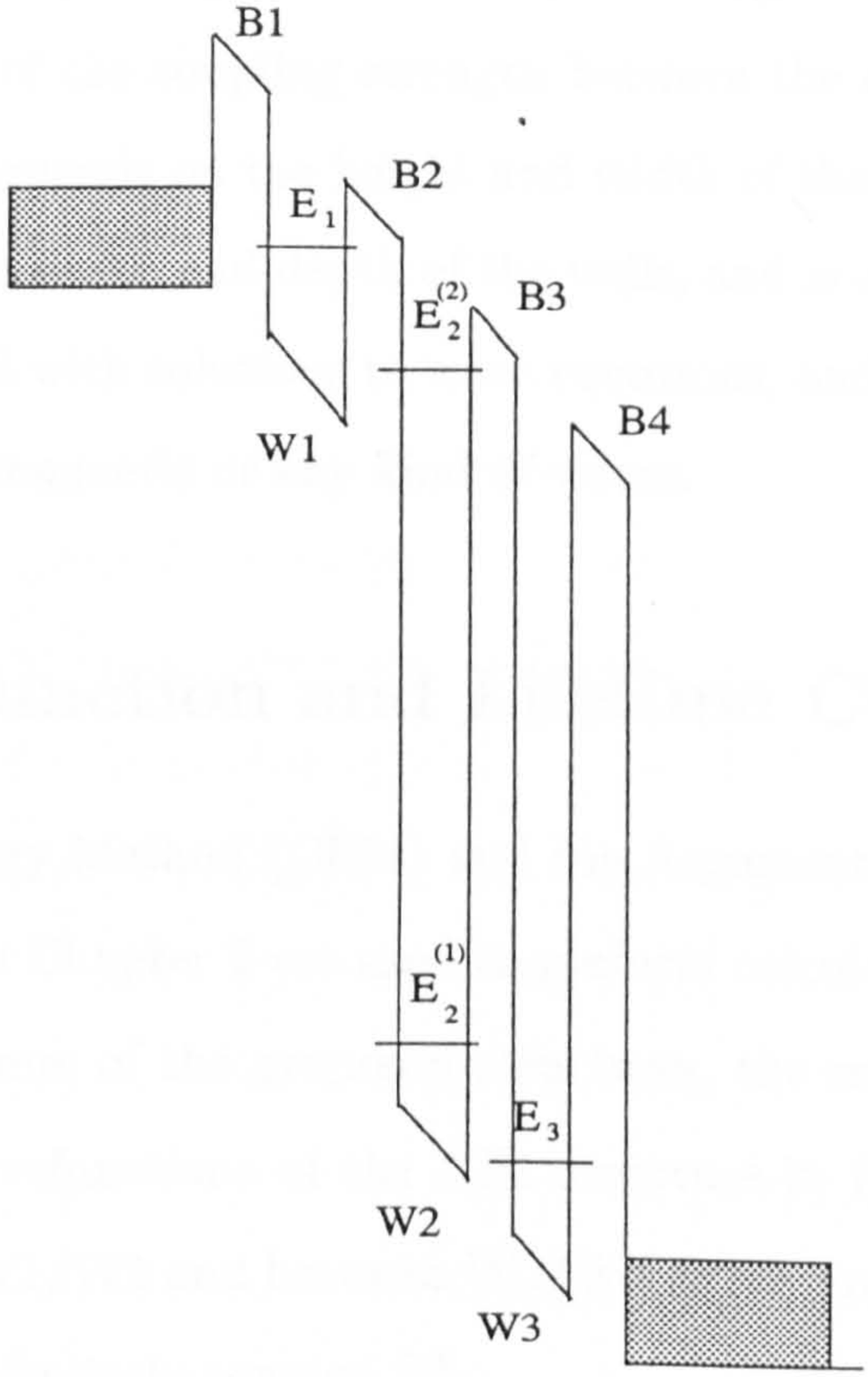

Figure 5.2: Schematic conduction band diagram of the NIR TQW structure biased to an appropriate operating voltage. Barrier composition is AlAs. W1 is $Al_{0.2}Ga_{0.8}As$. W2 and W3 are both $In_{0.53}Ga_{0.47}As$. Well widths are 3.1 nm, 3.1 nm, 2.1 nm. Barrier widths are 2.0 nm, 3.0 nm, 1.6 nm, 1.6 nm.

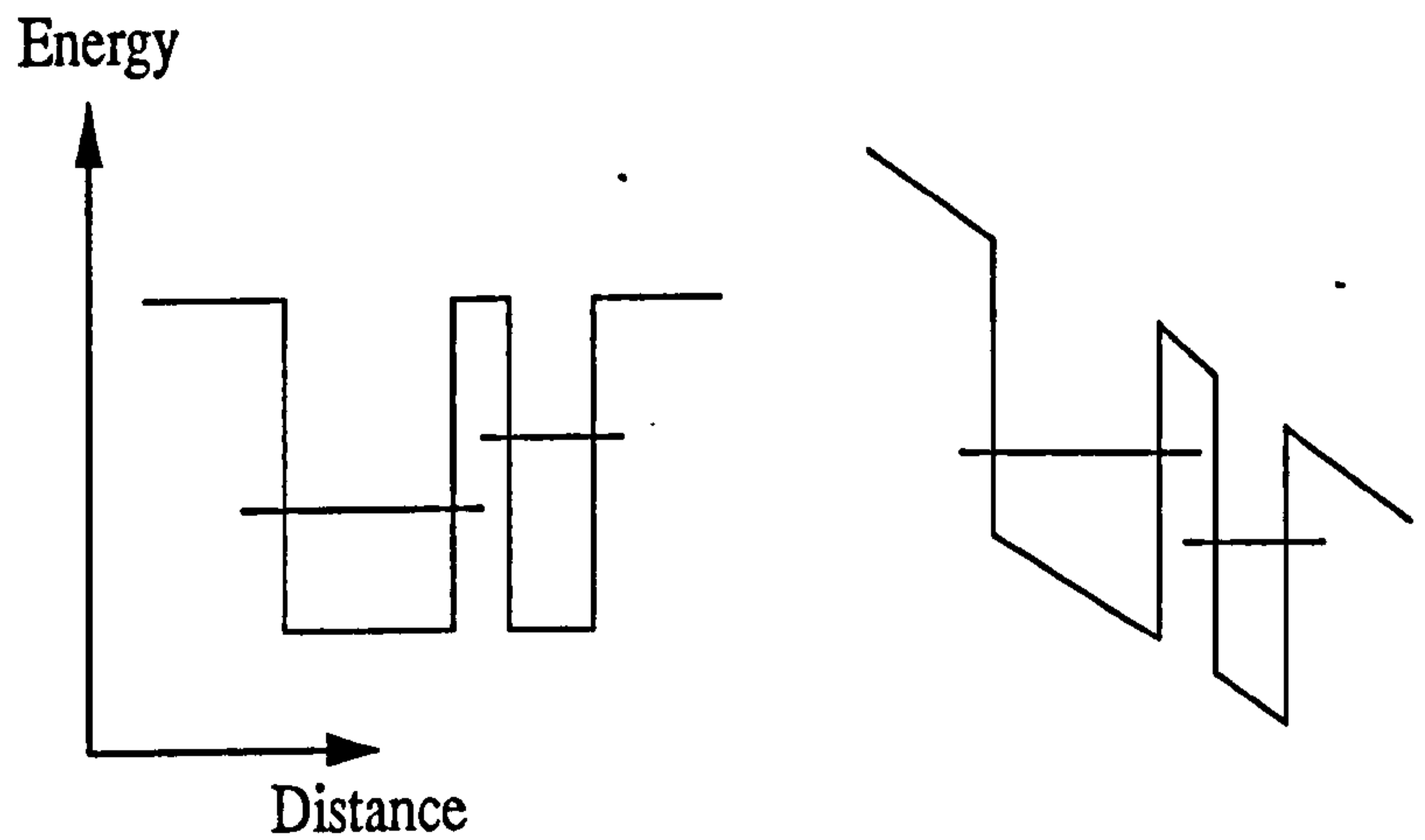

Figure 5.3: Schematic conduction band diagram of a coupled QW structure when unbiased (left) and when biased to an appropriate voltage (right).

gap, or energy level splitting, between coupled energy levels and this minimum is a measure of the coupling strength between the coupled wells. The splitting strongly depends on the height and width of the barrier separating the wells and on the width and depth of the wells, and is a fundamental phenomenon associated with solutions to wave equations, and applies equally to probability, electromagnetic or any kind of waves.

5.3 Wavefunction and Lifetime Calculations

The Complex Energy Method (CEM) and the Argument Principle Method (APM) described in Chapter 2 are used to perform calculations of the wavefunctions and lifetimes of the proposed structures, the results are shown in Table 5.1. The wavefunctions of the NIR structure in Figure 5.4 indicate coupling between W1/W2 and between W2/W3 as required, the wells of the MIR structure are similarly coupled [1].

5.3.1 State Lifetimes

In most cases, the higher the energy level, the shorter the corresponding state lifetime. The state lifetimes of bound states are infinite, while those of quasibound states are usually of the order of the order of picoseconds or femtoseconds. However, in some structures there occurs an inversion of these state lifetimes [4],as is the case for the TQW structures in Figures 5.1 and 5.2.

A study of the variation of the state lifetimes with well and barrier widths, and the state lifetimes' dependence on coupling and anticrossing has been undertaken [5], and the results have been utilised in the design of the TQW structures here.

5.3.2 Tunneling Times

As mentioned previously, the minimum energy splitting or anticrossing gap ΔE, is a measure of the coupling strength between the respective coupled wells. The stronger the coupling, the larger the minimum separation, resulting in faster tunneling time through the barrier. Figure 5.5 illustrates the change in the wavefunction localisations as the coupling between the wells become stronger. When the structure is unbiased, there is no coupling between the wells, and the wavefunctions are localised in their respective wells. However, as the voltage is slowly increased, the energy separation ΔE between the energy levels decreases, and the wavefunctions become more and more delocalised. At a bias voltage of 70 meV, the mininum value of ΔE is

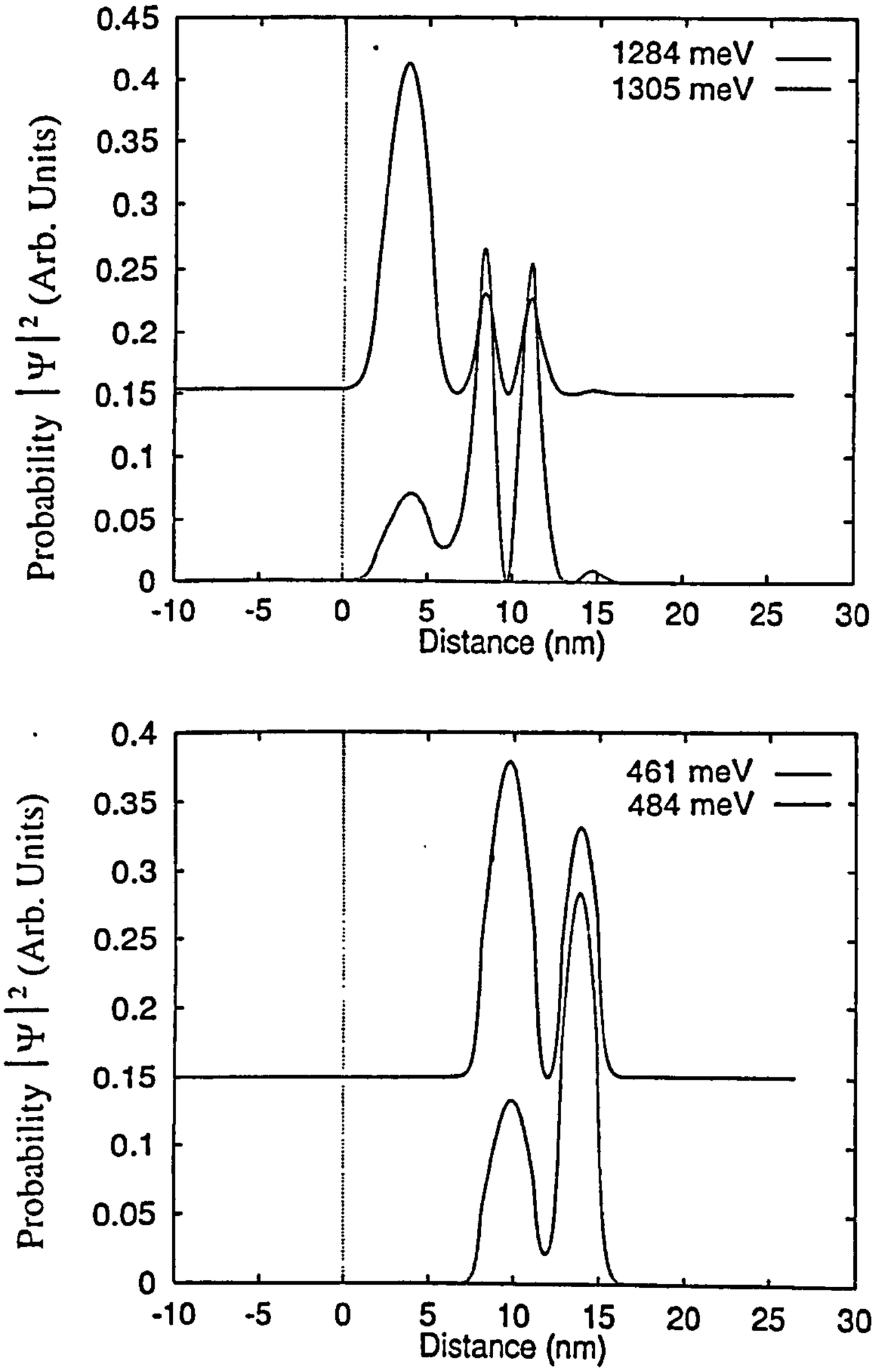

Figure 5.4: The wavefunction of the NIR structure's four energy levels, when biased to a voltage of 550 meV.

Table 5.1: The four energy levels of the structures in Figures 5.1 and 5.2 respectively, with the corresponding state lifetimes.

MIR structure at a bias of 70 meV		
	Energy levels (meV)	State lifetimes (ps)
E_1	211.2	1.26
$E_2^{(2)}$	205.2	3.23
$E_2^{(1)}$	80.6	1.68
E_3	76.3	0.85

NIR structure at a bias of 550 meV		
	Energy levels (meV)	State lifetimes (ps)
E_1	1304.8	0.82
$E_2^{(2)}$	1283.6	1.04
$E_2^{(1)}$	484.8	0.72
E_3	461.2	0.50

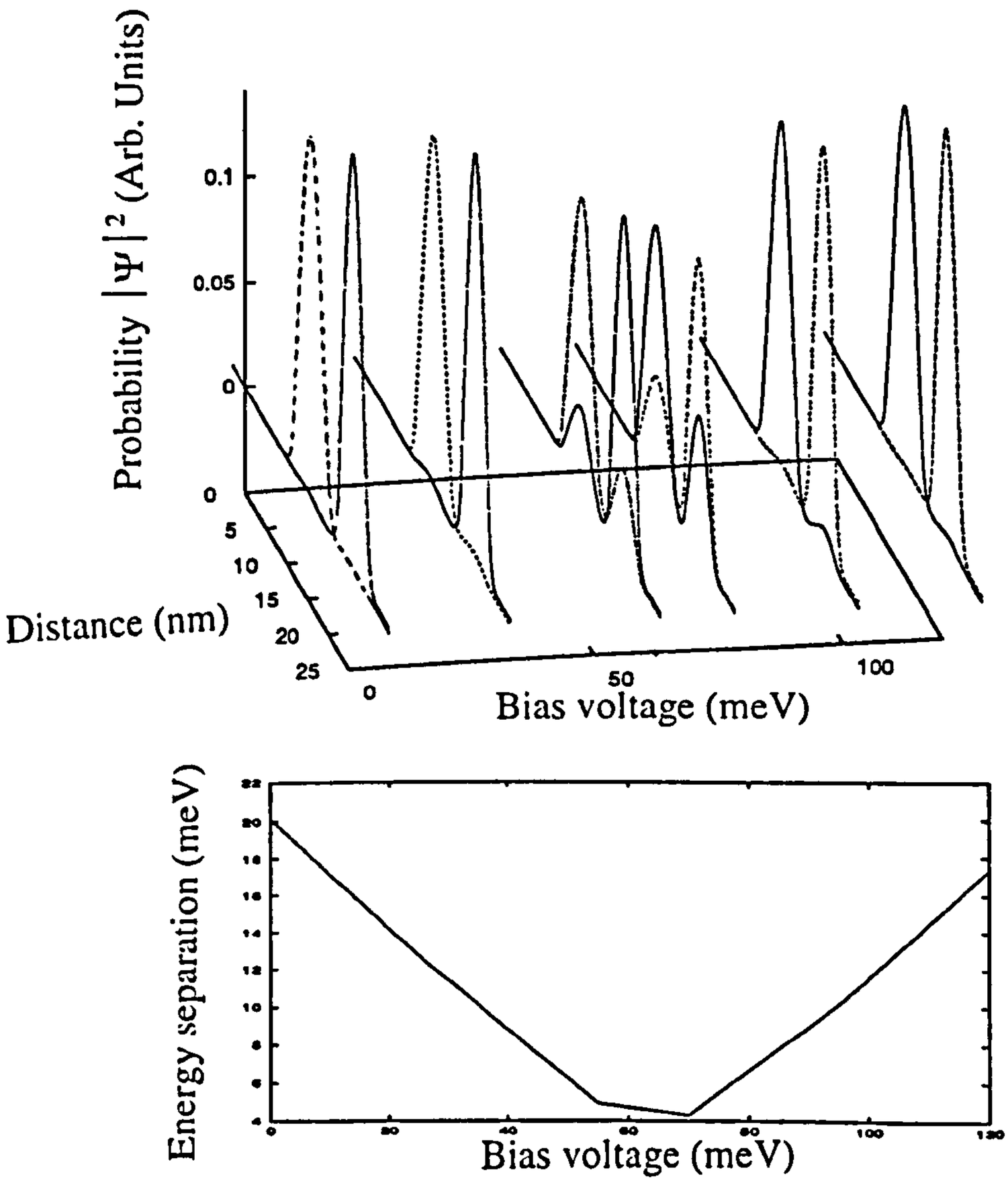

Figure 5.5: The wavefunctions of $E_2^{(1)}$ and E_3 in the MIR structure of Figure 5.1 at different bias voltages, and their respective energy separations.

reached and there is alignment between the energy levels of the wells, and hence maximum tunneling currents are achieved at that voltage. This is also known as the anticrossing gap since if the bias voltage is increased beyond this point, the wavefunctions become localised again, but in the other well.

The tunneling times between the wells are then calculated from the respective energy separations using Equation (5.1), where the tunneling time, $\tau_{tun} = \pi\hbar/\Delta E$. The results are shown in Table 5.2.

Table 5.2: The energy separations between the two pairs of coupled wells of the MIR and NIR structures, and the calculated tunneling times.

MIR structure

Energy levels	ΔE (meV)	Tunneling time (ps)
$E_2^{(2)}$ and E_1	3.96	0.52
$E_2^{(1)}$ and E_3	4.14	0.50

NIR structure

Energy levels	ΔE (meV)	Tunneling time (ps)
$E_2^{(2)}$ and E_1	21.2	0.10
$E_2^{(1)}$ and E_3	23.6	0.09

5.4 Modulation Response and MIR Dynamics

The population dynamics are described by the rate equations of Equations (4.2)-(4.6) described in Chapter 4. In order to accomplish direct current modulation of the laser, it is first pre-biased to a point about threshold where where the linear P-J relationship holds (see Figure 4.3 in Chapter 4). A modulating current $J_m(t)$ is superimposed upon the pre-bias so that the laser is driven by a total current $J_b + J_m(t)$. The optical output power will then respond to the modulating current. Assuming that $J_m(t)$ is sinusoidal such that $J_m(t) = J_m cos(\omega_m t)$, where J_m is the amplitude and ω_m the frequency of the modulating current. The current then varies between $J_b - J_m$ and $J_b + J_m$ with corresponding variations in the photon density (or optical output power) between P_{min} (minimum) and P_{max} (maximum). The empirical definition of the modulation depth can then be given as

$$\eta = \frac{P_{max} - P_{min}}{P_{max}} \tag{5.1}$$

As it not possible to obtain analytical forms for the modulation response for the general case of unequal tunneling times, it is therefore obtained numerically, using Equation (5.1), by solving the rate equations of Equations (4.2)-(4.6) and (4.8) for different values of the modulating frequency ω_m (Figure 5.6).

The existence of an optimum output power may be observed by the behaviour of the modulation response as P is increased, shown in Figure 5.7. In the figure, the modulation response is normalised with respect to the peak

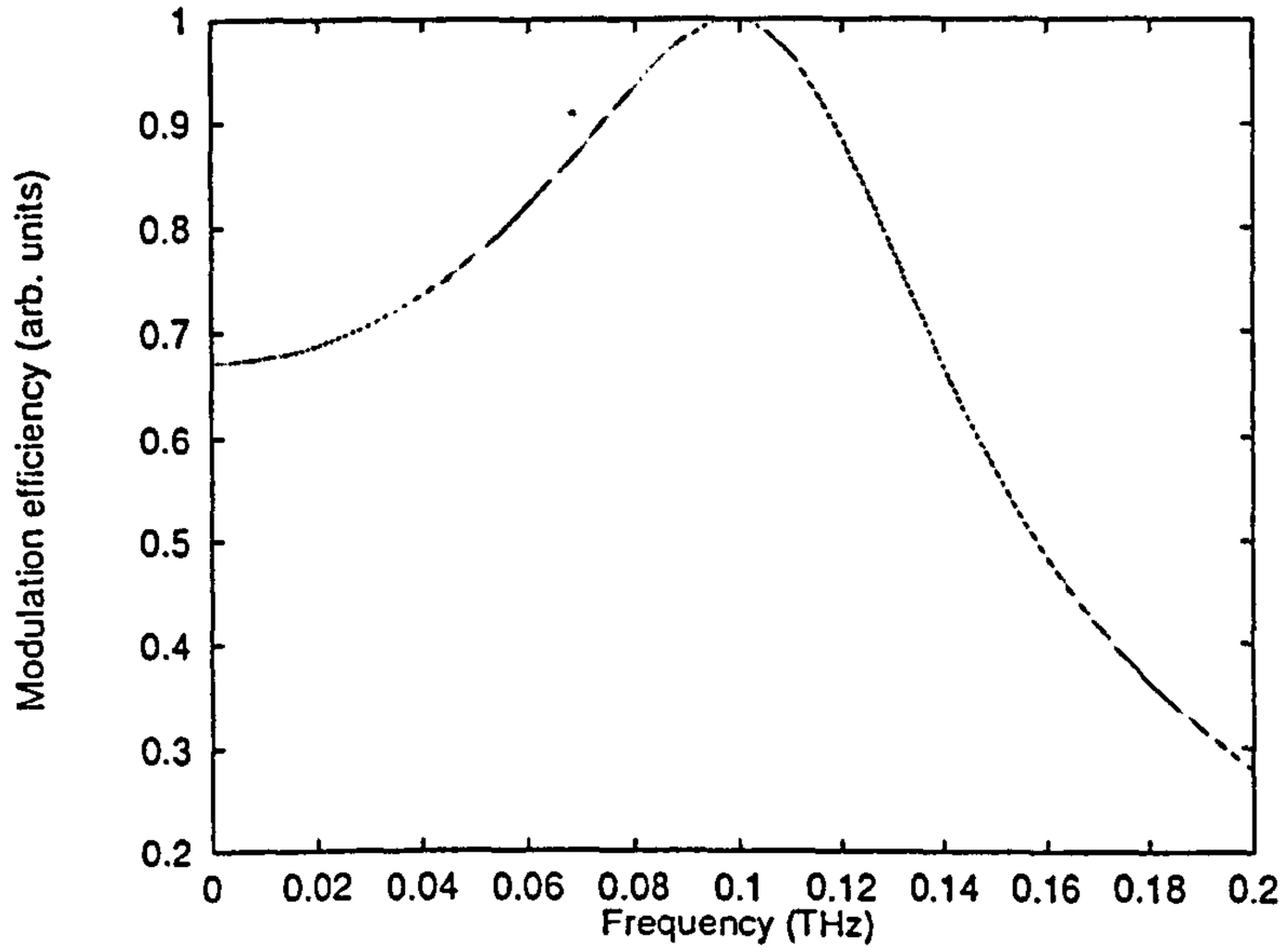

Figure 5.6: Modulation response of the MIR stucture shown in Figure 5.1, with the parameters in Table 5.4.

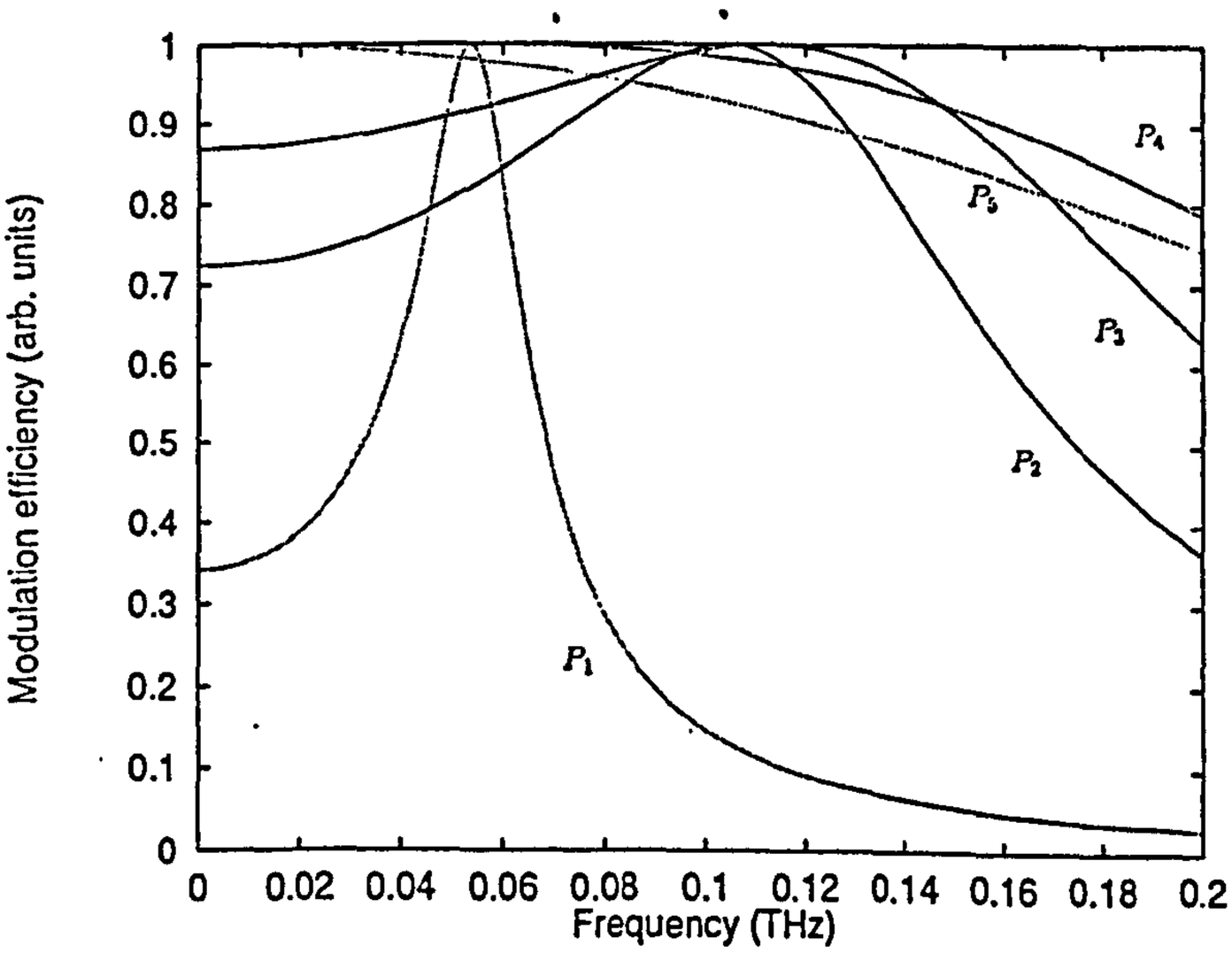

Figure 5.7: The modulation response of the MIR TQW structure with increasing values of photon density P. Optimum output power is at P_3 for $f_3 = 112$ GHz.

Table 5.3: The maximum response frequency f_i corresponding to the photon densities in Figure 5.7.

$P_1 = 0.06 \times 10^{17}$ cm^{-3}	$f_1 = 0.052$ THz
$P_2 = 0.31 \times 10^{17}$ cm^{-3}	$f_2 = 0.093$ THz
$P_3 = 0.50 \times 10^{17}$ cm^{-3}	$f_3 = 0.112$ THz
$P_4 = 0.96 \times 10^{17}$ cm^{-3}	$f_4 = 0.062$ THz
$P_5 = 1.50 \times 10^{17}$ cm^{-3}	$f_5 = 0.005$ THz

Table 5.4: Parameters for the calculation of the modulation response of the MIR and the NIR TQW structures.

MIR parameters

Symbol	Meaning	Value
a	Gain coefficient	10^{-5} s^{-1}
α	$J_m = \alpha J_b$	0.02
τ_T	Carrier transit time through the structure	3.2 ps
τ_S	Intersubband relaxation time	1.2 ps
τ_P	Photon lifetime	1.0 ps

NIR parameters

Symbol	Meaning	Value
a	Gain coefficient	10^{-5} s^{-1}
α	$J_m = \alpha J_b$	0.02
τ_T	Carrier transit time through the structure	3.8 ps
τ_S	Intersubband relaxation time	3.0 ps
τ_P	Photon lifetime	1.0 ps

modulation efficiency, and not its DC value as is usually the case, in order to better illustrate the behaviour of the peak frequency as the output power varies. Hence, the various modulation efficiency plots are not unity at DC. It can be seen that the sharpness of the response decreases with increasing P. The maximum response frequency increases until a certain value of P, after which the familiar shape of the modulation response is lost (Table 5.3).

In the special case treated analytically in Chapter 4, it can be shown that the modulation response is basically limited by the photon lifetime. The present simulations indicate that this remains the case for the more general structures treated here, so improvements should be obtained by using device design parameters which results in decreased photon lifetime.

5.5 NIR Dynamics

As the tunneling times for the NIR structure are faster than that for the MIR structure, it is expected that the maximum modulation response frequency should be higher that in the MIR case. Figure 5.8 illustrates that this is indeed the case. The maximum modulation response frequency for the NIR structure is about 155GHz, while that of the MIR structure has a value of about 100GHz.

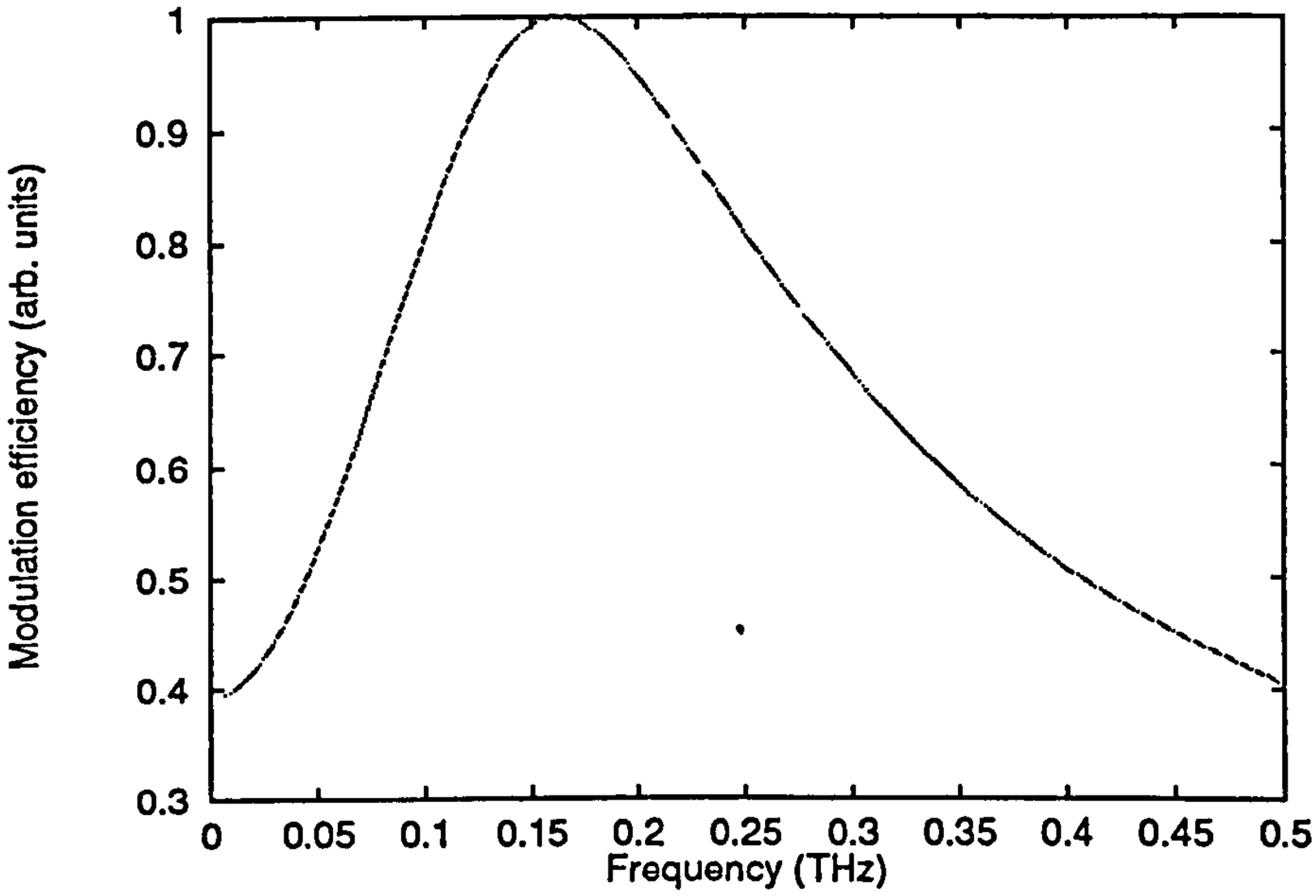

Figure 5.8: Modulation response of the NIR stucture shown in Figure 5.2, normalised with respect to the peak modulation efficiency, found using the parameters in Table 5.4. The MMF is at about 155 GHz at the photon density of 1.20×10^{17} cm^{-3}.

5.6 Conclusion

Two prototype structures suitable for incorporation into intersubband structures, for MIR and NIR lasing respectively, have been designed. The carrier and modulation response behaviour of the structures have been investigated, and results showing the dependence of the modulation bandwidth on the optical output power of the laser have been obtained.

The maximum modulation frequency does not increase monotonically with increasing optical output power. It is possible that a further improvement in modulation bandwidth may be achieved by further optimisation of the TQW structure, but the fact that the carrier lifetimes in intersubband structures are of the same order as, or shorter than, the photon lifetime, indicates that the achievable direct current modulation bandwidth of intersubband lasers is essentially determined by the photon lifetime. Hence, improvements should be obtained by using device design parameters which results in decreased photon lifetime.

References

[1] C. Y. L. Cheung and K. A. Shore, "Self-consistent analysis of the dc modulation response of unipolar semiconductor lasers ," *J. Mod. Optics* **45**, pp. 1219-1229, 1998.

[2] C. Y. L. Cheung, P. Rees and K. A. Shore, "Quantum well structures for THz bandwidth NIR unipolar semiconductor lasers," 6th IEEE International Conference on Terahertz Electronics (THz98), September 1998.

[3] C. Y. L. Cheung and K. A. Shore, "Self-consistent analysis of the dc modulation response of unipolar semiconductor lasers ," 13th Quantum Electronics Conference (QE-13), September 1997.

[4] G. N. Henderson, L. C. West, T. K. Gaylord, C. W. Roberts, E. N. Glytis and M. T. Asom, "Optical transitions to above-barrier quasibound states in asymmetric semiconductor heterostructures," *Appl. Phys. Lett.*, **62**, pp. 1432-1434, 1993.

[5] C. Y. L. Cheung and K. A. Shore, "Anti-crossing and coupling effects in the design of intersubband semiconductor lasers," submitted for publication.

[6] C. Sirtori, J. Faist, F. Capasso, S. L. Sivco, A. L. Hutchinson and A. Y. Cho, "Mid-infrared (8.5 μm) semiconductor lasers operating at room temperature," *IEEE Photonics Technol. Lett.*, **9**, pp. 294-296, 1997.

Chapter 6

Theory of Intersubband Optical Gain

6.1 Introduction

In Chapter 4, four-level intersubband rate equations were introduced, and a simple expression for the gain was used in the calculations. In the present chapter, more consideration will be given to the formalism of intersubband gain, and a comparison drawn with conventional interband semiconductor laser gain. But first, each of the basic components which make up the general optical gain equation will be reviewed, and the forms appropriate for intersubband calculations will be found.

6.2 Density of States

As is well appreciated, in QW structures, discrete levels are formed by the confinement of electrons in the direction of the QW thickness. The density

of states (per unit energy per unit volume) of such confined electrons in the nth subband in the conduction band is given by

$$\rho_n(E) = \frac{1}{2\pi L_z}\frac{2m_e}{\hbar^2}H(E - E_n) \tag{6.1}$$

where $H(E-E_n)$ is the Heaviside unit step function, m_e is the electron Kane effective mass at the bottom of the conduction band, L_z the QW width and E_n the energy of the nth subband of the QW structures.

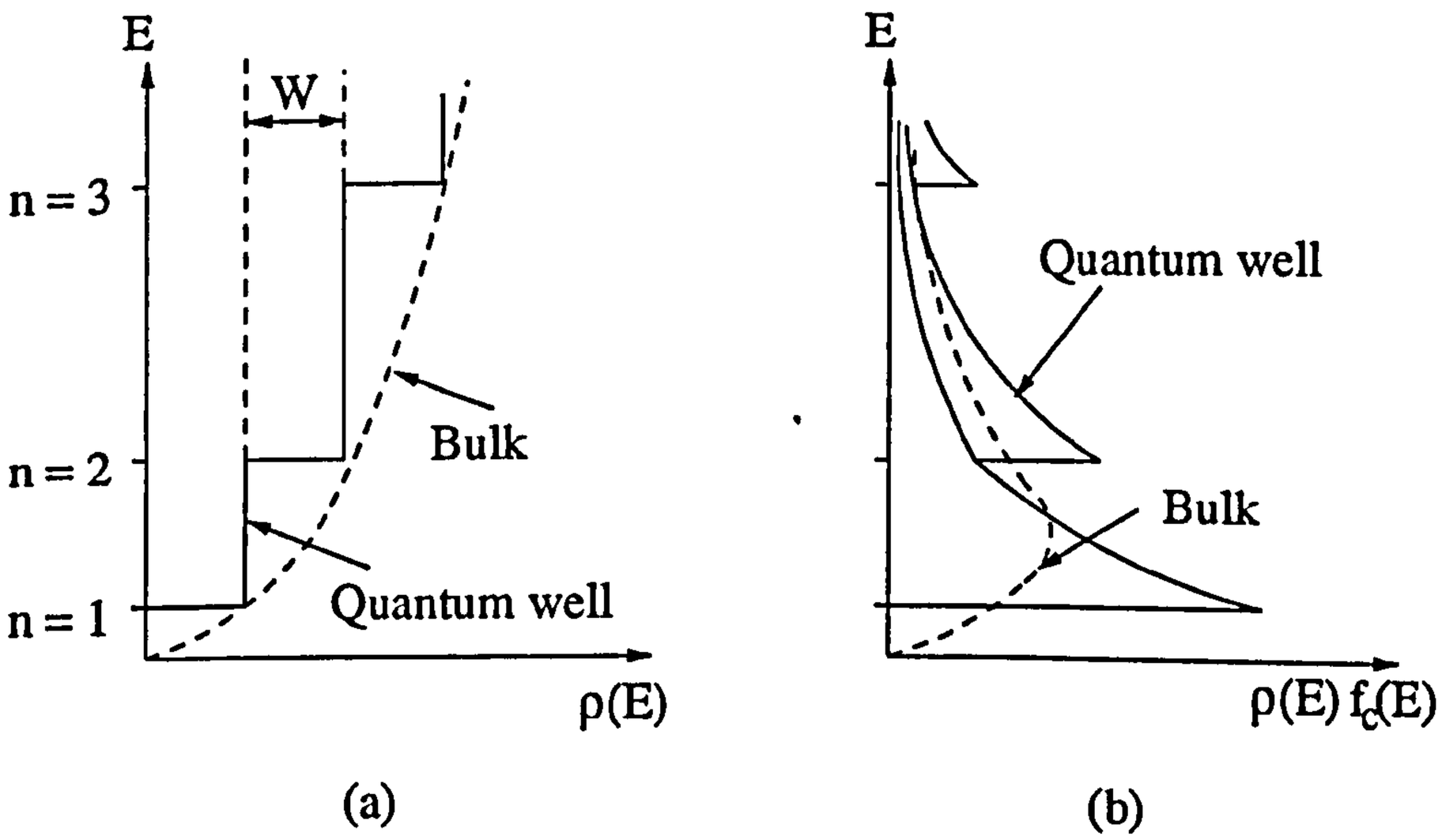

Figure 6.1: (a) Density of states $\rho(E)$, and (b) carrier distribution $\rho(E)f_c(E)$ for bulk and quantum well semiconductors. $W = \frac{1}{2\pi^2}(\frac{2m^*}{\hbar^2})\frac{\pi}{L_z}$.

Figure 6.1 shows the steplike state density for a quantum well and the corresponding narrow carrier distribution. As a point of interest, it is due to this extra degree of confinement that the gain in interband quantum well lasers is larger and sharper than that of ordinary bulk semiconductor lasers. When the barrier height and width are sufficiently large, E_n is equal to

PAGE/PAGES EXCLUDED UNDER INSTRUCTION FROM UNIVERSITY

6.2.1 Reduced Density of States

Applying the k-selection rules, for a given wavevector k, the corresponding upper subband energy ϵ_2 determines the lower subband energy ϵ_1 and vice versa. Therefore, only states with identical k-vectors can form a transition pair, and only vertical transitions in k-space can occur. Because of this restriction, the number of transition pairs is equal to the number of states in either subband, and we can describe the number of allowed transitions using a single density of states function, instead of one for each of the subbands. This single density of states function then is known as the reduced density of states, and takes the same form as the usual density of states for a quantum well

$$\rho_{red}(\epsilon) = \frac{m_r}{\pi\hbar^2 L_z} \tag{6.2}$$

but the effective mass term is now a reduced mass, which can be found from

$$m_r = \frac{m_1 m_2}{m_1 + m_2} \tag{6.3}$$

where m_1 and m_2 are the effective masses at the bottom of the subbands, which are given by [5]

$$m_n = m_e\left(1 + \frac{E_n}{E_G}\right) \tag{6.4}$$

where E_G is semiconductor band gap, and E_n $(n = 1, 2, \ldots)$ is the energy of the subband of interest, with the conduction band bottom as the point of reference.

6.2.2 Fermi-Dirac Distribution Function

When dealing with transitions in semiconductors, the probability that the state from which the transition originates is filled, and the probability that

the terminal state is empty, must always be considered. These so-called occupation probabilities must be .taken into account when performing any calculation related to transitions in semiconductors, whether intersubband, bulk or quantum well.

The occupation probabilities of electrons in each of the subbands in a QW structure can be described using Fermi-Dirac statistics by using a separate Fermi level for the respective subbands (called a quasi-Fermi level), which is determined by the subband effective mass, similiar to the method used for conventional semiconductor lasers. The Fermi functions for the subbands are then

$$f_n = \frac{1}{\exp[(\epsilon_n - E_{Fn})/KT] + 1} \tag{6.5}$$

where ϵ_n are the kinetic energies in the subbands given by $\epsilon_n = \hbar^2 k^2/(2m_n)$, k is the in-plane electron wavevector, K is Boltzman's constant, T the carrier temperature and E_{Fn} are the subband quasi-Fermi levels, given by

$$E_{Fn} = KT\ln(\exp\left(\frac{\pi\hbar^2 N_n}{m_n KT}\right) - 1) \tag{6.6}$$

where N_n is the carrier density in the relevant subband. Note that the above equation is a rearrangement (see Appendix C) of the well-known expression where the total carrier density is found as a product of the Fermi distribution function and the state density

$$N_n = \int f_n(\epsilon_n)\rho_n(\epsilon_n)dE \tag{6.7}$$

where $\rho_n(E)$ is the density of states mentioned in the previous section. The distribution of electrons in each of the subbands then look like that shown in Figure 6.2.

6.3 Intersubband Gain Formalism

Spontaneous and stimulated emission, giving rise to optical gain, are the most basic processes of all lasers. The main factors determining the optical spectrum of an intersubband device are carrier distributions in the subbands, transition matrix elements between the initial and final states, and intraband relaxation of carriers due to various scattering processes. The first of these factors can be calculated by considering the population dynamics in the subbands, which are described by the rate equations treated in Chapter 4. The transition matrix elements determine the strength of the interaction between the two states involved in the transition, and will be discussed further in Chapter 8.

6.3.1 Radiative Transitions

Figure 6.3 shows the subband structure of a quantum well, and the possible electronic transitions, both radiative and nonradiative. From the diagram we can see that

$$\hbar\Omega(\epsilon) = \hbar\Omega_0 + \epsilon_2 - \epsilon_1 \tag{6.8}$$

where $\epsilon_n(k) \equiv E_n(k) - E_n(0)$, $n = 1, 2$. The transition can be designated by $\epsilon \equiv \epsilon_2$, because of the k-selection rules, so that only transitions between those electron state pairs that conserve energy and momentum are induced. This means that the interaction is reduced to a very particular region of the *E-k* diagram.

As mentioned previously, when dealing with transitions in semiconductors, another restriction to be considered is that transitions only occur be-

PAGE/PAGES EXCLUDED UNDER INSTRUCTION FROM UNIVERSITY

tween filled initial states and empty final states. Hence the transition rates can be written as .

$$\begin{aligned} R_{12} &= R_r.f_1(1-f_2) \\ R_{21} &= R_r.f_2(1-f_1) \end{aligned} \tag{6.9}$$

where R_{12} is the stimulated absorptiopn rate, R_{21} is the stimulated emission rate, R_r represents the radiative transition rate that would exist if all state pairs were available to participate in the transition, and f_1 and f_2 are the respective occupation probabilities of the subbands. The net generation rate of photons, or the net stimulated emission rate then is

$$R_{st} = R_{21} - R_{12} = R_r.(f_2 - f_1) \tag{6.10}$$

This net stimulated emission rate, as we shall see in the next section, is directly proportional to the optical gain in the material.

6.3.2 General Expression for Optical Gain

The material gain per unit length can be defined, following [3], as the proportional growth of the photon density as it propagates along some direction in the material. This definition can be related to the transition rates as follows:

$$g = \frac{1}{N_p}\frac{dN_p}{dz} = \frac{1}{v_g N_p}\frac{dN_p}{dt} = \frac{1}{v_g N_p}(R_{21} - R_{12}) = \frac{R_{st}}{v_g N_p} \tag{6.11}$$

where the group velocity, v_g in the second equality is used to tranform the spatial growth rate to the growth rate in time. This chronic growth rate is then linked to the net generation rate of photons, so that finally we have

$$g = \frac{R_r}{v_g N_p}(f_2 - f_1) \tag{6.12}$$

Using Fermi's Golden Rule, R_r, which is the transition rate per unit volume of active material (in units of s^{-1} cm^{-3}) may be written as

$$R_r = \frac{2\pi}{\hbar}|H'_{21}|^2\rho_r(E_{21} = \hbar\Omega_0) \tag{6.13}$$

The details of the derivation of this equation may be found in Appendix C.

Using the above expression we can now write the gain as

$$g_{21} = \frac{2\pi}{\hbar}\frac{|H'_{21}|^2}{v_g N_p}\rho_r(E_{21}).(f_2 - f_1) \tag{6.14}$$

where $|H'_{21}|^2/N_p = \hbar\Omega e^2|z|^2/(2nn_g\epsilon_0)$, and $|z|$ is the dipole moment matrix element. We can now write the gain equation as

$$g_{21} = \frac{e^2\pi|z|^2\Omega}{v_g n n_g \epsilon_0}\rho_r(E_{21}).(f_2 - f_1) \tag{6.15}$$

and since we know the expression for the reduced density of states, $\rho_r(E_{21}) = m_r/(\pi\hbar^2 L_z)$ and that $c = v_g n_g$, the gain equation now becomes [11]

$$g_{21} = \frac{e^2|z|^2 m_r\Omega}{\hbar^2 cn\epsilon_0 L_z}.(f_2 - f_1) \tag{6.16}$$

6.3.3 Lineshape Function

The gain coefficient of a semiconductor laser is, in general, proportional to the population inversion, and the lineshape function of the laser. This lineshape comes about due to the interaction of the electrons with phonons and other electrons, so that the lifetime of a given state is not infinite. It is presently believed that, on average, the electron lifetime in intersubband lasers is about 0.1 ps, and if it is assumed that the state decays exponentially with time, then the energy of each state (and each transition) is no longer sharp but has an energy spread over a range of $\Delta E \approx \hbar/0.1$ ps ≈ 7 meV. This energy

broadening ultimately limits the resolution of features which can be observed in the gain spectrum, and is particularly important to consider in reduced dimensional structures like a quantum well, where the reduced density of states contains very sharp features.

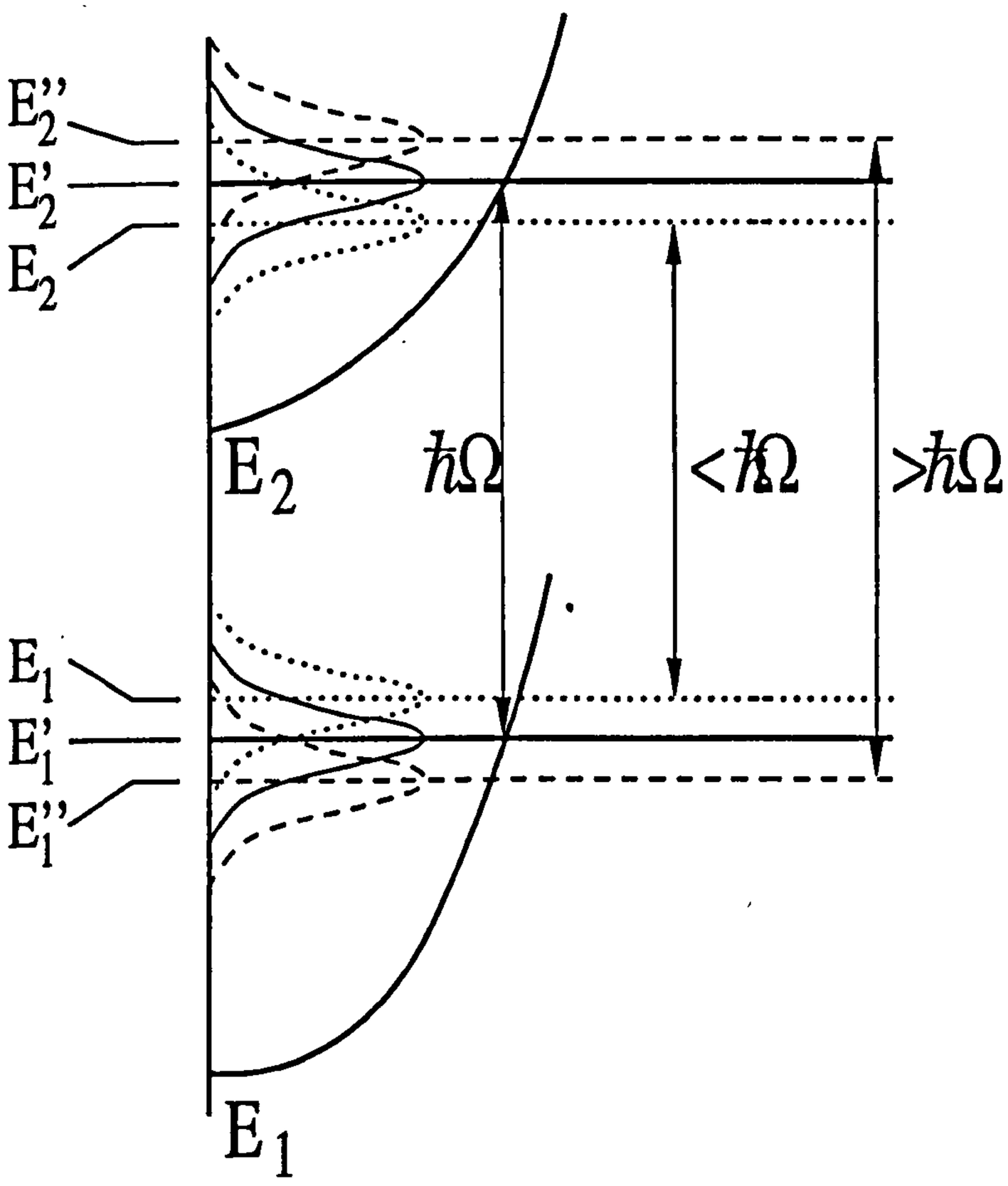

Figure 6.4: Three (of many) transition pairs which contribute to gain at $\hbar\Omega$. The pairs are $E_2'' - E_1''$, $E_2' - E_1'$ and $E_2 - E_1$.

As illustrated in Figure 6.4, when the energy states are broadened, a nominal distribution of the energy states labeled by E_1 and E_2, and many

different transition pairs contribute to gain at a particular transition energy. Hence, there can be spontaneous emission from any parts of the states labeled 2 to those parts labeled 1 at the various frequencies shown in Figure 6.4. The lineshape function therefore describes the probable energy distribution of each transition pair, and in order to determine the total gain at $\hbar\Omega$, the gain coefficient g_{21} must be integrated over all transition energies weighted by the appropriate lineshape function, $\mathcal{L}(\hbar\Omega - E_{21})$. The gain including lineshape broadening takes the form

$$g(\hbar\Omega) = \int g_{21}\mathcal{L}(\hbar\Omega - E_{21})dE_{21} \tag{6.17}$$

The specific form of the lineshape function can be determined by studying the time evolution of an electron state, taking into account its interaction with phonons and other electrons. There are several different lineshapes to select from the various work in the literature [7], [8], [9] but here as mentioned earlier, a simple first-order approximation is used, where the probability of finding an electron in a given state decays exponentially. This simple time dependence when Fourier transformed to the energy domain immediately leads to a Lorentzian lineshape function. The lineshape that will be used here, however, is essentially Lorentzian, but instead of a relaxation time associated with the decay of the electron, an energy dependent scattering term will be used instead, since the scattering rate out of a state is dependent on where the electron is in the state, and on how full the band is [10]:

$$\mathcal{L}(E - E_{21}) = \frac{W(\epsilon)/\pi}{[E - E_{21}]^2 + [W(\epsilon)]^2} \tag{6.18}$$

where the damping term $W(\epsilon)$ covers the optical-phonon assisted scattering events that break the phase coherence of electron states participating in the

radiative transition. A more detailed treatment of these phonon scattering events has been presented by Kisin et al in [10]. A simpler approximation, however, which was utilised by Gelmont et al. in [5] will be applied here, where

$$W(\epsilon) = \frac{\pi e^2}{2\hbar}\left(\frac{1}{\kappa_\infty} - \frac{1}{\kappa_0}\right) q_{ph} \times \begin{cases} N_{ph} \\ (N_{ph}+1)\theta(\epsilon - \hbar\omega_{ph}) \end{cases} \tag{6.19}$$

where the top line corresponds to optical phonon absorption and the bottom line to optical phonon emission, $\hbar\omega_{ph}$ is the polar optic phonon energy seen in Figure 6.3, $\theta(\epsilon)$ is a step function, $q_{ph} = \sqrt{2m_e\omega_{ph}/\hbar}$, κ_0 and κ_∞ are the low and high frequency dielectric constants respectively, and N_{ph} is the phonon Planck function characterised by

$$N_{ph} = \frac{1}{exp(\frac{\hbar\omega_{ph}}{KT}) - 1)} \tag{6.20}$$

The full equation for intersubband gain including lineshape broadening therefore can now be written as

$$g(\hbar\Omega) = \frac{e^2|z|^2 m_r \Omega}{\hbar^2 cn\epsilon_0 L_z} \int_0^\infty d\epsilon \frac{\hbar W(\epsilon).(f_2 - f_1)}{\pi([\hbar\Omega - \hbar\Omega_2 1]^2 + \hbar W(\epsilon)]^2)} \tag{6.21}$$

6.4 General Characteristics of the Gain Spectrum

From the general gain equation of Equation (6.16), it is apparent that there is a maximum value for the gain spectrum, which can be found from Equation (6.16) without the inclusion of the additional term of the difference of the Fermi-distribution functions. It is useful to define at this stage a population inversion parameter $\xi = N_2^{(1)}/N_2^{(2)}$ between the carrier densities in subbands.

Figure 6.5 shows the gain spectra calculated from Equation (6.21), with various values of ξ. It is apparent that the gain can be positive even in the absence of inversion between the two subbands.

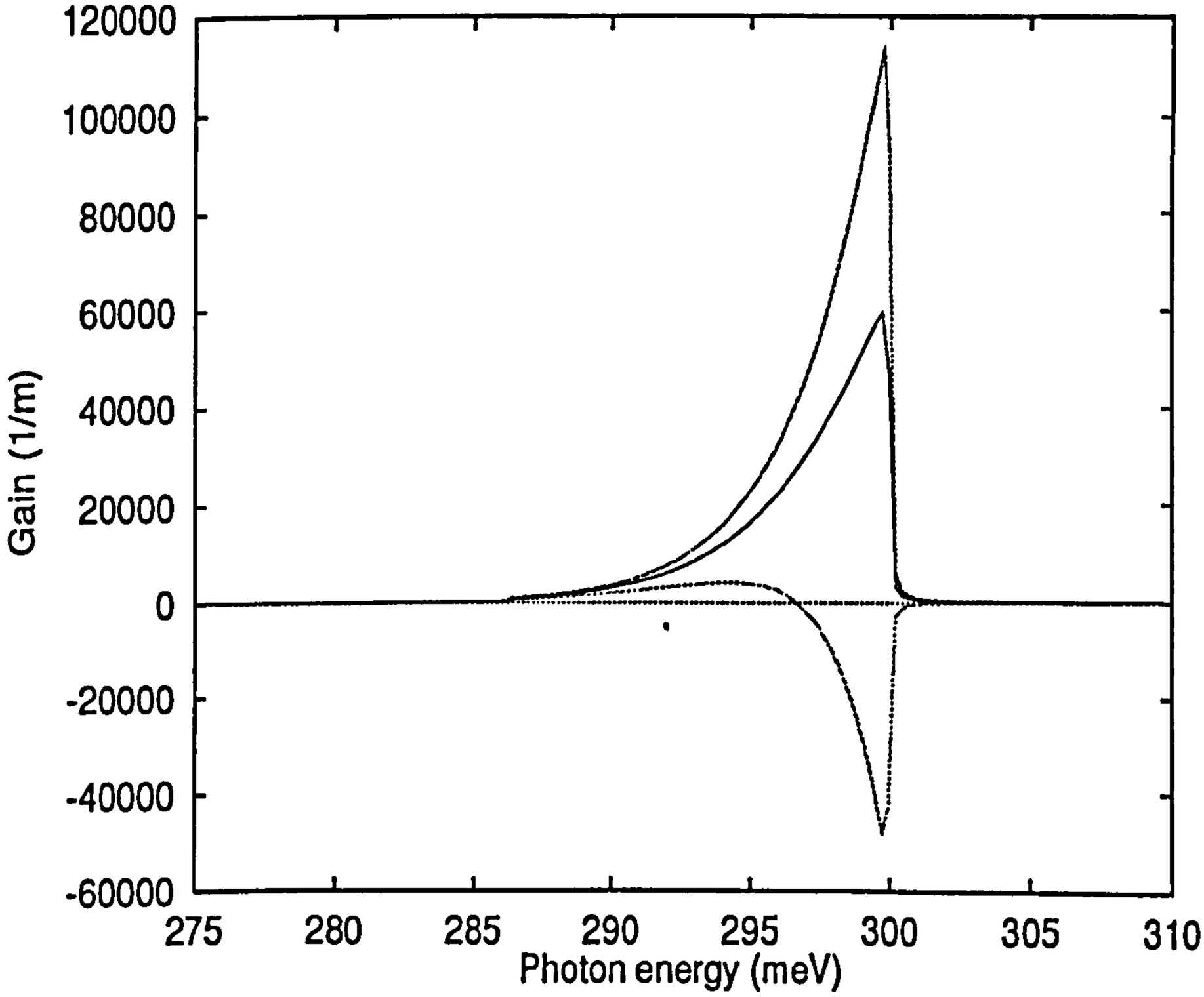

Figure 6.5: Intersubband gain spectra for different values of the population inversion parameter $\xi = N_2^{(1)}/N_2^{(2)}$: (a) $\xi = 0$, (b) $\xi = 1/3$ and (c) $\xi = 1$, i.e. $N_1 = N_2$. Assumed material parameters: $E_G = 1\text{eV}$, $m_e = 0.04m_0$, and $L_z = 7.6$ nm, resulting in $E_1 = 138$ eV, $E_2 = 438$ eV, and $m_1 = 1.28m_e$, $m_2 = 1.88m_e$. Source: [5]

The dominant scattering process is assumed to be intrasubband phonon scattering, which causes a slight bump in the long wavelength portion of

the gain spectra, the rate, $W(\epsilon)$, being proportional to the step function $\theta(\epsilon - \hbar\omega_{ph})$. Hence the scattering process is initiated when the electron energy exceeds the LO phonon energy (of ≈ 40 meV depending on the semiconductor material). This means that transitions corresponding to $\epsilon > \hbar\omega_{ph}$ undergo a steplike increase in the broadening by optical phonon emission. Similiarly the spectra are depressed at $\epsilon < \hbar\omega_{ph}$). This effect is only slightly apparent in Figure 6.5 but is more obvious in the higher temperature spectra of Figure 6.6, and in the calculations of the next chapter. It can also be observed in Figure 6.6 that the peak gain occurs at different wavelengths for different temperatures, and shifts to longer wavelengths at higher values of T.

6.5 Conclusion

This chapter has been concerned with developing an expression to describe the intersubband optical gain, paving the way for investigations into the optical gain spectra of QW structures designed for intersubband lasing. The various components of the general optical gain equation have been discussed, and the corresponding forms appropriate for intersubband calculations found. The resulting expression for intersubband optical gain will now be utilised in the next chapter where the optical gain calculations of QW structures designed for lasing at mid-infrared (MIR) and near-infrared (NIR) will be undertaken.

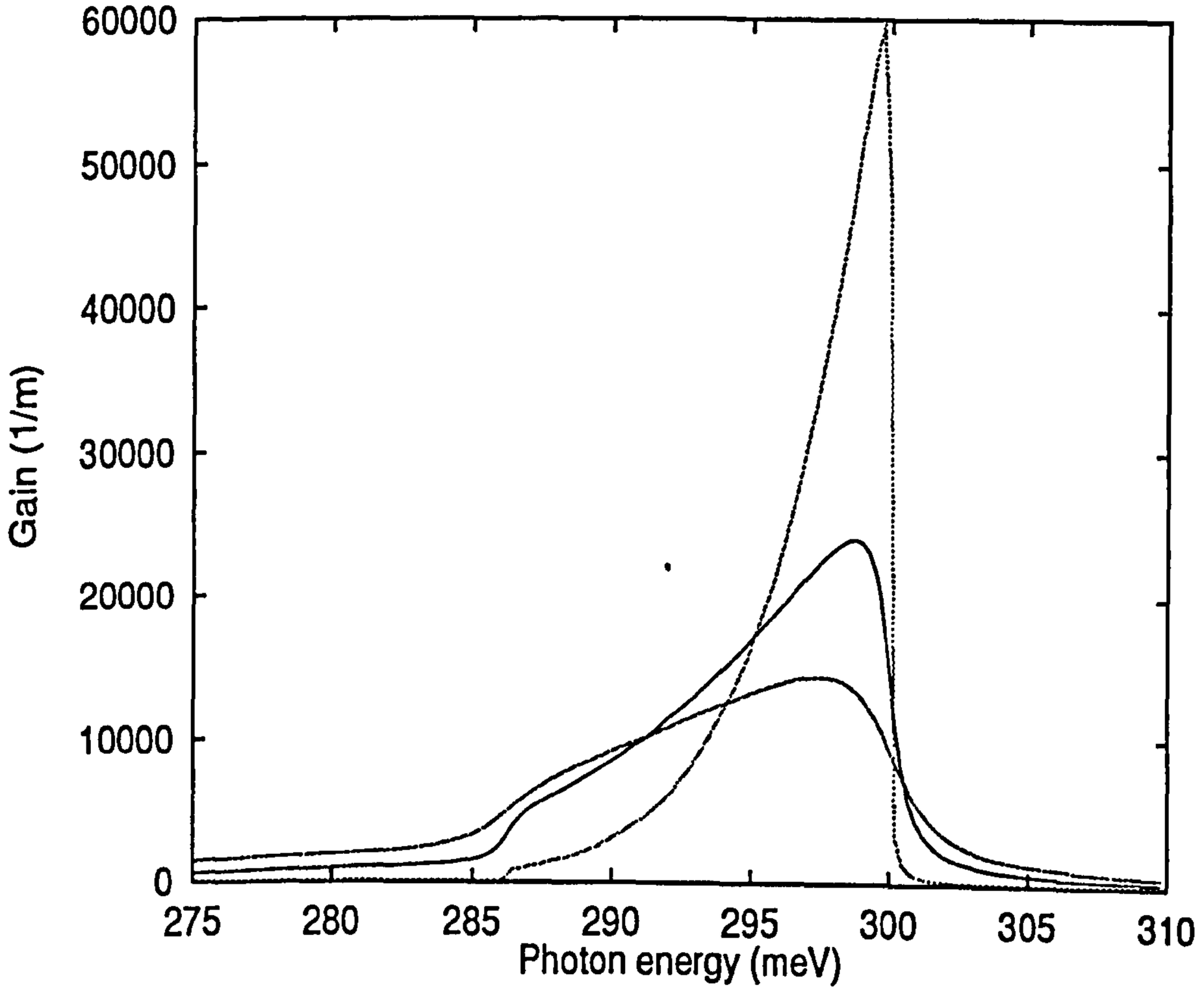

Figure 6.6: Intersubband gain spectra for $\xi = 1/3$ at $T = 100$-300K: (a) $T = 100$K, (b) $T = 200$K, and (c) $T = 300$K.

References

[1] K. Iga, *Fundamentals of Laser Optics*, Chapter 10, Plenum Press, New York, 1994.

[2] Y. Arakawa and A. Yariv, "Theory of Gain, Modulation Response and Spectral Linewidth in AlGaAs Quantum Well Lasers," *IEEE J. Quant. Electron.* **21**, pp. 1666-1674, 1985.

[3] L. A. Coldren and S. W. Corzine, *Diode Lasers and Photonic Integrated Circuits*, Chapter 4 and Appendices 1, 6, John Wiley & Sons, New York, 1995.

[4] J. T. Verdeyen, *Laser Electronics* 3rd ed., Chapter 11, Prentice Hall International Inc., New Jersey, 1981.

[5] B. Gelmont, V. Gorfinkel and S. Luryi," Theory of spectral lineshape and gain in quantum wells with intersubband transitions," *Appl. Phys Lett.* **68**, pp. 2171-2173, 1996.

[6] V. B. Gorfinkel, S. Luryi and B. Gelmont, "Theory of gain spectra for quantum cascade lasers and temperature dependence of their characteristics at low and moderate carrier concentrations," *IEEE J. Quant. Electon.* **32**, pp. 1995-2003, 1996.

[7] S. R. Chinn, P. Zory and A. R. Reisinger, "A model for GRIN-SCH-SQW diode-lasers," *IEEE J. Quant. Electron.* **24**, pp. 2191-2214 , 1988.

[8] M. Asada, "Intraband relaxation effect on optical spectra" in *Quantum Well Lasers*, ed. P. S. Zory, Jr., Chapter 2, Academic Press, SanDiego, 1993.

[9] M. Yamanishi and Y. Lee, "Phase dampings of optical dipole-moments and gain spectra in semiconductor lasers," *IEEE J. Quant. Electron.* **23**, pp. 367-370 , 1987.

[10] M. V. Kisin, V. B. Gorfinkel, M. A. Stroscio, G. Belenky and S. Luryi, "Influence of complex phonon spectra on intersubband optical gain," *J. Appl. Phys.* **82**, pp. 2031-2038, 1997.

[11] C. Y. L. Cheung, P. Rees and K. A. Shore, "Gain calculations for unipolar semiconductor lasers," submitted for publication.

Chapter 7

MIR and NIR Intersubband Optical Gain and Lasing Threshold Current

7.1 Introduction

The previous chapter introduced the formalism of intersubband optical gain, where the various components which make up the expression for the optical gain were discussed. Here, the information gleaned from that chapter as well as Chapters 4 and 5 where the rate equations were discussed, will be utilised to investigate the optical gain spectra of QW structures designed for lasing at mid-infrared (MIR) [1] and near-infrared (NIR) wavelengths [2]. Self-consistent numerical simulations of the carrier conservation rate equations, optical gain and spontaneous emission spectra of the QW structures have also been undertaken [3], and will be described here.

7.2 MIR Intersubband Optical Gain

Use will be made of the MIR TQW structure introduced in Chapter 5, and the same notation which was introduced there for identifying the energy levels and subband carrier populations will be maintained. This section extends the previous analysis to provide a further degree of consistency by incorporating the intersubband gain calculations appropriate for MIR emission. We will restate the rate equations from the previous chapters, and write them in terms of the optical gain $\bar{g}$:

$$\frac{\mathrm{d}N_1}{\mathrm{d}t} = \frac{J}{eL_1} + \frac{L_2}{L_1}\frac{N_2^{(2)}}{\tau_{12}} - \frac{N_1}{\tau_{12}} \tag{7.1}$$

$$\frac{\mathrm{d}N_2^{(2)}}{\mathrm{d}t} = \frac{L_1}{L_2}\frac{N_1}{\tau_{12}} - \frac{N_2^{(2)}}{\tau_{12}} - \bar{g}P - \frac{N_2^{(2)}}{\tau_S} \tag{7.2}$$

$$\frac{\mathrm{d}N_2^{(1)}}{\mathrm{d}t} = \bar{g}P + \frac{N_2^{(2)}}{\tau_S} + \frac{L_3}{L_2}\frac{N_3}{\tau_{23}} - \frac{N_2^{(1)}}{\tau_{23}} \tag{7.3}$$

$$\frac{\mathrm{d}N_3}{\mathrm{d}t} = \frac{L_2}{L_3}\frac{N_2^{(1)}}{\tau_{23}} - \frac{N_3}{\tau_{23}} - \frac{J}{eL_3} \tag{7.4}$$

$$\frac{\mathrm{d}P}{\mathrm{d}t} = \bar{g}P - \frac{P}{\tau_P} \tag{7.5}$$

where e is the electronic charge, and P is the photon density. $\bar{g} = \bar{c}\Gamma g_{peak}$ the peak intersubband gain at the lasing frequency, and $\bar{c} = c/\sqrt{\kappa_\infty}$ is the speed of light in the lasing mode. τ_{12} and τ_{23} are the tunneling times between W1 and W2, and between W2 and W3 respectively, and τ_S is the intersubband relaxation time. In addition, the current injection equation takes the form

$$J = \frac{e}{\tau_T}\left[N_1L_1 + (N_2^{(1)} + N_2^{(2)})L_2 + N_3L_3\right] \tag{7.6}$$

where τ_T is the effective transit time of the carriers through the whole structure, which includes not only the tunneling times through the barriers and the intersubband transition times, but also the time delays caused by intrasubband scattering and electron diffusion, and J is the areal current density.

The expression for the optical gain $g(\hbar\Omega)$ as stated in Equation (6.21) of Chapter 6 is:

$$g(\hbar\Omega) = \frac{4e^2|z_{12}|^2 m_r \Omega}{\hbar L_z c\sqrt{\kappa_\infty}} \int_0^\infty \frac{d\epsilon \hbar W(\epsilon)[f_2(\epsilon) - f_1(\epsilon_1)]}{[\hbar\Omega - \hbar\Omega_\epsilon]^2 + [W(\epsilon)]^2} \tag{7.7}$$

where e is the electron charge, z_{12} is the transition matrix element, κ_∞ the high frequency dielectric constant of the QW, L_z the QW width, Ω_ϵ the optical transition frequency for the in-plane electron momentum $\hbar k = \sqrt{2m_2\epsilon}$, namely $\hbar\Omega_\epsilon \equiv \hbar\Omega_0 + \epsilon_2 - \epsilon_1$, where $\epsilon_2 \equiv \epsilon$ and $\epsilon_1 = \hbar^2 k^2/2m_1$ are kinetic energies in the upper and lower subbands respectively, characterized by the effective masses m_1 and m_2, and the distribution functions f_1 and f_2.

Using the parameters given in Table 7.1 the gain spectra for a single MIR TQW element at various temperatures is obtained, as illustrated in Figure 7.1 below.

Note the slight kink in the gain spectra which occurs due to the threshold nature of $\gamma(\epsilon)$ in the lineshape function. This kink reflects the fact that transitions corresponding to frequencies greater than the optical phonon frequency suffer a steplike increase in the broadening by optical phonon emission. The peak in gain occurs at 10.6μm but, as can be observed, shifts to longer wavelengths with higher temperature. This effect was also mentioned previously

Table 7.1: Parameters used in the intersubband gain spectra simulations.

Descriptions	Values
Upper energy level, $E_2^{(2)}$	203.5 meV
Lower energy level, $E_2^{(1)}$	78.8 meV
Band energy gap for GaAs, E_g	1424 meV
Upper level carrier density, N_2	3.7×10^{17} cm^{-3}
Lower level carrier density, N_1	2.4×10^{17} cm^{-3}
Phonon energy for GaAs, $\hbar\omega_{ph}$	36 meV
Effective mass for GaAs, m_e	$0.067m_0$
Transition matrix element, z_{12}	1.5 nm
High frequency dielectric constant, κ_∞	10.90
Low frequency dielectric constant, κ_0	13.71

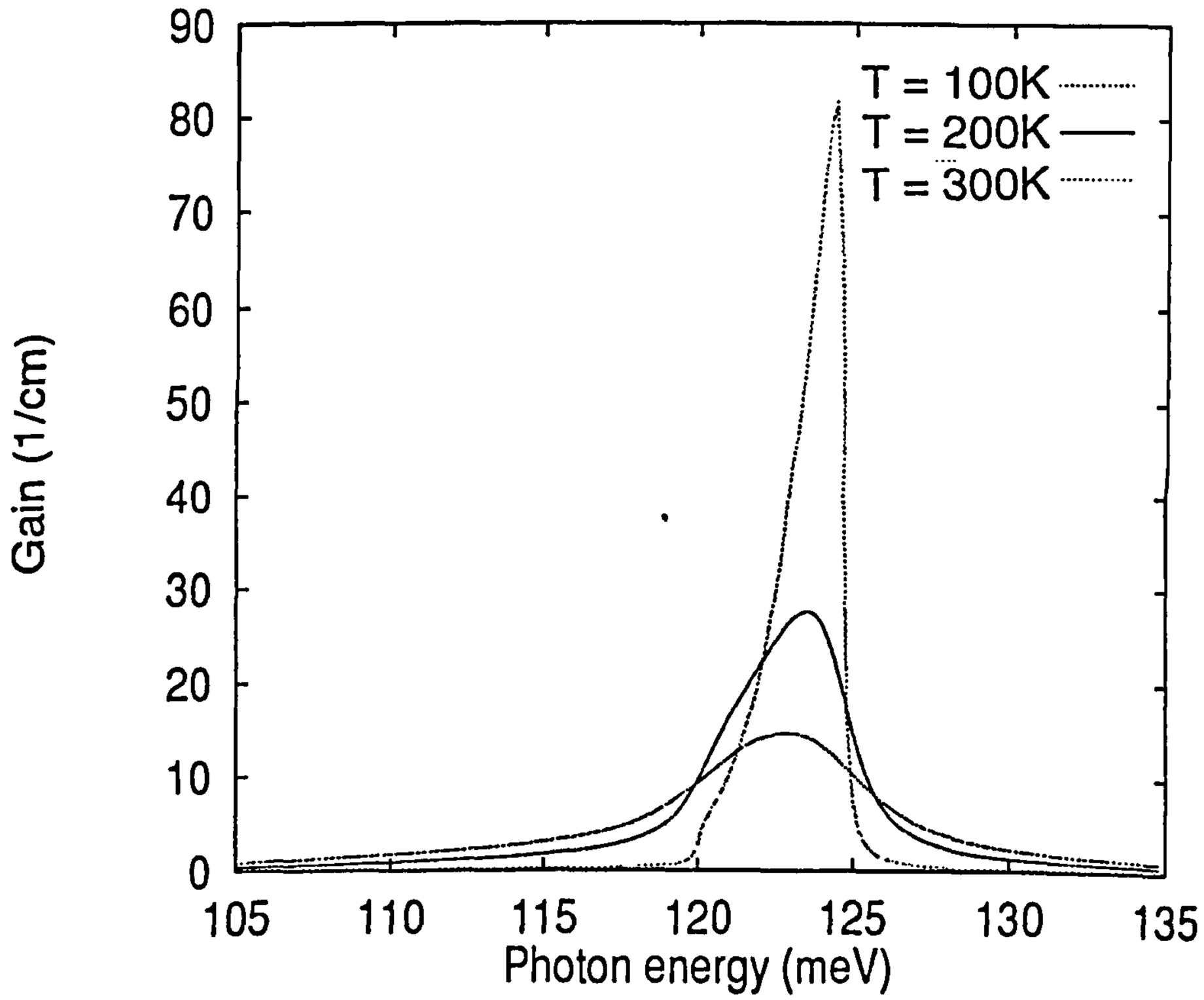

Figure 7.1: Calculated MIR intersubband gain spectra at T = 100-300K.

in [1], [4]. The peak gain at room temperature is very low (20 cm^{-1}) due to the high value of the population inversion parameter $\xi = N_2^{(1)}/N_2(2) = 0.65$. When this is considered together with the relatively larger optical losses at MIR wavelengths, it is clear that there is a need to use several such groups of TQW elements in, for example quantum cascade laser configurations, in order to achieve lasing action. It is, therefore, of interest to perform similiar calculations for near-infrared (NIR) wavelengths where the optical losses are expected to be lower [2].

7.3 NIR Intersubband Optical Gain

In this section, we utilise the NIR TQW structure from Chapter 5. The structure is designed so that at an appropriate bias, its four energy levels are aligned in a manner that causes a transition wavelength of 1.55 μm to be achieved. At this bias voltage, there also exists an inversion of state lifetimes. An intrawell lasing transition scheme is chosen since, in addition to the larger dipole matrix elements achievable, the threshold current for intrawell is lower than that for interwell transitions. It is noted that although maximising the transition matrix element will increase the radiative transitions, but the non-radiative decay rate [6], [7] will also increase. Similiarly, tailoring the matrix element for the purpose of reducing nonradiative transitions will also result in a decrease of radiative transitions.

In contrast to the case of MIR emission, calculations of optical gain at NIR wavelengths, shown in Figure 7.2, are seen to be significantly higher than at MIR wavelengths. Taken together with the lower optical losses ex-

pected in the NIR, this strongly suggests that NIR intersubband lasing can be susteained using very few coupled quantum well structures.

Table 7.2: Parameters used in the intersubband gain spectra simulations.

Descriptions	Values
Upper energy level, $E_2^{(2)}$	1283.6 meV
Lower energy level, $E_2^{(1)}$	484.5 meV
Band energy gap for $In_{0.53}Ga_{0.47}As$, E_g	750 meV
Upper level carrier density, N_2	1.5×10^{18} cm^{-3}
Lower level carrier density, N_1	7.5×10^{17} cm^{-3}
Phonon energy for InGaAs, $\hbar\omega_{ph}$	45 meV
Effective mass for InGaAs, m_e	$0.047m_0$
Transition matrix element, z_{12}	1.65 nm
High frequency dielectric constant, κ_∞	11.62
Low frequency dielectric constant, κ_0	14.66

Using the parameters given in Table 7.2 the gain spectra for a single MIR TQW element at various temperatures is obtained, as illustrated in Figure 7.2 below.

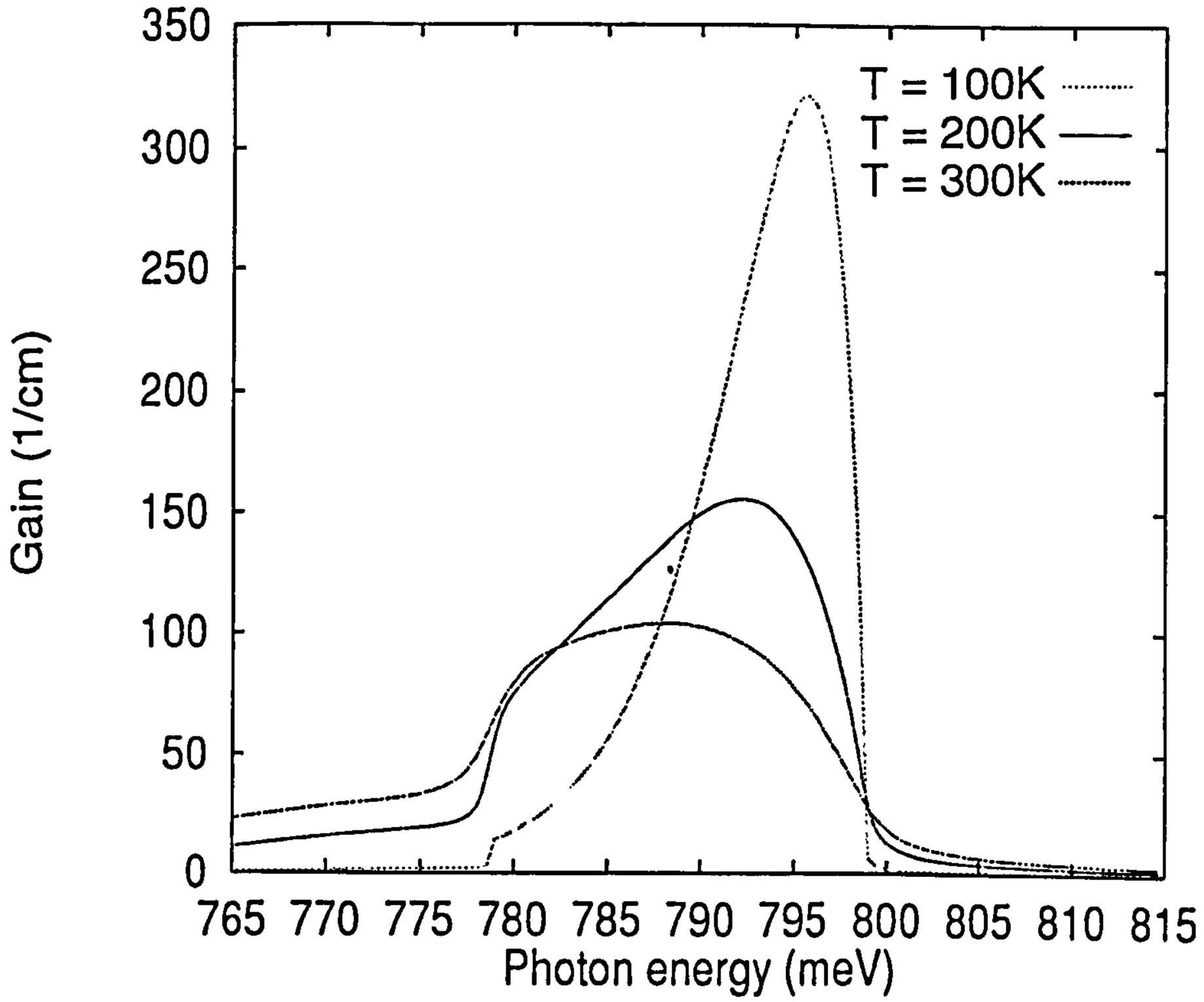

Figure 7.2: Optical gain spectra at NIR wavelengths for a single TQW element at temperatures $T = 100$-300K, $\xi = 0.5$

7.4 Self-Consistent Gain Calculations

In Chapter 4, the optical gain term in the rate equation model was given using the straightforward expression

$$\bar{g} = a(N_2^{(2)} - N_2^{(1)}) \tag{7.8}$$

where an appropriate value for the local gain coefficient, a, was assumed. $N_2^{(1)}$ and $N_2^{(2)}$, of course, are the carrier densities in the lower and upper subbands of the well in which the lasing transition occurs.

7.4.1 Spontaneous Emission and Threshold Current

The single-mode spontaneous emission rate per unit volume, which is the spontaneous emission per optical mode, is given by the Einstein relation which relates the gain spectrum to the spontaneous emission spectrum [9]

$$R'_{sp} = \frac{\Gamma v_g g(\hbar\Omega)}{V} \frac{f_2(1-f_1)}{f_2 - f_1} \tag{7.9}$$

where V is the QW volume, v_g is the material group velocity of the active region and Γ is the overlap factor between the mode and the TQW element such that $V/\Gamma = V_p$, the mode volume. In order to find the total spontaneous emission rate, R_{sp}, we multiply the single-mode rate by the number of optical modes in the QW volume, N_{modes}, such that

$$N_{modes} = \frac{\kappa_\infty n_g \Omega^2}{\pi^2 \hbar c^3} V_p \tag{7.10}$$

where n_g is the group index which comes about from the frequency dependence of the refractive index, such that $n_g = c/v_g$, and V_p is the mode volume

mentioned earlier. It should be noted that the present treatment is only valid for cavity dimensions much larger than the wavelength of interest. A method for finding the equivalent expression for cases where this does not apply, e.g. in microcavities, may be found in [10]. Using the present approach, the following equation for total spontaneous emission rate per unit energy per unit QW volume (in units of s^{-1} m^{-2} eV^{-1}) is obtained

$$R_{sp}(\hbar\Omega) = \frac{ne^2|z|^2 m_r \Omega^3}{\pi^2 \epsilon_0 \hbar^3 c^3} \int_0^\infty d\epsilon \frac{\hbar\gamma(\epsilon).f_2(\epsilon)[1 - f_1(\epsilon_1)]}{\pi[\hbar\Omega - \hbar\Omega_\epsilon]^2 + [\hbar\gamma(\epsilon)]^2} \tag{7.11}$$

The radiative component of the current (excluding stimulated emission) required to obtain a given gain in the QW, can then be found by integrating the spontaneous emission rate over all photon energies:

$$J_{rad} = \frac{eL_2}{\eta_i \eta_r} \int R_{sp}(\hbar\Omega) d(\hbar\Omega) \tag{7.12}$$

where η_i is the internal efficiency [7] of the laser (say 75 %), η_r is the radiative efficiency (usually of order 10^{-4} - 10^{-3} in MIR quantum cascade structures [6], [7], [10]) and J_{rad} is the areal spontaneous current density (A/m^2). The high nonradiative current (40%) [7], in QCLs results in a very high threshold current density (4-15 kA/cm^2 for MIR QCLs).

7.4.2 Modifications to the Rate Equations

An additional term, the spontaneous emission term, will now be added to the photon density rate equation, so that it takes the form:

$$\frac{dP}{dt} = \bar{g}P - \frac{P}{\tau_P} + \beta_{sp}\frac{N_2^{(2)}}{\tau_S} \tag{7.13}$$

where β_{sp} is the spontaneous emission factor, which is the ratio of the single-mode spontaneous emission rate to the total spontaneous emission [9], and

may be obtained from the expression below

$$\beta_{sp} = \frac{\Gamma v_g g_{peak}}{V \int R_{sp}(\hbar\Omega) d(\hbar\Omega)} \frac{f_2(1-f_1)}{f_2 - f_1} \tag{7.14}$$

Also, by equating the the two equivalent expressions for $\bar{g}$ from the rate equations

$$\bar{g} = \frac{c\Gamma g_{peak}}{\sqrt{\kappa_\infty}} \equiv a(N_2^{(2)} - N_2^{(1)}) \tag{7.15}$$

we can obtain an expression for the local gain coefficient, a, such that

$$a = \frac{\bar{c} g_p}{N_2^{(2)} - N_2^{(1)}} \tag{7.16}$$

Using the above expressions, the gain and rate equations can be solved alternatively until the variables converge to constant values. From this calculation, the self-consistent gain spectra are obtained.

7.5 Results

Using the parameters given in Table 7.3, we obtain, for the relevant structures, the MIR and NIR gain spectra. These are shown in Figure 7.3. Tunneling times were calculated from the respective energy level splittings, ΔE_{ij} of the coupled wells using $\tau_{ij} = \pi\hbar/\Delta E_{ij}$. In performing these calculations we have assumed for simplicity that the bias applied to the TQW structures remains fixed throughout, although in reality the bias may change as the current is varied.

It can be observed that the values of the MIR threshold currents in Table 7.4 are comparable to those found by Sirtori *et al* in their experiments [11], [12]. The peak modal gain for 25 such elements in e.g. a QCL is found by

Table 7.3: Parameters used in the calculations for the NIR and MIR devices.

	NIR	MIR
Photon lifetime, τ_P	1 ps	1 ps
Tunneling time, τ_{12}	0.11 ps	0.54 ps
Tunneling time, τ_{23}	0.10 ps	0.45 ps
Transit time, τ_T	3.2 ps	3.8 ps
Well W1 width	3.10 nm	2.80 nm
Well W2 width	3.10 nm	8.20 nm
Well W3 width	2.06 nm	6.20 nm
QW volume, V	1.3mm×2.0μm×3.10nm	1.3mm×2.0μm×8.20nm

multiplying the peak gain at threshold by the mode confinement factor of [12], and is found to be approximately 28 cm^{-1}, which agrees with the value of 30 cm^{-1} in [12]. The good agreement found where the experimental results are available gives added confidence in the model and hence its predictions for the NIR case.

Table 7.4: Threshold current values for a single TQW element.

NIR		MIR	
100K	300K	100K	300K
33.4 A/cm^2	143.5 A/cm^2	576.5 A/cm^2	4071.2 A/cm^2

Attention is drawn to the fact that the peak of the gain curves do not shift with increase in applied current. In conventional lasers, such a shift is

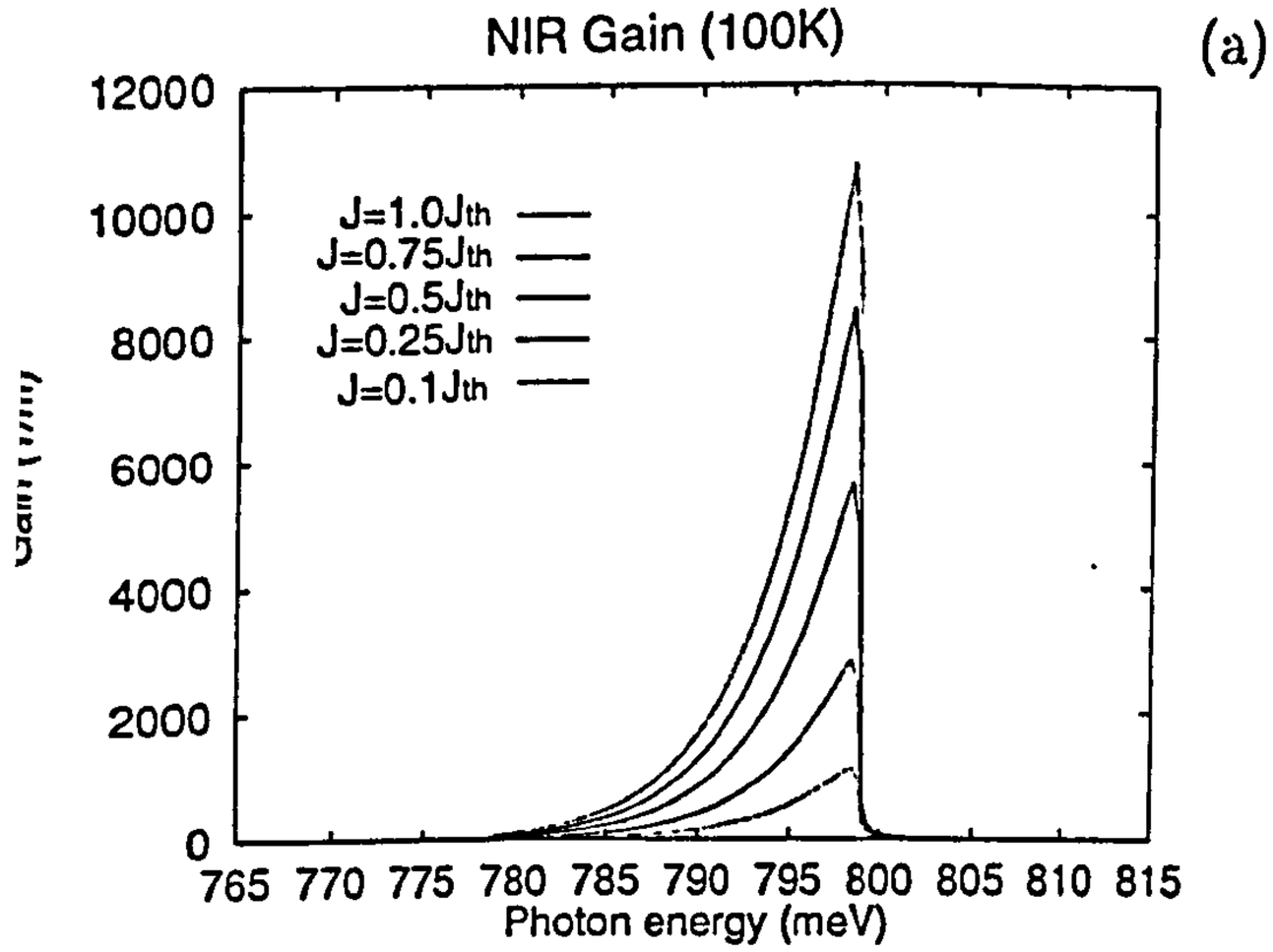

Figure 7.3: Gain spectra of the NIR and MIR structures at various threshold currents.

due to the change in the Fermi-Dirac distributions caused by the increased current, which is made possible by the quasi-continuous nature of the conduction and valence bands in these lasers. In the present case, this shift is not observed in intersubband transitions which involve electrons occupying discrete subbands.

7.6 Conclusion

Using the rate equations for four-level TQWs from previous work, we have performed a self-consistent analysis of the achievable gain of a device utilising this TQW structure, and compared the results with an equivalent TQW structure for MIR lasing. As the results of the MIR calculations are similiar to those of experimental results reported in the literature, it is to be expected that the NIR results are also reliable.

The optical gain spectra was obtained from a modified standard expression for the optical gain per unit length, using the lineshape function as proposed by Gorfinkel *et al* in [5], [4]. Comparisons between the results for the NIR structure and a MIR structure show that for the threshold current densities for the NIR at comparable values of peak gain are two orders of magnitudes smaller that that of the MIR structure. The recent publication by Kisin *et al* [13] indicates that several other considerations may also need to be taken into account in forming the lineshape function for the optical gain expression, including optical phonon confinement effects and electron-phonon scattering rates. In addition, the effect of the state lifetimes, which

were designed to be inverted in the TQW structure, have not as yet been included in the rate equation model. Recent results [14] have shown that these lifetimes should be taken into consideration when designing intersubband devices. This is reserved for further work, and will be discussed in Chapter 9.

References

[1] C. Y. L. Cheung, P. Rees and K. A. Shore, "Gain calculations for unipolar semiconductor lasers," submitted for publication.

[2] C. Y. L. Cheung, P. Rees and K. A. Shore, "Optical gain calculations for NIR intersubband semiconductor lasers," CLEO (Europe) Glasgow, September 1998.

[3] C. Y. L. Cheung, P. Rees and K. A. Shore, "Estimation of threshold current for unipolar intersubband semiconductor lasers," Semiconductor Quantum Wires and Dots, DERA, Malvern, June 1998.

[4] B. Gelmont, V. Gorfinkel and S. Luryi, "Theory of spectral lineshape and gain in quantum wells with intersubband transitions," *Appl. Phys Lett.* **68**, pp. 2171-2173, 1996.

[5] V. B. Gorfinkel, S. Luryi and B. Gelmont, "Theory of gain spectra for quantum cascade lasers and temperature dependence of their characteristics at low and moderate carrier concentrations," *IEEE J. Quant. Electon.* **32**, pp. 1995-2003, 1996.

[6] J. Faist, F. Capasso *et al*, "Measurement of the intersubband scattering rate in semiconductor quantum-wells by excited state differential absorption-spectroscopy," *Appl. Phys. Lett.* **63**, pp. 1354-1356, 1993.

[7] R. Q. Yang, "Infrared laser based on intersubband transitions in quantum wells," *Superlattices and Microstructures* **17**, pp. 77-83, 1995.

[8] C. Y. L. Cheung, P. Rees and K. A. Shore, "Self-consistent optical gain and threshold current calculations for 1.55μm intersubband semiconductor lasers, submitted for publication.

[9] L. A. Coldren and S. W. Corzine, *Diode Lasers and Photonic Integrated Circuits*, Chapter 4, John Wiley & Sons, New York, 1995.

[10] J. H. Smet, C. G. Fonstad and Q. Hu, "Intrawell and interwell intersubband transitions in multiple quantum wells for far-infrared sources," *J. Appl. Phys.* **79**, pp. 9305-9320, 1996.

[11] C. Sirtori, J. Faist, F. Capasso, S. L. Sivco, A. L. Hutchinson and A. Y. Cho, "Mid-infrared (8.5 μm) semiconductor lasers operating at room temperature," *IEEE Photonics Technol. Lett.*, **9**, pp. 294-296, 1997.

[12] C Sirtori, J Faist, F Capasso, D L Sivco, A L Hutchinson and A Y Cho, 'Pulsed and continous-wave operation of long wavelength infrared ($\lambda = 9.3\mu$m) quantum cascade lasers,' *IEEE J. Quant. Electron.* **33**, pp. 89-93, 1997.

[13] M. V. Kisin, V. B. Gorfinkel, M. A. Stroscio, G. Belenky, and S. Luryi, 'Influence of complex phonon spectra on intersubband optical gain,' *J. Appl. Phys.* **82**, pp. 2031-2038, 1997.

[14] C. Y. L. Cheung and K. A. Shore, 'Anticrossing and coupling effects in the design of intersubband semiconductor lasers,' submitted for publication.

Chapter 8

Intersubband Nonlinearities

8.1 Introduction

The linear and nonlinear susceptibilities characterize the optical properties of a medium. If $\chi^{(n)}$ is known for a given medium, then at least in principle, the nth order nonlinear optical effects in the medium can be predicted from Maxwell's equations. All optical phenomena would be predictable and easily understood if the constitutive equation could just be written and the solution found for the resulting set of Maxwell's equations with the appropriate boundary conditions. This, however, is seldom possible.

Physically, $\chi^{(n)}$ is related to the microscopic structure of the medium. The proper evaluation the nth order nonlinear susceptibility necessitates a full quantum mechanical treatment, which shall be considered in a later section. A simpler model will first be considered in order to illustrate the origin of optical nonlinearity and some characteristic features of $\chi^{(n)}$.

8.1.1 Electron Oscillator Model

The electron oscillator model predicts that a polarisation, $\mathbb{P}$, is induced in a dielectric medium under the influence of an applied field, by the resulting creation of dipole moments from the displaced bound charges. The polarisation is the sum of the internal dipole moments induced per unit volume, and adds to the electric flux density such that the total flux density becomes

$$\mathbf{D} = \epsilon_0 \mathbf{E} + \mathbb{P} \tag{8.1}$$

This response of the medium to the electric field under steady-state conditions is determined by the susceptibility of the medium through which the wave is travelling, χ, and is defined by

$$\mathbb{P} = \epsilon_0 \chi(\omega) \mathbf{E} \tag{8.2}$$

where the frequency dependence, or dispersion, of χ emphasises the dispersive nature of the medium response. Dispersive effects are greatest at certain frequencies resonant with atomic transitions. When the frequency ω of the applied field is tuned close to that of a transition, the atoms acquire large dipole moments that oscillate at ω.

χ contains the essential optical properties of the material. It describes the various light-matter interactions and so its complexity determines to what extent these phenomena are taken into account. The refractive index n of the medium, for example, can be written as $n^2(\omega) = 1 + \chi(\omega)$. In general, χ tends to be complex and frequency dependent.

8.2 Nonlinear Susceptibilities

Quantum mechanics provides an expression for the nonlinear susceptibility of a material in terms of the transition dipole moments and transition frequencies. There are two approaches to the calculation of the nth order nonlinear susceptibility, $\chi^{(n)}$. These are (i) the perturbative approach, which is a straightforward iterative third-order solution of the Liouville equation for the density matrix, and (ii) the diagrammatic approach, in which double-sided Feynman diagrams enable the solution to be written directly by following simple rules. As the two approaches have been evaluated and found to be equivalent [1], we shall be using the latter derivation.

8.2.1 Feynman Diagrams

The nonlinear susceptibilities may be calculated using double-sided Feynman diagrams (Figure 8.1) [1], [2]. These diagrams enable one to write directly all permutations of the interacting fields of a system, without calculating lower-order processes. The density matrix is given by $\rho = |\psi\rangle\langle\psi|$, and for the the general use, one needs to keep track of the proper time development of the $\langle bra|$ and $|ket\rangle$ vectors separately. Thus, one plots two parallel lines, with time advancing upwards.

A photon absorbed is symbolised by a wavy line pointing upward (when tracing it from left to right), and a photon emitted is drawn by a wavy line pointing downward (when tracing it from left to right). These symbols for emission and absorpsion apply both on the *bra* and *ket* sides.

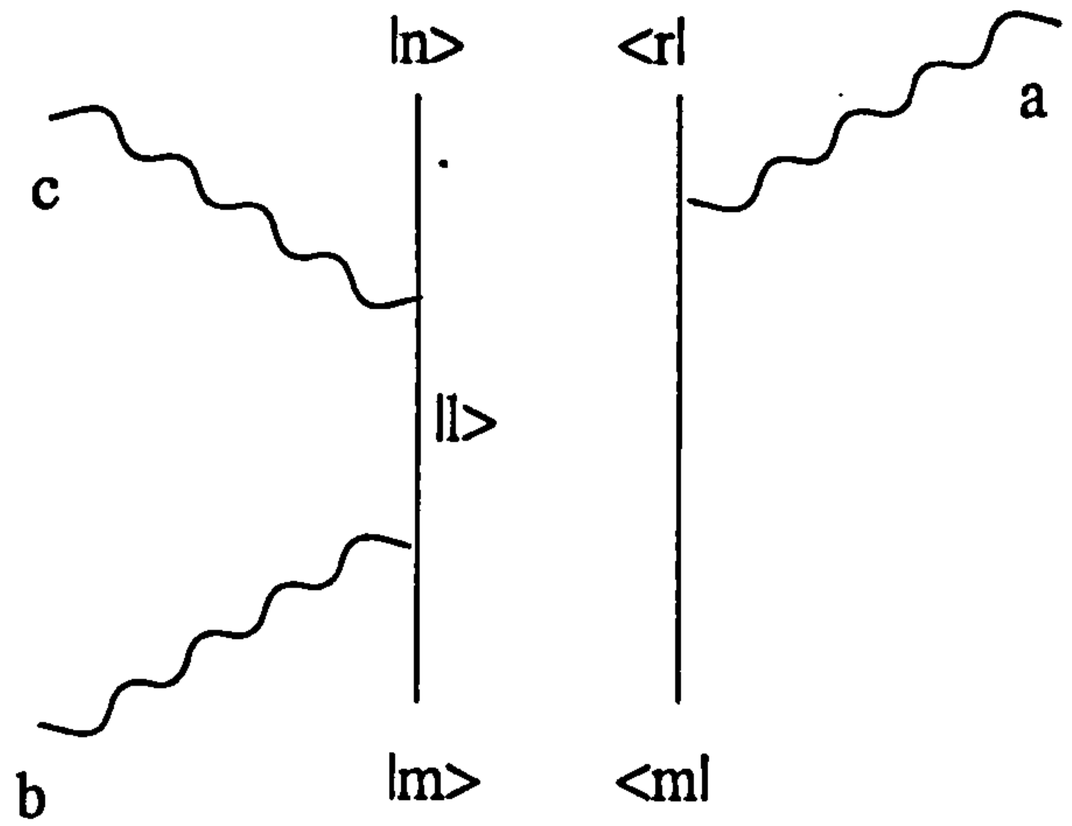

Figure 8.1: Double-sided Feynman diagram.

The prescription on how to translate one such diagram into a term in the expression for the susceptibility is given below following [1]. The rules are specific for these diagrams and refer to the diagram in Figure 8.1 which is the diagram for a third-order nonlinearity. A term includes the following factors:

- Initial density matrix element ρ^0_{mm}.

- Four matrix elements, obtained as follows. Trace the left line (*ket*) upward and then the right one (*bra*) downward, writing a matrix element for each interaction. Note that the transition from $|n\rangle$ to $\langle r|$ involves an "interaction." The polarization order is that of the fields involved where ω_p is the field involved with the transition at the top of the diagram. Thus for Fig. 1 the following is obtained

$$R^{\beta}_{ml} R^{\gamma}_{ln} R^{\mu}_{nr} R^{\alpha}_{rm}$$

where α, β, γ, μ is the Cartesian coordinate of the polarization of the

field ω_a, ω_b, ω_c, ω_p respectively.

- Product of the propagators, obtained as follows. Advance in time until after one has crossed an interaction vertex. The propagator is given by the inverse of the energy difference of the states on both sides of the diagram including damping, minus all photon frequencies of the photons pointing upward (absorbed) plus all photon frequencies of the photons pointing downward (emitted). In Fig. 1 the first propagator is

$$\frac{1}{\omega_{lm} - i\Gamma_{lm} - \omega_b}.$$

The next propagator is

$$\frac{1}{\omega_{nm} - i\Gamma_{nm} - (\omega_b - \omega_c)}.$$

The last propagator is

$$\frac{(-1)}{\omega_{nr} - i\Gamma_{nr} - (\omega_a + \omega_b - \omega_c)}$$

where a (-1) is included for cases where the last interaction occurred on the right-hand (*bra*) side.

8.3 Intersubband Dipole Moment Matrix Elements

The transition matrix element determines the strength of interaction between two states. This interaction can be strong, weak or nonexistent, depending on the wavefunctions describing the two electron states. In Chapter 2, it was

seen that the electron wavefunction can be decomposed into two separate functions - the envelope wavefunction, $\psi(\mathbf{r})$, and the Bloch function, $u(\mathbf{r})$.

In general, for a given interaction Hamiltonian $H(\mathbf{r}) = H'.\mathbf{r}$, the transition dipole approximation matrix element, so called because the influence of the photon wavevector in the matrix element is neglected [5], or dipole matrix element, between two states is given by

$$H'.\langle\phi_f|\mathbf{r}|\phi_i\rangle = H'.\langle\psi_f.u_f|\mathbf{r}|\psi_i.u_i\rangle \tag{8.3}$$

where $\phi_i = \psi_i.u_i$ and $\phi_f = \psi_f.u_f$ are the electron wavefunctions of the initial and final states respectively.

As the envelope wavefunctions ψ_i and ψ_f are slowly varying compared to the Bloch functions $u_i(r)$ and $u_f(r)$, this matrix element can be approximately written as

$$\langle\psi_f.u_f|\mathbf{r}|\psi_i.u_i\rangle \approx \langle u_f|\mathbf{r}|u_i\rangle\langle\psi_f|\psi_i\rangle + \langle u_f|u_i\rangle\langle\psi_f|\mathbf{r}|\psi_i\rangle \tag{8.4}$$

In the case of direct interband transitions, the second term of the above expression is zero, because at the same point in the Brillouin zone, Bloch functions in two different bands are orthogonal. On the other hand, for the intersubband transitions, the first term gives zero because of the fact that the Hamiltonian used to obtain ψ_f and ψ_i is Hermitian [12]. In addition, the overlap between Bloch functions in the *same* band is equal to unity [13]. So that, for the intersubband case, the following matrix element is obtained

$$\langle\phi_f|\mathbf{r}|\phi_i\rangle \approx \langle\psi_f|\mathbf{r}|\psi_i\rangle \tag{8.5}$$

PAGE/PAGES EXCLUDED UNDER INSTRUCTION FROM UNIVERSITY

plane, with a polarisation vector, $\epsilon_1(\theta) = sin(\theta)\hat{x} + cos(\theta)\hat{z}$, and a k vector $\mathbf{k} = k[-cos(\theta)\hat{x} + sin(\theta)\hat{z}]$, where θ is the angle between the polarisation vector and the z direction, and the ϵ_2 polarisation is neglected since this polarisation cannot induce intersubband transitions [8]. Since the envelope wavefunctions of the confinement potential are also functions of z only, the only nonvanishing component of the dipole matrix element is $\langle\psi_f|z|\psi_i\rangle$. The intersubband dipole matrix element is therefore polarised in the z direction, and will be referred to in the rest of this chapter as $\langle z\rangle$.

8.4 Intersubband Third Order Nonlinearities

The large intersubband dipole infrared transition first observed and reported by West and Eglash [3] in 1985 has given rise to substantial interest and research in intersubband nonlinearities in recent years. The transition dipole matrix elements in semiconductor QWs, which are of the order of a few nanometres, give rise to potentially large optical nonlinearities, which can be further maximised by suitable design of the heterostructure [4] [6].

The properties possessed by intersubband transitions enable their energy levels to be tailored by suitable design of the wells and barriers as dictated by the appropriate use of semiconductor alloys, as well as by an applied electric field. In this chapter, this versatile characteristic of intersubband transitions is utilised in designing a multi-quantum well (MQW) structure containing energy levels appropriate for both triple harmonic generation (THG) and four wave mixing (FWM) by the mere expedient of the application of an electric field [9].

It is necessary that the structure energy levels behave appropriately as an electric field is applied and hence the use of a three well structure with energy levels localised in the respective wells as will be shown in the next section, making use of the well known fact that the energy of a confined state of a quantum well tracks the centre of the well as an electric field is applied and increased.

A single device with multiple functions is hence made possible, especially since investigations of the optical Kerr effect associated with intersubband transitions are also possible with this structure.

8.5 Structure Description

The structure is a three well structure with $In_{0.53}Ga_{0.47}As$ wells and AlAs barriers, shown in Figure 8.3. There are several techniques currently available to compensate for the high lattice mismatch between $In_{0.53}Ga_{0.47}As$ and AlAs, one of which is by growing the MQW structure on an InGaAs buffer layer with graded indium composition on a GaAs substrate [7].

The energy levels are localised in the wells as follows: E_1 and E_4 in the middle well, E_3 in the left well, and E_2 in the right. This arrangement is important as when a bias voltage is applied to the structure, energy level which is localised in the leftmost well will undergo the greatest increase in energy, followed by those in the middle well, and the right well respectively. Electric-field tunable $\chi^{(3)}$ for both THG (characterised by $\chi^{(3)}(3\omega = \omega + \omega + \omega)$) and

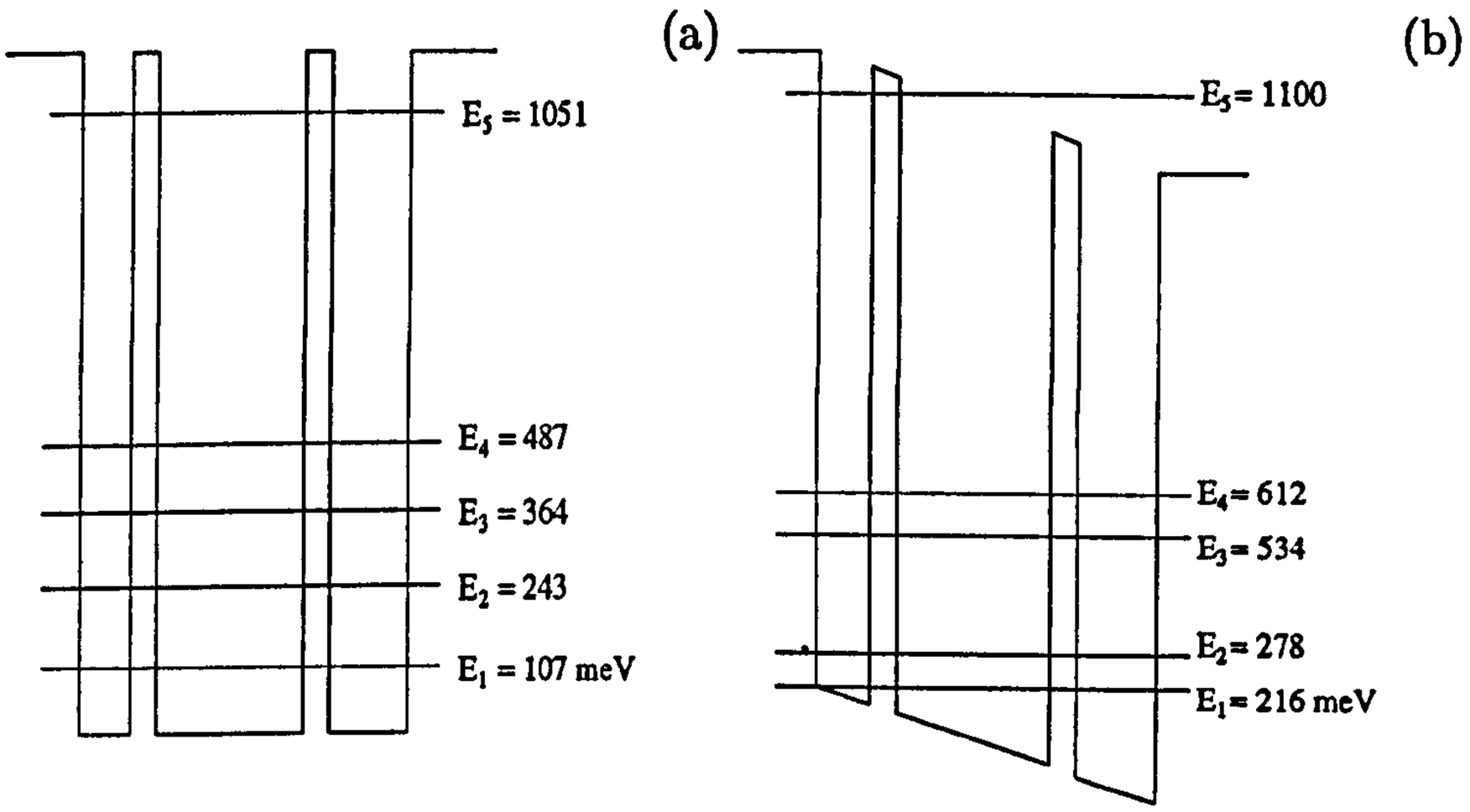

Figure 8.3: Conduction band diagrams of the AlAs/InGaAs coupled quantum well nonlinear optical structures for (a) THG at 0 meV bias, and (b) FWM at 200 meV bias. Shown are the positions of the positions of the calculated energy subbands. The widths of the InGaAs wells are 2.0 nm, 5.7 nm and 3.0 nm respectively, and are separated by 1.0 nm AlAs barriers.

FWM (characterised by $\chi^{(3)}(\omega_4 = 2\omega_1 - \omega_2)$) is then possible using same structure, with an applied bias voltage of less than 30 meV for THG, and more than 100 meV for FWM. Ideally, anti-crossing between the subbands should not occur otherwise the 4-1 matrix element, $\langle z_{14} \rangle$, will not be optimised, hence there is a limit to the maximum bias voltage which can be applied.

The energy states of the structure for THG may be pumped by e.g. a CO_2 laser [10], whereas those for FWM could make use of sources with wavelengths shorter than 5 μm such as holmium and erbium rare earth lasers and periodically poled lithium niobate optical parametric oscillators [11], where many interesting nonlinear optics applications exist. The nonlinearity is further enhanced because the processes will be triply resonant for small laser difference frequencies. i.e. the spacing between the relevant energy subbands will be equal to the pump photon energy.

Table 8.1: Energy states of the structure appropriate for THG at various applied bias, and their transition energies.

V_{bias}	E_1	E_2	E_3	E_4	V_{bias}	$E_2 - E_1$	$E_3 - E_2$	$E_4 - E_3$
10 meV	112	244	373	493	10 meV	132	129	120
20 meV	118	246	382	499	20 meV	128	136	118

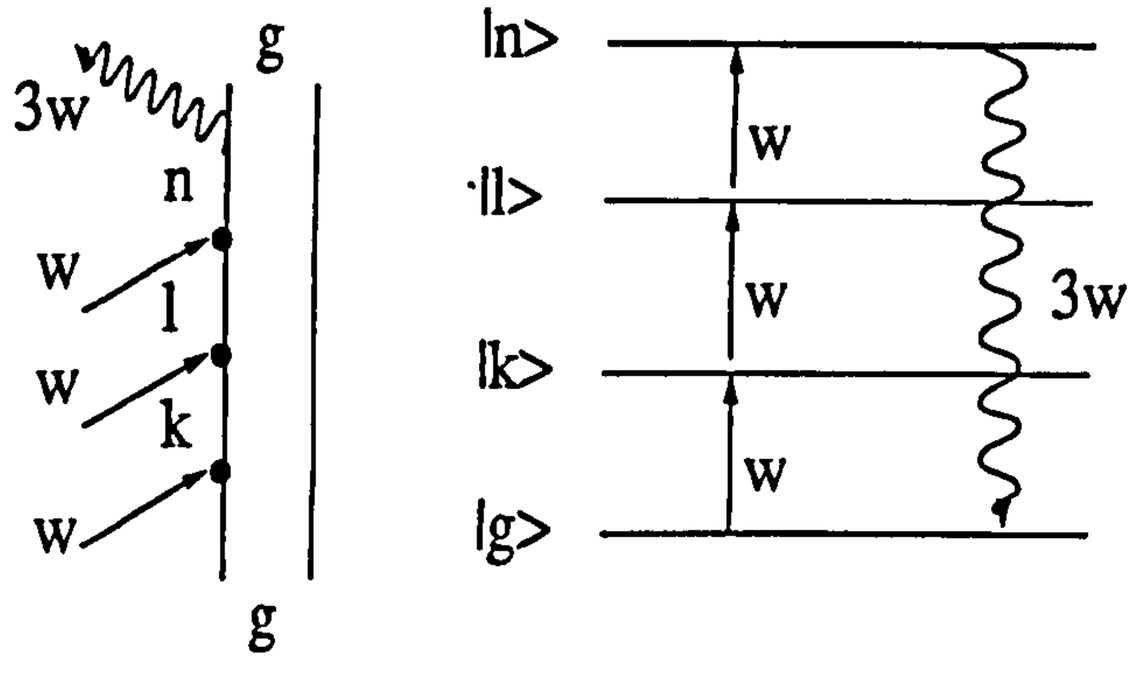

Figure 8.4: The double-sided Feynman diagram (left) for the triply resonant THG process shown on the right.

8.6 Third-Order Nonlinear Susceptibility Equations

There are eight basic diagrams for $\chi^{(3)}(\omega_4 = \omega_1 + \omega_2 + \omega_3)$, and six possible terms can be derived from each diagram, making a total of 48 terms altogether. In the case of THG, the number of terms collapse into eight, which in turn becomes only one when the process is triply resonant. The double-sided Feynman diagram which describes the triply resonant THG process is shown in Figure 8.4.

Following the simple rules outlined in the previous section, we obtain the following equation for the triply resonant THG process:

$$\chi^{(3)}(3\omega) = \frac{Ne^4}{\hbar^3\epsilon_0} \frac{\langle z_{gk}\rangle\langle z_{kl}\rangle\langle z_{ln}\rangle\langle z_{ng}\rangle}{(\omega - \omega_{kg} - i\Gamma_{kg})(2\omega - \omega_{lg} - i\Gamma_{lg})(3\omega - \omega_{ng} - i\Gamma_{ng})} \quad (8.6)$$

where Γ_{ij} are the scattering rates between the subbands i and j such that $\hbar\Gamma_{ij} = 7$ meV [14]. It is assumed that only the lowest level is thermally populated with a density of carriers $N = 5 \times 10^{17}$ cm^{-3}, and that the

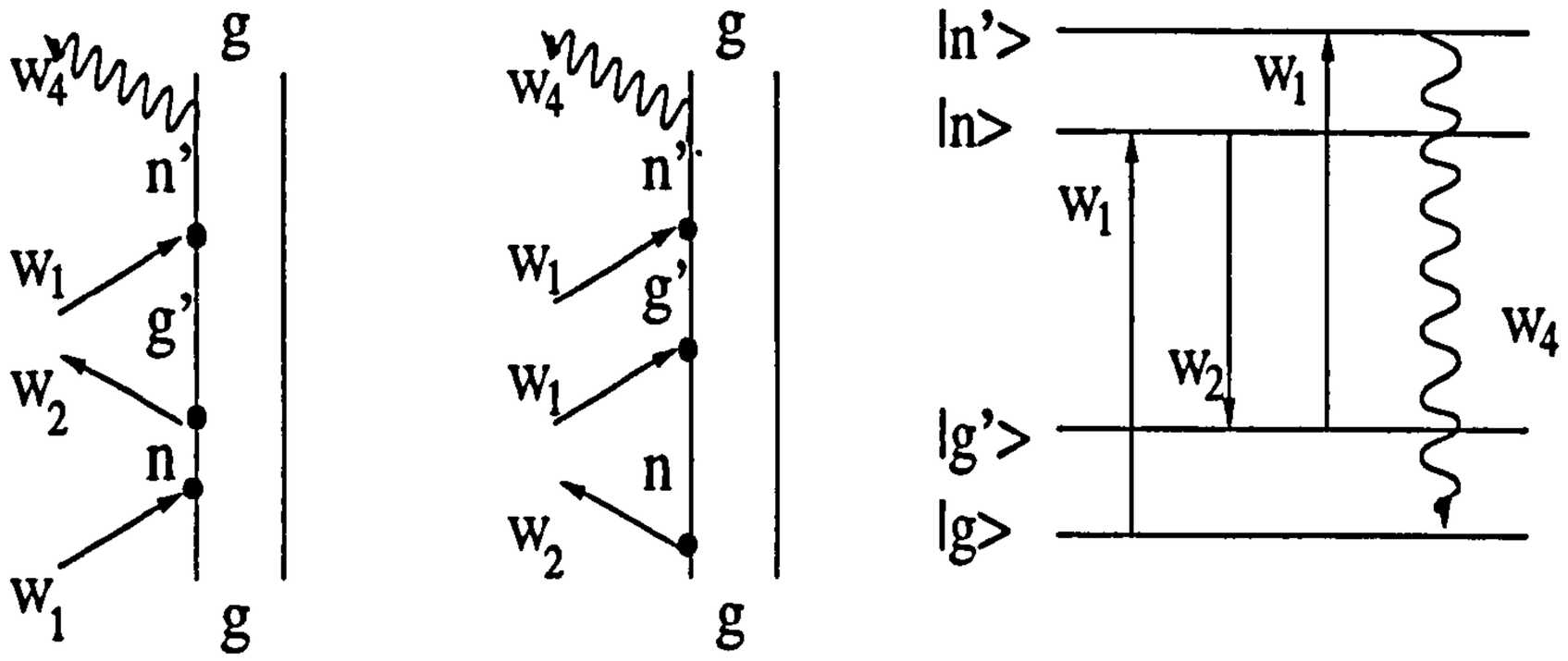

Figure 8.5: The double-sided Feynman diagrams (left and centre) for the case of the triply resonant FWM shown on the right.

pump beam is of frequency $\omega = 9.8\mu$m. Using the above values, a value of $|\chi^{(3)}(3\omega)| = 8.3 \times 10^{-14}$ (m/V)^2 is calculated.

Three terms can be derived from each of the 8 diagrams describing the various cases of the FWM process of $\chi^{(3)}(\omega_4 = 2\omega_1 + \omega_3)$, making a total of 24 terms altogether. These collapse into the two double-sided Feynman diagrams which describe the triply resonant FWM process that we are interested in [2], and these are explicitly shown in Figure 8.5.

From the above diagrams, two terms are obtained for the triply resonant FWM process, which when simplified becomes

$$\chi^{(3)} = \frac{Ne^4}{\hbar^3\epsilon_0} \frac{\langle z_{gn}\rangle\langle z_{ng'}\rangle\langle z_{g'n'}\rangle\langle z_{n'g}\rangle}{(\omega_1 - \omega_2 - \omega_{g'g} - i\Gamma_{g'g})(\omega_4 - \omega_{n'g} - i\Gamma_{n'g})} \times\Big[\frac{1}{(\omega_1 - \omega_{ng} - i\Gamma_{ng})} + \frac{1}{(-\omega_2 - \omega_{ng} - i\Gamma_{ng})}\Big] \tag{8.7}$$

where Γ_{ng} and $\Gamma_{n'g}$ are the intersubband scattering rates, and is estimated to be 2 ps [10]. $\Gamma_{g'g}$ is the effective intrasubband scattering rate, assumed to

be 0.1 ps [10], and the pump frequency $\omega_1 = 3.8\mu$m. Using the above values, a value of $|\chi^{(3)}(\omega_4)| = 1.1 \times 10^{-10}$ $(\mathrm{m/V})^2$ is found.

8.7 Conclusions

A MQW structure has been designed which is suitable for both THG and FWM, depending on the bias voltage which is applied. The calculated third order nonlinearities for THG, $\chi^{(3)}(3\omega)$, and for FWM, $\chi^{(3)}(\omega_4)$, have been found, and are comparable to those of the "single-use" structures reported in e.g. [15] (for THG), and in [10] (for FWM) respectively.

By applying different values of the bias voltage, the energy levels of the structure could be brought into resonance for optimising the third order nonlinearity. Moreover, the output frequency could also be tuned by changing the bias voltage, resulting in a multi-function tunable device. Similiar devices of this kind could be easily designed for operation at other frequencies of interest.

References

[1] Y. Prior, "A complete expression for the third-order susceptibility ($\chi^{(3)}$) - perturbative and diagrammatic approaches," *J. Quant. Electron.* **20**, pp. 37-42, 1984.

[2] Y. R. Shen, *The Principles of Nonlinear Optics*, Chap. 2, 14, Wiley, New York, 1984.

[3] L. C. West and S. J. Eglash, "First observation of an extremely large dipole infrared transition within the conduction band of a GaAs quantum well," *Appl. Phys. Lett.* **46**, pp. 1156-1157, 1985.

[4] S. Tomić, V. Milanović and Z. Ikonić, "Optimization of intersubband resonant second-order susceptibility in asymmetric graded $Al_xGa_{1-x}As$ quantum wells using supersymmetric quantum mechanics," *Phys. Rev. B* **56**, pp. 1033-1036, 1997.

[5] G. Bastard, *Wave mechanics applied to semiconductor heterostructures*, Chapter 7, Halsted Press, 1988.

[6] D. Indjin, Z. Ikonić. V. Milanović and J. Radovanović, "Optimization of resonant second- and third-order nonlinearities in step and continuously graded semiconductor quantum wells," *IEEE J. Quan. Electron.* **34**, pp. 795-802, 1998.

[7] H. C. Chui and J. S. Harris, Jr., "Growth studies on $In_{0.5}Ga_{0.50}As$/AlGaAs quantum wells grown on GaAs with a linearly graded InGaAs buffer," *J. Vac. Sci. Techonol. B* **12**, pp. 1019-1022, 1994.

[8] A. Sa'ar, "On the question of intersubband electric quadrupole transitions in a quantum well structure," *J. Appl. Phys.* **74**, pp. 5263-5265, 1993.

[9] C. Y. L. Cheung, K. A. Shore and P. Rees, Manuscript in preparation.

[10] D Walrod, S Y Auyang, P A Wolff and M Sugimoto, "Observation of third order nonlinearity due to intersubband transitions in AlGaAs/GaAs superlattices," *Appl. Phys. Lett.* **59**, pp. 2932-2934, 1991.

[11] W S Rabinovich, G Beadie and D S Katzer, "Intersubband χ^3 in coupled InGaAs-AlGaAs multiple quantum wells," *J. Quant. Electron.* **34**, pp. 975-981, 1998.

[12] D. D. Coon and R. P. G. Karunasiri, "New mode of IR detection using quantum wells," *Appl. Phys. Lett.* **45**, pp. 649-651, 1984.

[13] L. A. Coldren and S. W. Corzine, *Diode Lasers and Photonic Integrated Circuits*, Chapter 4, John Wiley & Sons, New York, 1995.

[14] E. Rosencher, P.Bois, J. Nagle and S. Delaitre, "Second harmonic generation by intersubband transitions in compositionally asymmetrical MQWs," *Electronics Letters* **25**, pp. 1063-1065, 1989.

[15] F. Capasso, C. Sirtori and A. Y. Cho, "Coupled quantum well semiconductors with giant electric field tunable nonlinear optical properties in the infrared," *J. Quant. Electron.* **30**, pp. 1313-1326, 1994.

Chapter 9

Conclusions

9.1 Introduction

This thesis has been concerned with the optical properties of intersubband devices and waveguides, with particular attention being paid to accessing THz bandwidths in directly modulated intersubband semiconductor lasers, and the optical gain achievable in these devices. Specifically, three main aspects of the optical properties of intersubband devices have been studied, namely the waveguiding properties of quantum cascade lasers (QCLs), the anticipated modulation bandwidth, gain and threshold current of intersubband lasers, and the engineering of nonlinear susceptibilities in intersubband quantum well structures.

A particular context where THz modulation bandwidths would be of interest is in optical fibre communications where significant changes in available system performances have occured recently, with considerable attention being given to the use of wavelength division multiplexing (WDM) techniques.

In this context, a perception is emerging that data transmission at THz data rates may become a systems requirement sooner rather than later. The direct approach to meeting such requirements has already been taken, e.g. by multiplexing 100 sources at 10 Gbits/s. An ultimately simpler approach may be feasible based on the development of near-infrared (NIR) unipolar intersubband lasers, which has been assessed to be capable of both high gain and fast direct modulation rates.

In the following sections, the significance of the results obtained from an investigation of these various aspects of the optical properties of semiconductor lasers is summarized. Proposals for future work which may be undertaken to further enhance the understanding of these optical properties, as well as utilise and expand upon the existing knowledge in related work, are also presented.

9.2 Conclusions and Further Work

9.2.1 Optical Waveguiding Properties of Quantum Cascade Lasers

In a conventional semiconductor laser, the epitaxial layers grown on either side of the active region are usually chosen to form a waveguide normal to these layers. It is this variant of waveguide that has been studied here, using the numerical method detailed in Chapter 2 which allows the supported modes and their corresponding losses or gain to be found. An improvement to the structure used in the QCL by Faist *et al* was made from the sensitivity

analysis, resulting in a simpler waveguide structure, as well has better mode confinement.

More recent advances in the design of optical waveguides for QCLs have been reported by C. Gmachl *et al* (*Science* **280**, p.1556, 1998) where the incorporation of the QCL into a microdisk waveguide has resulted in a dramatic increase in the output power intensity and decrease of threshold current achievable from such devices. It appears that this would be the direction to go into for further QCL work, in addition to diversifying into QCL intersubband structures for NIR and far-infrared (FIR) lasing. Further work may be undertaken in this regard by modifying the waveguide Helmholtz Equation solver to solve for modes in microcavities.

Moreover, although the lower threshold current of the interband cascade lasers might, at first glance, make them the preferred choice for mid-infrared lasing, QCLs has several advantages over the interband structures, most obviously, the fact that QCLs are not only tunable, but using a single material system, e.g. AlInAs/GaInAs, a range of wavelengths (from 3.5 - 17 μm for AlInAs/GaInAs) may be obtained. Investigations into the possibilities of using different materials, such as GaAs/AlGaAs, have already been undertaken by various researchers (see e.g. Li *et al*, *Appl. Phys. Lett.* **72**, p.2141, 1998; Sirtori, Invited talk, Vertical Transport and Intersubband Processes in Low Dimensional Structures, Sheffield, Oct. 1998.)

9.2.2 Rate Equations and Modulation Bandwidth of Intersubband Lasers

Analytical expressions for the population inversion condition and threshold current of a triple quantum well (TQW) intersubband structure were derived in Chapter 4, using a four-level rate equation model. An analytical expression for the modulation response of the TQW structure has also been found for a special case of equal tunneling times between the relevant wells of the structure. Using this expression, it has been found that the maximum response frequency is dependent upon carrier lifetimes. It was also found that the modulation response does not increase monotonically with the output power, and that there exists an optimum optical output power for maximum attainable response frequency.

The four-level rate equation model has also been used to study the dynamics of intersubband lasers for the general case of unequal lifetimes, in order to confirm the results of the earlier analytical model. A more self-consistent calculation was also undertaken in Chapter 5, where the relevant lifetimes were deduced from calculations of electronic wavefunctions of the two TQW structures designed for MIR and NIR lasing which were presented here, and the requirements that were considered in their design prescribed.

The unique dependence of the modulation bandwidth upon the output power of the laser found previously in Chapter 4 was also repeated in Chapter 5. For intersubband structures, in contrast with interband semiconductor lasers, there is a fine balance between the contributions of the resonance

frequency and the damping factor in the determination of the maximum modulation frequency due to the picosecond carrier lifetimes which are characteristic of such structures. The fact that these lifetimes are of the same order, or shorter than, the photon lifetime indicates that the achievable direct modulation bandwidth is essentially determined by the photon lifetime, and hence, improvements should be obtained by using device design parameters which results in a reduction of the photon lifetime. There is, however, a trade-off in this aspect as higher gain would then be required since the losses would be higher for a smaller photon lifetime.

The effect of the state lifetimes of the energy levels, which are an indication of how long the electron remains within the structure at that energy level, should also be taken in consideration and included in the rate equation model for completeness.

9.2.3 Intersubband Optical Gain

In Chapter 6, an expression describing the optical gain in intersubband devices was derived by drawing on similiarites between the general gain expression and corresponding terms for the intersubband case. The resulting expression was found to be similiar to that derived in another work by Gorfinkel *et al*, except that the one presented here uses a reduced effective mass.

The rate equation model has also been used in developing a self-consistent model of the optical gain of intersubband lasers, together with this optical gain equation in Chapter 7. Here it was found that for the same gain, the

threshold current for the NIR structure is an order of magnitude less than that of the MIR structure. This is attributed to the fact that the materials used in designing the NIR TQW structure has a lower effective mass that those used in the MIR case, and hence the carrier population density is higher for the NIR structure.

The inclusion of the more detailed treatment of the phonon scattering events presented by Kisin *et al* (*J. Appl. Phys.* **82**, p.2031, 1997) into the lineshape function could be undertaken for future work. It would also be of interest to apply the model to the study of FIR intersubband structures. Here, the fact that the transition is less than the optical phonon energy means that electron-electron scattering needs to be considered, and so the lineshape function would be altered accordingly. This aspect would be of interest for future consideration.

9.2.4 Intersubband Nonlinearities

In Chapter 8, an intersubband structure designed for both triple harmonic generation (THG) and four-wave mixing (FWM) was presented, and the third-order nonlinear susceptibilities (χ^3) appropriate for these functions were calculated. The application of an appropriate electric field would alter the enrgy levels in the structure in such a manner so that when optically pumped at the appropriate frequency, the relevant processes would take place.

It should be noted, however, that the calculations only take into consid-

eration the resonant cases. It should therefore, be of interest to develop a computational model to take into account the nonresonant cases, and which has the full 48 terms of the χ^3, in order to investigate the changes which take place as the electric field applied to the structure is increased or decreased. A simpler study with regard to the second-order susceptibility could also be undertaken.

9.3 Other Developments

9.3.1 Photonic Bandgaps

A photonic bandgap (PBG) crystal is a periodic composite structure with a frequency gap in which all optical electromagnetic modes are forbidden. The originators of the concept were Yablonovich and John, who suggested it in 1987. Primary applications of such structures include all-angle reflecting mirrors, band-pass and band-stop filters, and finally, waveguides and resonators. Among the principal current problems encountered by researchers in this field is the development of appropriate mathematical tools for analysis and design of these structures in practical geometries. The waveguide solver could be expanded into three dimensions, with some imagination, to enable the design of PBG structures for theoretical and experimental investigations.

9.3.2 Nonlinearities in Cantor and Fibonacci Structures

The study of the nonlinear optical response of Cantor-like and Fibonacci-like quasiperiodic structures is an interesting field. The application of such

structures in optical waveguides can be seen as an extension of the analysis of semiconductor multilayered optical waveguides, such as ridge waveguide structures and Bragg optical waveguides, where previous analysis of a defocusing optical nonlinearity in such waveguides has already given rise to interesting results (see e.g. Lambkin and Shore, *IEEE J. Quant. Electron.* **14** p.2046, 1988, and *IEEE J. Quant. Electron.* **27**, p.824, 1991.) Further studies could be undertaken in this direction using the waveguide solver described in Chapter 2.

9.3.3 The Poisson Equation

When carriers are injected into a MQW structure, the presence of the electrons modifies its band structure, and therefore, its energy levels. Solving the Poisson and Schrödinger Equations concurrently could enable this accumulative space charge effect associated with the application of a bias voltage to an extended MQW structure to be taken into account. Hence, complex superlattice-type structures such as the QCL injector and its active region may then be modelled.

Appendix A

Basic Complex Variable Theory and Mathematical Definitions

A.1 Terms and Concepts when Dealing with Complex Functions

Continuity. A function f is said to be *continuous* at a point z_0 is all three of the following conditions are satisfied:

$$\text{(i)} \quad \lim_{z \to z_0} f(z) \text{exists},$$

$$\text{(ii)} \quad f(z_0) \text{exists},$$

$$\text{(iii)} \quad \lim_{z \to z_0} f(z) = f(z_0).$$

Note that statement (iii) actually contains statements (i) and (ii); for the existence of the quantity on each side of the equation is implicit. Statement (iii) says that for each positive number ϵ, there is a positive number δ such

that

$$|f(z) - f(z_0)| < \epsilon. \qquad \text{whenever } |z - z_0| < \delta \cdot$$

A function of a complex variable is said to be continuous in a region R if it is continuous at each point in R.

Derivatives. Let f be a function whose domain of definition contains a neighborhood of a point z_0. We define the derivative of f at z_0, written as $f'(z_0)$, by the equation

$$f'(z_0) = \lim_{z \to z_0} \frac{f(z) - f(z_0)}{z - z_0} \tag{A.1}$$

provided the limit here exists. The function f is said to be differentiable at z_0 when its derivative at z_0 exists.

Analytic Functions. A function f of the complex variable z is analytic at a point z_0 if its derivative exists not only at z_0 . It is analytic in a region R if it is analytic at every point in R. The term holomorphic is also used to denote analyticity.

If a function f is analytic in a region R, then about each point z of R there must be a neighbourhood on which f is defined. This means that z must be an interior point of the domain of definition, and so analytic functions are usually defined on domains. If, however, an analytic function f is said to be on a closed disk $|z| \leq 1$, for example, it is to be understood that f is analytic throughout some domain containing that disk.

An *entire* function is a function that is analytic at each point in an entire plane. Since the derivative of a polynomial exists everywhere, it follows that every polynomial is an entire function.

Singularities. If a function fails to be analytic at a point z_0 but is analytic at some point in every neighbourhood of z_0, then z_0 is called a *singular point*, or *singularity*, of the function. For exmaple, if

$$f(z) = \frac{1}{z}; \qquad \text{then } f'(z) = -\frac{1}{z^2} \qquad (z \neq 0).$$

Hence, f is analytic at every point except for $z = 0$ where it is not even defined. The point $z = 0$ is therefore a singular point. On the othe rhand, the function $f(z) = |z|^2$ has no singular points since it is nowhere analytic.

A.2 Contour Integrals

An arc C is a set of points $z = (x, y)$ in the complex plane such that

$$x = x(t), \qquad y = y(t) \qquad (a \leq t \leq b) \tag{A.2}$$

where $x(t)$ and $y(t)$ are continuous functions of the real parameter t. This definition establishes a continous mapping of the interval $a \leq t \leq b$ into the xy plane, and the image points are ordered according to increasing values of t. It is convenient to describe the points of C by the equation

$$z = z(t) = x(t) + jy(t) \qquad (a \leq t \leq b) \tag{A.3}$$

and we say that $z(t)$ is continous since $x(t)$ and $y(t)$ are both continuous.

A *contour*, or piecewise smooth arc, is an arc consisting of a finite number of smooth arcs joined end to end. If Equation (B.3) represents a contour, then $x(t)$ and $y(t)$ are continuous, whereas their first derivatives are piecewise continuous.

When only the initial and final values of $z(t)$ are the same, a contour C is called a simple closed contour. Examples are the circle, as well as the boundary of a triangle or a rectangle taken in a specific direction. The length of a contour or a simple closed contour is the sum of the lengths of the smooth arcs which make up the contour.

Line and Contour Integrals. The definite integral of a complex-valued function f of the complex variable z, can be defined in terms of the values $f(z)$ along a given contour C extending from a point $z = \alpha$ to a point $z = \beta$ in the complex plane. It is, therefore, a line integral, and its value depends upon the contour C as well as the function f. Such an integral is written

$$\int_C f(z)dz \qquad or \qquad \int_\alpha^\beta f(z)dz;$$

the latter notation is often used when the value of the integral is independent of the choice of the contour direction taken between the two end points.

A *contour integral* is a special type of line integral, where the value of the integral is affected by the choice of path direction taken between two end points. The positive direction of trversal is, by convention, taken to be counter-clockwise (CCW), and if a clockwise (CW) direction is chosen, the sign of the integral is opposite to that which would be obtained if a CCW

direction had been taken.

A.3 Mathematical definitions

Hermitian. Let † denote the adjoint, where $A^\dagger$ is the adjoint operator corresponding to the operator A. Then $A^\dagger$ is defined by:

$$\langle A^\dagger \phi | \varphi \rangle = \langle \phi | A\varphi \rangle \qquad \text{for any } \phi, \varphi \tag{A.4}$$

The operator A is then self-adjoint, or Hermitian, if

$$A^\dagger = A \tag{A.5}$$

so that Equation (A.4) now becomes

$$\langle A\phi | \varphi \rangle = \langle \phi | A\varphi \rangle \quad , \text{for any } \phi, \varphi \tag{A.6}$$

Orthogonal. Two complex functions, $\psi_1(z)$ and $\psi_2(z)$, are orthogonal if

$$\int \psi_1(z)\psi_2^*(z)dz = 0 \tag{A.7}$$

where ψ_2^* is the complex conjugate of ψ_2.

Orthonormal. Similarly, two functions, $\psi_1(z)$ and $\psi_2(z)$, are orthonormal if

$$\int \psi_1(z)\psi_2^*(z)dz = 1 \tag{A.8}$$

A.4 The Liouville Equations. (Chapter 8)

In order to find the microscopic expressions for nonlinear susceptibilities, a quantum mechanical calculation is often required. The density matrix formalism is usually the most convenient for such calculations especially when

relaxations or excitations have to be dealt with. The following is a modified excerpt from Shen, *The Principles of Nonlinear Optics*, Chap. 2, John Wiley & Sons, 1984.

Let ψ be the wave function of the material system under of the electromagnetic field. Then the density matric operator is defined as the ensemble average over the product of the ket and bra state vectors

$$\rho = \bar{|\psi\rangle\langle\psi|} \tag{A.9}$$

and the ensemble average of a physical quantity $\mathbf{P}$ is given by

$$\begin{aligned} \langle \mathrm{P} \rangle &= \langle \psi | \bar{\mathrm{P}} | \psi \rangle \\ &= \mathrm{Tr}(\rho \mathrm{P}) \end{aligned} \tag{A.10}$$

where $\mathbf{P}$ is the electric polarization. From the definition of ρ in Equation (A.10), and from the Schrödinger equation for ψ, the equation for motion for ρ can be obtained

$$\frac{\partial \rho}{\partial t} = \frac{1}{i\hbar}[\mathcal{H}, \rho], \tag{A.11}$$

known as the Liouville equation. The Hamiltonian $\mathcal{H}$ is composed of three parts

$$\mathcal{H} = \mathcal{H}_0 + \mathcal{H}_{int} + \mathcal{H}_{random} \tag{A.12}$$

where $\mathcal{H}_0$ is the Hamiltonian of the unperturbed material system, $\mathcal{H}_{int}$ is the interaction Hamiltonian describing the interaction of light with matter, and $\mathcal{H}_{random}$ is a Hamiltonian describing the random perturbation on the system. The Hamiltonian $\mathcal{H}_{random}$ is responsible for the relaxation of the perturbed ρ back to equilibrium. Equation (A.12) can then be expressed as

$$\frac{\partial \rho}{\partial t} = \frac{1}{i\hbar}[\mathcal{H}_0 + \mathcal{H}_{int}, \rho] + \left(\frac{\partial \rho}{\partial t}\right)_{relax} \tag{A.13}$$

with

$$\left(\frac{\partial \rho}{\partial t}\right)_{relax} \equiv \frac{1}{i\hbar}[\mathcal{H}_{random}, \rho] \tag{A.14}$$

In principle, if $\mathcal{H}_0$, $\mathcal{H}_{int}$ and $\left(\frac{\partial \rho}{\partial t}\right)_{relax}$ are known, then the Liouville equations in Equation (A.14) togther with Equation (A.11) fully describe the response of the medium to the incoming field. In general, however, it is not possible to combine these equations together into a single equation of motion for $\langle \mathbf{P} \rangle$, it can be accomplished only in special cases.

Appendix B

Rate Equations and Modulation Response of the Three Well Structure

B.1 Derivation of ΔN

Starting from Equations (4.8)-(4.10) in Chapter 4 and rearranging, the following equations are obtained

$$\frac{J}{e} + \frac{L_2 N_2^{(2)}}{\tau_{12}} - \frac{L_1 N_1}{\tau_{12}} = 0 \tag{B.1}$$

$$\frac{L_1 N_1}{\tau_{12}} - \frac{L_2 N_2^{(2)}}{\tau_{12}} - \frac{L_2 N_2^{(2)}}{\tau_S} = 0 \tag{B.2}$$

$$\frac{L_2 N_2^{(2)}}{\tau_S} + \frac{L_3 N_3}{\tau_{23}} - \frac{L_2 N_2^{(1)}}{\tau_{23}} = 0$$

$$L_3 N_3 = \tau_{23} L_2 \left(\frac{N_2^{(1)}}{\tau_{23}} - \frac{N_2^{(2)}}{\tau_S} \right) \tag{B.3}$$

From Equation (4.7),

$$L_1 N_1 = \frac{J\tau_T}{e} - \dot{L}_2(N_2^{(2)} + N_2^{(1)}) - L_3 N_3 \tag{B.4}$$

The expressions below are then found by substituting both Equations (B.3) and (B.4) into Equations (B.1) and (B.2),

$$\frac{J}{e}\left(1 - \frac{\tau_T}{\tau_{12}}\right) + \frac{L_2 N_2^{(2)}}{\tau_{12}}\left(2 - \frac{\tau_{23}}{\tau_S}\right) + \frac{2L_2 N_2^{(1)}}{\tau_{12}} = 0 \tag{B.5}$$

$$\frac{J\tau_t}{e\tau_{12}} + L_2 N_2^{(2)}\left(-\frac{2}{\tau_{12}} - \frac{1}{\tau_S} + \frac{\tau_{23}}{\tau_{12}\tau_S}\right) - \frac{2L_2 N_2^{(1)}}{\tau_{12}} = 0 \tag{B.6}$$

Equations (B.5) and (B.6) are respectively of the form

$$A_1 + B_1 N_2^{(2)} + C_1 N_2^{(1)} = 0 \tag{B.7}$$

$$A_2 + B_2 N_2^{(2)} + C_2 N_2^{(1)} = 0 \tag{B.8}$$

where

$$A_1 = \tfrac{J}{e}\left(1 - \tfrac{\tau_T}{\tau_{12}}\right) \qquad A_2 = \tfrac{J\tau_T}{e\tau_{12}}$$
$$B_1 = \tfrac{L_2}{\tau_{12}}\left(2 - \tfrac{\tau_{23}}{\tau_S}\right) \qquad B_2 = L_2\left(-\tfrac{2}{\tau_{12}} - \tfrac{1}{\tau_S} + \tfrac{\tau_{23}}{\tau_{12}\tau_S}\right)$$
$$C_1 = \tfrac{2L_2}{\tau_{12}} \qquad C_2 = -\tfrac{2L_2}{\tau_{12}}$$

Multiplying Equation (B.7) by C_2, and Equation (B.8) by C_1:

$$C_2 \times \text{(B.7)} \;:\; A_1 C_2 + B_1 C_2 N_2^{(2)} + C_1 C_2 N_2^{(1)} = 0 \tag{B.9}$$

$$C_1 \times \text{(B.8)} \;:\; A_2 C_1 + B_2 C_1 N_2^{(2)} + C_2 C_1 N_2^{(1)} = 0$$

$$C_2 C_1 N_2^{(1)} = -A_2 C_1 - B_2 C_1 N_2^{(2)} \tag{B.10}$$

And substituting the resulting Equation (B.10) into Equation (B.9), an expression for $N_2^{(2)}$ is found, where

$$N_2^{(2)} = \frac{A_2 C_1 - A_1 C_2}{B_1 C_2 - B_2 C_1} \tag{B.11}$$

By putting Equation (B.11) back into Equation (B.10), a similiar expression for $N_2^{(1)}$ may also be obtained

$$N_2^{(1)} = \frac{A_1 B_2 - A_2 B_1}{B_1 C_2 - B_2 C_1} \tag{B.12}$$

And so,

$$\begin{aligned} \Delta N &= N_2^{(2)} - N_2^{(1)} \\ &= \frac{A_2 C_1 - A_1 C_2}{B_1 C_2 - B_2 C_1} - \frac{A_1 B_2 - A_2 B_1}{B_1 C_2 - B_2 C_1} \\ &= \frac{A_1(-C_2 - B_2) + A_2(C_1 + B_1)}{B_1 C_2 - B_2 C_1} \end{aligned} \tag{B.13}$$

The actual expression for each of the above terms can then be found by replacing the corresponding expressions from Equations (B.6) and (B.7),

$$\begin{aligned} A_1(-C_2 - B_2) &= \frac{JL_2}{e\tau_S(\tau_{12})^2}\Big[4\tau_{12}\tau_S + (\tau_{12})^2 - \tau_{12}\tau_{23} - 4\tau_T\tau_S - \tau_{12}\tau_T \\ &\qquad + \tau_T\tau_{23}\Big] \end{aligned} \tag{B.14}$$

$$A_2(C_1 + B_1) = \frac{JL_2\tau_T}{e\tau_s(\tau_{12})^2}\Big(4\tau_S - \tau_{23}\Big) \tag{B.15}$$

$$B_1 C_2 - B_2 C_1 = \frac{2(L_2)^2}{\tau_{12}\tau_S} \tag{B.16}$$

So the

$$\begin{aligned} \text{Numerator} &= A_1(-C_2 - B_2) + A_2(C_1 + B_1) \\ &= \frac{JL_2}{e\tau_S\tau_{12}}\Big(4\tau_S + \tau_{12} - \tau_{23} - \tau_T\Big) \\ \text{and the Denominator} &= \frac{2(L_2)^2}{\tau_{12}\tau_S} \end{aligned}$$

And finally,

$$\Delta N = \frac{J}{2eL_2}[4\tau_S + \tau_{12} - \tau_{23} - \tau_T] \tag{B.17}$$

B.2 Deriving the Photon Density in terms of the Current Density

Rearranging the rate equations above threshold, Equations (4.16) - (4.18), and substituting $\Delta N = N_2^{(2)} - N_2^{(1)}$ for $1/(a\tau_P)$ where applicable

$$\frac{L_2 N_2^{(2)}}{\tau_{12}} - \frac{L_1 N_1}{\tau_{12}} + \frac{J}{e} = 0 \tag{B.18}$$

$$\frac{L_1 N_1}{\tau_{12}} - \frac{L_2 N_2^{(2)}}{\tau_{12}} - \frac{L_2 P}{\tau_P} - \frac{L_2 N_2^{(2)}}{\tau_S} = 0 \tag{B.19}$$

$$\frac{L_2 P}{\tau_P} + \frac{L_2 N_2^{(2)}}{\tau_S} + \frac{L_3 N_3}{\tau_{23}} - \frac{L_2 N_2^{(1)}}{\tau_{23}} = 0$$

$$L_3 N_3 = L_2 \tau_{23} \left[\frac{N_2^{(1)}}{\tau_{23}} - \frac{N_2^{(2)}}{\tau_S} - \frac{P}{\tau_P} \right] \tag{B.20}$$

And substituting both Equations (B.4) and (B.20) into Equations (B.18) and (B.19), the following expressions are obtained:

$$\frac{J}{e}\left(1 - \frac{\tau_T}{\tau_{12}}\right) + \frac{L_2 N_2^{(2)}}{\tau_{12}}\left(2 - \frac{\tau_{23}}{\tau_S}\right) + \frac{2 L_2 N_2^{(1)}}{\tau_{12}} - \frac{L_2 P \tau_{23}}{\tau_P \tau_{12}} = 0 \tag{B.21}$$

$$\frac{J \tau_T}{e \tau_{12}} + L_2 N_2^{(2)}\left(- \frac{2}{\tau_{12}} - \frac{1}{\tau_S} + \frac{\tau_{23}}{\tau_{12}\tau_S}\right) - \frac{2 L_2 N_2^{(1)}}{\tau_{12}} + \frac{L_2 P}{\tau_P}\left(\frac{\tau_{23}}{\tau_{12}} - 1\right) = 0 \tag{B.22}$$

which are respectively of the forms of Equations (B.7) and (B.8) but now,

$$A_1 = \frac{J}{e}\left(1 - \frac{\tau_T}{\tau_{12}}\right) - \frac{L_2 P \tau_{23}}{\tau_P \tau_{12}} \qquad A_2 = \frac{J \tau_T}{e \tau_{12}} + \frac{L_2 P}{\tau_P}\left(\frac{\tau_{23}}{\tau_{12}} - 1\right)$$

$$B_1 = \frac{L_2}{\tau_{12}}\left(2 - \frac{\tau_{23}}{\tau_S}\right) \qquad B_2 = L_2\left(- \frac{2}{\tau_{12}} - \frac{1}{\tau_S} + \frac{\tau_{23}}{\tau_{12}\tau_S}\right)$$

$$C_1 = \frac{2 L_2}{\tau_{12}} \qquad C_2 = -\frac{2 L_2}{\tau_{12}}$$

Referring to Equation (B.13), the terms in the numerator and the denominator are

$$A_1(-C_2 - B_2) = \frac{L_2}{\tau_{12}}\left[\frac{J}{e}\left(4 + \frac{\tau_{12}}{\tau_S} - \frac{\tau_{23}}{\tau_S}\right) - \frac{J\tau_T}{e\tau_{12}}\left(4 + \frac{\tau_{12}}{\tau_S} - \frac{\tau_{23}}{\tau_S}\right) - \frac{L_2 P\tau_{23}}{\tau_P\tau_{12}}\left(4 + \frac{\tau_{12}}{\tau_S} - \frac{\tau_{23}}{\tau_S}\right)\right] \quad \text{(B.23)}$$

$$A_2(C_1 + B_1) = \frac{L_2}{\tau_{12}}\left[\frac{4J\tau_T}{e\tau_{12}} - \frac{J\tau_T\tau_{23}}{e\tau_S\tau_{12}} + \frac{4L_2P\tau_{23}}{\tau_P\tau_{12}} - \frac{L_2P(\tau_{23})^2}{\tau_P\tau_{12}\tau_S} - \frac{4L_2P}{\tau_P} + \frac{L_2P\tau_{23}}{\tau_P\tau_S}\right] \quad \text{(B.24)}$$

$$B_1C_2 - B_2C_1 = \frac{2(L_2)^2}{\tau_{12}\tau_S} \quad \text{(B.25)}$$

where the

$$\text{Numerator} = \frac{L_2}{\tau_{12}}\left[\frac{J}{e}\left(4 + \frac{\tau_{12}}{\tau_S} - \frac{\tau_{23}}{\tau_S} - \frac{\tau_T}{\tau_S}\right) - \frac{4L_2P}{\tau_P}\right]$$

And so,

$$\Delta N = \frac{J}{2eL_2}\left(4\tau_S + \tau_{12} - \tau_{23} - \tau_T\right) - \frac{2P\tau_S}{\tau_P} \quad \text{(B.26)}$$

As the value for ΔN remains clamped at its threshold value even above the lasing, $\Delta N = 1/(a\tau_P)$, so an expression for the current density as a function of the photon density is obtained

$$J = \frac{2eL_2(1 + 2aP\tau_S)}{a\tau_P Z} \quad \text{(B.27)}$$

where $Z = 4\tau_S + \tau_{12} - \tau_{23} - \tau_T$, and recalling the expression for threshold current density, J_{th}, from Equation (4.14),

$$J_{th} = \frac{2eL_2}{a\tau_P Z} \quad \text{(B.28)}$$

Then, the photon density may be written as

$$\frac{J}{J_{th}} = 1 + 2aP\tau_S$$

$$P = \frac{1}{2a\tau_S}\left(\frac{J}{J_{th}} - 1\right) \quad \text{(B.29)}$$

B.3 Small Signal Analysis

Considering Equations (4.30) and (4.31), and assuming that $\tau_{12} = \tau_{23} = \tau_W$, the following expressions are obtained:

$$\frac{\mathrm{d}n_2^{(2)}}{\mathrm{d}t} = \frac{L_1}{L_2}\frac{n_1}{\tau_W} - \frac{n_2^{(2)}}{\tau_W} - \frac{p}{\tau_P} - a\bar{P}n_d - \frac{n_2^{(2)}}{\tau_S} \tag{B.30}$$

$$\frac{\mathrm{d}n_2^{(1)}}{\mathrm{d}t} = \frac{L_3}{L_2}\frac{n_3}{\tau_W} - \frac{n_2^{(1)}}{\tau_W} + \frac{p}{\tau_P} + a\bar{P}n_d + \frac{n_2^{(2)}}{\tau_S} \tag{B.31}$$

Subtracting Equation (B.31) from Equation (B.30), and using Equation (4.34), where $n_1 L_1 = J_m(t)\tau_T/e - n_s L_2 - n_3 L_3$, results in

$$\begin{aligned}\frac{\mathrm{d}n_d}{\mathrm{d}t} &= \frac{L_1 n_1 - L_3 n_3}{L_2 \tau_W} - \frac{n_d}{\tau_W} - \frac{2p}{\tau_P} - 2a\bar{P}n_d - \frac{2n_2^{(2)}}{\tau_S} \\ &= \frac{1}{\tau_W}\left(\frac{J_m(t)\tau_T}{eL_2} - n_s - \frac{2L_3 n_3}{L_2}\right) - n_d\left(2a\bar{P} + \frac{1}{\tau_W}\right) \\ &\quad - \frac{2n_2^{(2)}}{\tau_S} - \frac{2p}{\tau_P}\end{aligned} \tag{B.32}$$

Noting that $n_2^{(2)} = 1/2(n_d + n_s)$,

$$\begin{aligned}\frac{\mathrm{d}n_d}{\mathrm{d}t} &= \frac{1}{\tau_W}\left(\frac{J_m(t)\tau_T}{eL_2} - n_s - \frac{2L_3 n_3}{L_2}\right) - n_d\left(2a\bar{P} + \frac{1}{\tau_W} + \frac{1}{\tau_S}\right) \\ &\quad - \frac{n_s}{\tau_S} - \frac{2p}{\tau_P}\end{aligned} \tag{B.33}$$

Adding Equations (B.30) and (B.31), gives

$$\begin{aligned}\frac{\mathrm{d}n_s}{\mathrm{d}t} &= \frac{L_1 n_1 + L_3 n_3}{L_2 \tau_W} - \frac{n_s}{\tau_W} \\ &= \frac{J_m(t)\tau_T}{eL_2\tau_W} - \frac{2n_s}{\tau_W}\end{aligned} \tag{B.34}$$

However, since $n_s = n_2^{(2)} + n_2^{(1)}$, and any change in $n_2^{(2)}$ will result in a similiar change in $n_2^{(1)}$, as may be observed in Figure B.1, it can be assumed that $\mathrm{d}n_s/\mathrm{d}t \approx 0$. So,

$$n_s = \frac{J_m(t)\tau_T}{2eL_2} \tag{B.35}$$

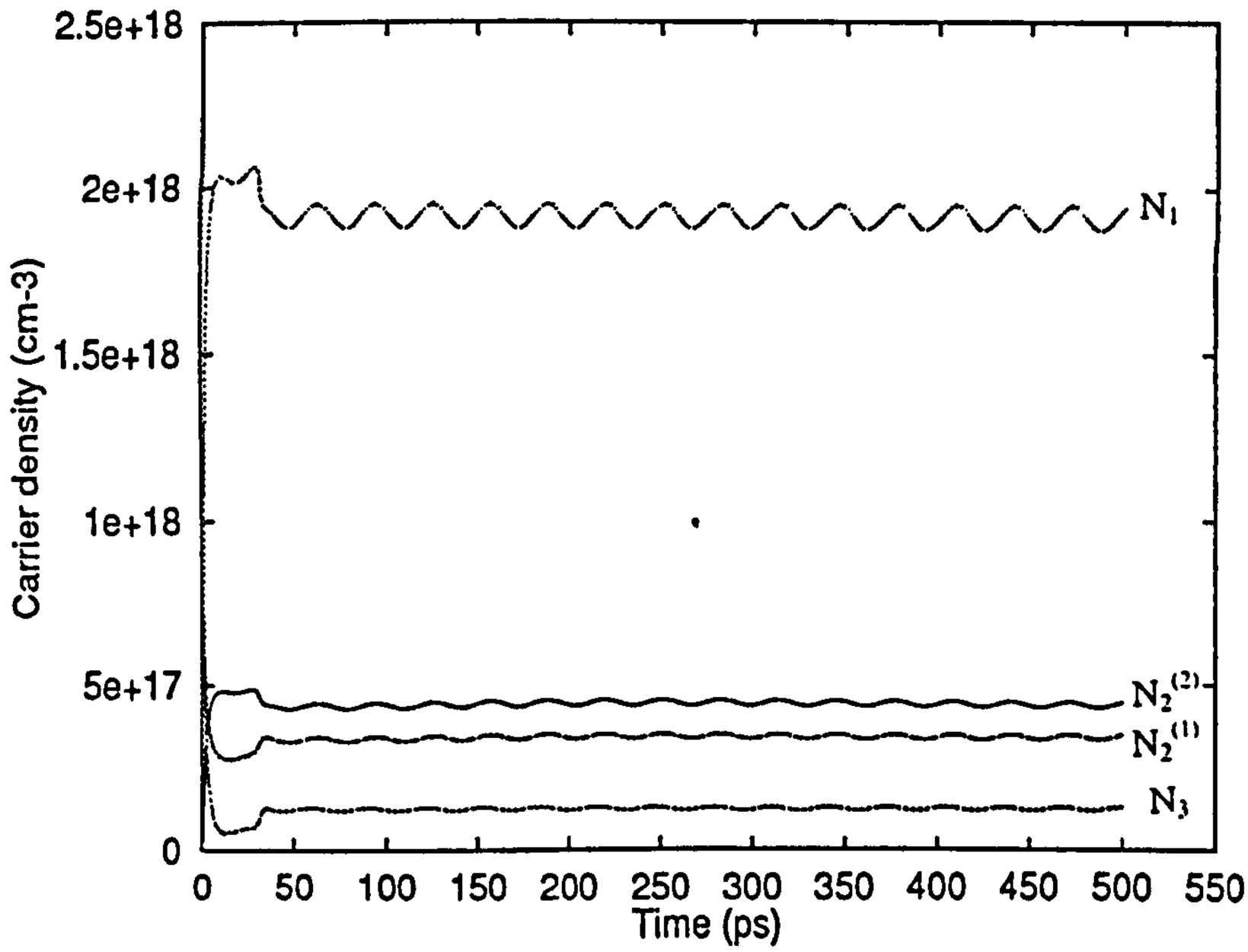

Figure B.1: Simulation results showing the variation of the carrier densities with time.

Substituting the above expression for n_s back into Equation (B.33), and neglecting the term $\frac{2L_3 n_3}{L_2 \tau_W}$ since, from Figure B.1, n_3 is much smaller than $n_1, n_2^{(2)}$ and $n_2^{(1)}$, the following expression is found:

$$\frac{\mathrm{d}n_d}{\mathrm{d}t} = \frac{J_m(t)\tau_T}{2eL_2\tau_W} - \frac{J_m(t)\tau_T}{2eL_2\tau_S} - n_d\Big(2a\bar{P} + \frac{1}{\tau_W} + \frac{1}{\tau_S}\Big) - \frac{2p}{\tau_P} \tag{B.36}$$

Differentiating Equation (B.36), and noting that $\mathrm{d}p/\mathrm{d}t = a\bar{P}n_d$, the familiar 2nd order carrier rate equation may be derived:

$$\begin{aligned} \frac{\mathrm{d}^2 n_d}{\mathrm{d}t^2} + \Big(2a\bar{P} + \frac{1}{\tau_W} + \frac{1}{\tau_S}\Big)\frac{\mathrm{d}n_d}{\mathrm{d}t} \quad + \quad & \frac{a\bar{P}}{\tau_P} n_d = \frac{\tau_T}{2eL_2}\Big(\frac{1}{\tau_W} - \frac{1}{\tau_S}\Big)\frac{\mathrm{d}J_m(t)}{\mathrm{d}t} \\ \frac{\mathrm{d}^2 n_d}{\mathrm{d}t^2} + \gamma\frac{\mathrm{d}n_d}{\mathrm{d}t} + \omega_0^2 n_d \quad = \quad & \frac{\tau_T}{2eL_2}\Big(\frac{1}{\tau_W} - \frac{1}{\tau_S}\Big)\frac{\mathrm{d}J_m(t)}{\mathrm{d}t} \end{aligned} \tag{B.37}$$

where

$$\gamma = 2a\bar{P} + \frac{1}{\tau_W} + \frac{1}{\tau_S} \qquad \text{and} \qquad \omega_0^2 = \frac{a\bar{P}}{\tau_P} \tag{B.38}$$

B.3.1 Second-order Photon Rate Equation

In order to find the equivalent 2nd order photon rate equation, consider Equation (4.33), where $\mathrm{d}p/\mathrm{d}t = a\bar{P}n_d$, so

$$n_d = \frac{1}{a\bar{P}}\frac{\mathrm{d}p}{\mathrm{d}t} \tag{B.39}$$

Differentiating Equation (4.33), and subsituting the above Equation (B.39) into the resulting expression gives

$$\begin{aligned} \frac{\mathrm{d}^2 p}{\mathrm{d}t^2} &= a\bar{P}\frac{\mathrm{d}n_d}{\mathrm{d}t} \\ &= a\bar{P}\Big(-\frac{2p}{\tau_P} - (2a\bar{P} + \frac{1}{\tau_W} + \frac{1}{\tau_S})n_d + \frac{J_m(t)\tau_T}{2eL_2}(\frac{1}{\tau_W} - \frac{1}{\tau_S})\Big) \\ &= -\frac{2a\bar{P}}{\tau_P}p - \Big(2a\bar{P} + \frac{1}{\tau_W} + \frac{1}{\tau_S}\Big)\frac{\mathrm{d}p}{\mathrm{d}t} + \frac{J_m(t)\tau_T a\bar{P}}{2eL_2}\Big(\frac{1}{\tau_W} - \frac{1}{\tau_S}\Big) \end{aligned} \tag{B.40}$$

And hence,

$$\frac{\mathrm{d}^2p}{\mathrm{d}t^2} + \gamma\frac{\mathrm{d}p}{\mathrm{d}t} + \omega_0^2 p = \frac{J_m(t)\tau_T a\bar{P}}{2eL_2}\left(\frac{1}{\tau_W} - \frac{1}{\tau_S}\right) \tag{B.41}$$

B.3.2 Modulation Response

Assuming that the modulation current is sinusoidal, with a frequency ω_m, so that $J_m(t) = J_m\cos(\omega_m t)$, and that due to that modulation, the photon response is also sinusoidal, then

$$p = \bar{p}e^{j\omega_m t} \tag{B.42}$$

So that,

$$\frac{\mathrm{d}^2p}{\mathrm{d}t^2} = -\omega_m^2 p \qquad \text{and} \qquad \frac{\mathrm{d}p}{\mathrm{d}t} = j\omega_m p \tag{B.43}$$

Substituting the above terms into Equation (B.40) gives

$$(\omega_0^2 - \omega_m^2)p + j\omega_m\gamma p = \frac{a\tau_T}{2eL_2}\left(\frac{1}{\tau_W} - \frac{1}{\tau_S}\right)J_m \tag{B.44}$$

And hence the modulation depth can be written as

$$\eta = \frac{p}{\bar{P}} = \frac{\frac{a\tau_T}{2eL_2}\left(\frac{1}{\tau_W} - \frac{1}{\tau_S}\right)J_m}{(\omega_0^2 - \omega_m^2) + j\omega_m} \tag{B.45}$$

Appendix C

Derivation and Proof of Equations

C.1 Derivation of the Schrödinger Equation of Equation (2.14)

Here, the time-independent conduction-band effective mass Schrödinger equation is derived. Using Equations (2.12) and (2.13) from Chapter 2 where

$$\frac{-\hbar^2}{2m^*(r)}\nabla^2\Psi(r,t) + V(r)\Psi(r,t) = E\Psi(r,t) \tag{C.1}$$

and $\Psi(r,t) = \psi(r)w(t)$, where the time-dependent part

$$w(t) = e^{-j(E/\hbar)t} \tag{C.2}$$

First, rearrange Equation (C.1) into the form

$$\begin{aligned} \frac{-\hbar^2}{2m^*(r)}\nabla^2\Psi(r,t) &= E\Psi(r,t) - V(r)\Psi(r,t) \\ &= [E - V(r)]\Psi(r,t) \end{aligned} \tag{C.3}$$

When Equation (C.2) is substituted into the above expression, the following expression is obtained

$$\frac{-\hbar^2}{2m^*(r)}\nabla^2\psi(r)e^{-j(E/\hbar)t} = [E - V(r)]\psi(r)e^{-j(E/\hbar)t} \tag{C.4}$$

which then reduces to Equation (2.14) where:

$$\frac{-\hbar^2}{2m^*(r)}\nabla^2\psi(r) + V(r)\psi(r) = E\psi(r) \tag{C.5}$$

C.2 Proof of Cauchy's Integral Formula

Let $f(z)$ be analytic within and on C, a simple closed contour described counter-clockwise (CCW). Then for any point z_0 within C,

$$f(z_0) = \frac{1}{j2\pi}\int_C \frac{f(z)}{(z - z_0)}dz \tag{C.6}$$

This is Cauchy's Integral Formula, and it says that if a function f is to be analytic within and on the simple contour C, then the values of f inside C are completely determined by the values of f on C. The proof of this theorem is as below:

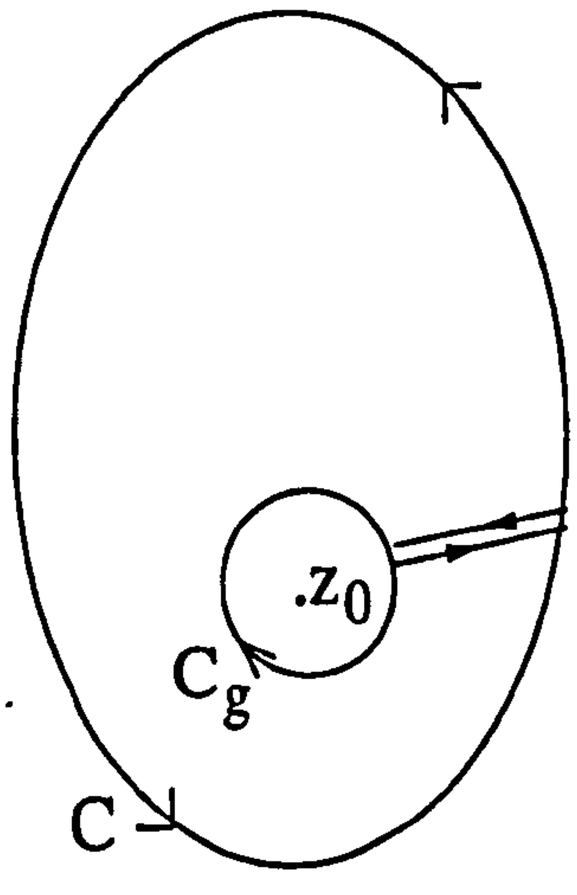

Choose a small circle C_s with centre z_0, radius δ, described clockwise (CW), and enclosed by C. Insert a cross-cut from C_g to C. Applying the Cauchy-Goursat Theorem to the simple closed curve, and noting that the two contributions of the cross-cut cancel, we obtain:

$$\int_C \frac{f(z)}{(z-z_0)}dz + \int_{C_g} \frac{f(z)}{(z-z_0)}dz = 0 \tag{C.7}$$

Therefore,

$$\int_C \frac{f(z)}{(z-z_0)}dz = -\int_{C_g} \frac{f(z)}{(z-z_0)}dz - \int_{C_g} \frac{f(z)-f(z_0)}{z-z_0}dz \tag{C.8}$$

Knowing that $\int_{C_g} \frac{dz}{z-z_0} = -j2\pi$, we can write:

$$\left| \int_C \frac{f(z)}{(z-z_0)}dz - j2\pi f(z_0) \right| = \left| \int_{C_g} \frac{f(z)-f(z_0)}{z-z_0}dz \right| \leq 2\pi\delta \frac{1}{\delta} \max_{C_g} |f(z)-f(z_0)| \tag{C.9}$$

This expression maybe made arbitrarily small, and hence its value must be zero. Equation (C.9) now reduces to

$$\int_C \frac{f(z)}{(z-z_0)}dz = f(z_0)j2\pi \tag{C.10}$$

and the theorem is proved.

C.3 Proof of the Cauchy Formula for Derivatives

This theorem says that if a function f is analytic at a point, then its derivatives of all orders are also analytic functions at that point. So, if C is a simple closed contour CCW, $f(z)$ is analytic within and on C, and z_0 is within C, then

$$f^{(n)}(z_0) = \frac{n!}{j2\pi} \int_C \frac{f(z)}{(z-z_0)^{n+1}}dz \tag{C.11}$$

Proof:

Start from Cauchy's Intergral Formula, and differentiate repeatedly with respect to z_0:

$$\begin{aligned}
\text{(i) } f(z_0) &= \frac{1}{j2\pi}\int_C \frac{f(z)}{z-z_0}dz \\
\text{(ii) } f'(z_0) &= \frac{1}{j2\pi}\int_C f(z)(-1)(z-z_0)^{-2}(-1)dz = \frac{1}{j2\pi}\int_C \frac{f(z)}{(z-z_0)^2}dz \\
\text{(iii) } f''(z_0) &= \frac{1}{j2\pi}\int_C f(z)(-2)(z-z_0)^{-3}(-1)dz = \frac{2}{j2\pi}\int_C \frac{f(z)}{(z-z_0)^3}dz
\end{aligned}$$

etc.

There is an observable pattern, and hence the theorem is proved.

C.4 Derivation of the Expression for the Subband Quasi-Fermi Levels

$$\begin{aligned}
N &= \int_0^\infty \rho_r(\epsilon) f_c(\epsilon) dE \qquad \text{(C.12)} \\
&= \int_0^\infty \frac{m}{\pi\hbar^2 L_z} \frac{1}{1+\ \exp(\frac{E-E_{fc}}{kT})} dE \\
&= \frac{m}{\pi\hbar^2 L_z} J
\end{aligned}$$

where

$$\begin{aligned}
J &= \int_0^\infty \frac{dE}{1+\ \exp(\frac{E-E_{fc}}{kT})} \qquad \text{(C.13)} \\
&= kT\int_{-\frac{E_{fc}}{kT}}^\infty \frac{dx}{1+e^x} \\
&= kT\ln[(1+\ \exp\Big(-\frac{E_{fc}}{kT}\Big) + \frac{E_{fc}}{kT}]
\end{aligned}$$

and $x = (E - E_{fc})/kT$ so that $dE = kTdx$ and $E = kTx + E_{fc}$.

Substituting Equation (C.13) back to the original equation, we have

$$\frac{N\pi\hbar^2 L_z}{kTm_c} = \ln[1 + \exp\Big(-\frac{E_{fc}}{kT}\Big)] + \frac{E_{fc}}{kT} \quad \text{(C.14)}$$

$$\exp\Big(\frac{N\pi\hbar^2 L_z}{kTm_c} - \frac{E_{fc}}{kT}\Big) = 1 + \exp\Big(-\frac{E_{fc}}{kT}\Big)$$

$$\exp\Big(\frac{N\pi\hbar^2 L_z}{kTm_c}\Big)/\exp\Big(\frac{E_{fc}}{kT}\Big) = 1 + \exp\Big(-\frac{E_{fc}}{kT}\Big)$$

$$\exp\Big(\frac{N\pi\hbar^2 L_z}{kTm_c}\Big) = \exp\Big(\frac{E_{fc}}{kT}\Big) + 1$$

$$E_{fc} = kT\ln[\exp\Big(\frac{N\pi\hbar^2 L_z}{kT}\Big) - 1]$$

C.5 Fermi's Golden Rule

Consider the Schrödinger equation below, which relates the system Hamiltonian H_0 of the crystal lattice to the energy E of the electron:

$$H_0 = \Big[\frac{\mathbf{p}^2}{2m_0} + V(\mathbf{r})\Big]\psi = E\psi \quad \text{(C.15)}$$

where $\mathbf{p}$ is the momentum operator, $\mathbf{r}$ is the position vector, m_0 is the free electron mass, ψ is the wavefunction of the electron, and $V(\mathbf{r})$ is the potential in the semiconductor.

In order to examine the electron-photon interaction which causes transitions in the semiconductor, the photon is represented classically by an electromagnetic wave. The wave's interaction with the electron enters into the Schrödinger's equation through the vector potential (see e.g. The Feynman Lectures on Physics (FLP), vol. II and III), which can be expressed as

$$\mathbf{A}(\mathbf{r}, t) = \hat{\mathbf{e}}\ \mathrm{Re}[A(\mathbf{r})e^{-i\omega t}] = \hat{\mathbf{e}}\frac{1}{2}[A(\mathbf{r})e^{-i\omega t} + A^*(\mathbf{r})e^{-i\omega t}] \quad \text{(C.16)}$$

where $\hat{\mathbf{e}}$ is the unit polarisation vector in the direction of $\mathbf{A}$, and ω ($\hbar\omega$) is the angular frequency (energy) of the photon. The Schrödinger equation in Equation (C.15) is now modified by the substitution [FLP]

$$\mathbf{p}^2 \rightarrow (\mathbf{p} + e\mathbf{A})^2 \approx \mathbf{p}^2 + 2e\mathbf{A} \cdot \mathbf{p} \tag{C.17}$$

where e is the magnitude of the electron charge. In expanding the square, the squared vector potential term can be neglected, since it does not affect the final results. Substituting Equation (C.17) into Equation (C.15), the new Hamiltonian is then

$$H = H_0 + [H'(\mathbf{r}e^{-i\omega t} + \text{h.c.}], \qquad H'(\mathbf{r}) \equiv \frac{e}{2m_0} A(\mathbf{r})\hat{\mathbf{e}} \cdot \mathbf{p} \tag{C.18}$$

the h.c. stands for Hermitian conjugate, and it simply means that the complex conjugate of all the terms is taken, except the Hermitian operator $\mathbf{p}$. The term in brackets can be viewed as a time-dependent perturbation to the original Hamiltonian. The effect of this perturbation is to induce electronic transitions between the initial and final states.

By studying the time evolution of some electron wavefunction in an initial state as it makes a transition (whether upward or downward) to the final state in the presence of the time-harmonic perturbation, it is possible to determine the rate at which such transitions occur (see e.g. Appendix 9, Coldren and Corzine). The resulting transition rate per unit volume of active material is given (in units of $\text{s}^{-1}\text{cm}^{-3}$) by

$$R_r = \frac{2\pi}{\hbar} |H'_{21}|^2 \rho_f(E_{21})|_{E_{21}=\hbar\omega} \tag{C.19}$$

$$H'_{21} \equiv \langle \psi_2 | H'(\mathbf{r}) | \psi_1 \rangle = \int_V \psi_2^* H'(\mathbf{r}) \psi_1 d^3\mathbf{r} \tag{C.20}$$

Equation (C.19) is known as Fermi's Golden Rule. Using it, the task of determing the transition rate, R_r, is reduced to providing explicit relations for both the density of final states and the overlap integral (or matrix element).

Appendix D

List of Publications and Manuscripts

D.1 Journal Papers

1. P. S. Spencer, C. Y. L. Cheung and K. A. Shore, "Sensitivity analysis of the optical-waveguide properties of quantum cascade lasers," *IEE Proc.-Optoelectron.* **144**, pp. 323-326, 1997.

2. C. Y. L. Cheung, P. S. Spencer and K. A. Shore, "Modulation bandwidth optimisation for unipolar intersubband semiconductor lasers," *IEE Proc. Optoelectron.* **144**, pp. 44-47, 1997.

3. C. Y. L. Cheung and K. A. Shore, "Self-consistent analysis of the dc modulation response of unipolar semiconductor lasers ," *J. Mod. Optics* **45**, pp. 1219-1229, 1998.

4. C. Y. L. Cheung and K. A. Shore, "Anti-crossing and coupling effects in

the design of intersubband semiconductor lasers," submitted for publication.

5. C. Y. L. Cheung, P. Rees and K. A. Shore, "Gain calculations for unipolar semiconductor lasers," submitted for publication.

6. C. Y. L. Cheung, P. Rees and K. A. Shore, "*Self-consistent* optical gain and threshold current calculations for 1.55μm intersubband semiconductor lasers," submitted for publication.

7. C. Y. L. Cheung, K. A. Shore and P. Rees, "Quantum well structures for THG and FWM by application of electric field," Manuscript in preparation.

8. N. Cinosi, C. Y. L. Cheung and K. A. Shore, "Mode transformations in planar self-similar Cantor waveguide structures," Manuscript in preparation.

D.2 Conference Publications

1. K. A. Shore, P. S. Spencer and C. Y. L. Cheung, "Threshold conditions and modulation properties of intersubband lasers," *Quantum Electronics Symposium IOP CMMP'95*, Liverpool, December 1995.

2. C. Y. L. Cheung, P. S. Spencer and K. A. Shore, "Modulation bandwidth predictions for unipolar intersubband semiconductor lasers," 10th Conference on Semiconductor and Integrated Optoelectronics (SIOE'96), Cardiff, April 1996.

3. C. Y. L. Cheung, P. S. Spencer and K. A. Shore, "Modulation bandwidth predictions for intersubband quantum well semiconductor lasers," Optical Society of America, Integrated Photonics Research Conference, Boston, Mass. USA, post-deadline paper PD-1, April 1996.

4. C. Y. L. Cheung, P. S. Spencer and K. A. Shore, "Optimisation of maximum modulation bandwidth of intersubband semiconductor lasers," Mid-Infrared Optoelectronics: Materials and Devices," Lancaster University, September 1996.

5. C. Y. L. Cheung and K. A. Shore, "Electron Lifetime Calculations and Lasing Properties of intersubband semiconductor lasers," 11th Conference on Semiconductor and Integrated Optoelectronics (SIOE'97), Cardiff, March 1997.

6. C. Y. L. Cheung, P. S. Spencer and K. A. Shore, "Analysis of the dynamical properties and modulation response of unipolar intersubband semiconductor lasers," Optical Society of America, CLEO/QELS '97, Baltimore, Maryland, USA, paper CThS2, May 1997.

7. C. Y. L. Cheung and K. A. Shore, "Self-consistent analysis of the dc modulation response of unipolar semiconductor lasers ," 13th Quantum Electronics Conference (QE-13), September 1997.

8. C. Y. L. Cheung and K. A. Shore, "Carrier lifetime calculations and modulation response of intersubband lasers," SPIE Photonics West '98, Conference Physics and Simulation of Optoelectronic Devices, San Jose, CA USA, paper 3283/48, January 1998.

9. C. Y. L. Cheung, P. Ress and K. A. Shore, "Gain calculations for unipolar semiconductor lasers," 12th Conference on Semiconductor and Integrated Optoelectronics (SIOE'98), Cardiff, April 1998.

10. N. Cinosi, C. Y. L. Cheung and K. A. Shore, "Mode transformations in planar self-similiar Cantor waveguide structures," 12th Conference on Semiconductor and Integrated Optoelectronics (SIOE'98), Cardiff, April 1998.

11. C. Y. L. Cheung, P. Rees and K. A. Shore, "Estimation of threshold current for unipolar intersubband semiconductor lasers," Semiconductor Quantum Wires and Dots, DERA, Malvern, June 1998.

12. C. Y. L. Cheung, P. Rees and K. A: Shore, "Quantum well structures for THz bandwidth NIR unipolar semiconductor lasers," 6th IEEE International Conference on Terahertz Electronics (THz98), September 1998.

13. C. Y. L. Cheung, P. Rees and K. A. Shore, "Optical gain calculations for NIR intersubband semiconductor lasers," CLEO (Europe) Glasgow, September 1998.

14. C. Y. L. Cheung, P. Rees and K. A. Shore, "Modulation bandwidth and gain calculations for near-infra red intersubband semiconductor lasers," IOP Meeting on Vertical Transport and Intersubband Processes in Low-Dimensional Structures, Sheffield, October 1998.